

Master thesis  
Studies of Solar Magnetic Cycle  
and Differential Rotation  
Based on Mean Field Model

Hideyuki Hotta  
(堀田英之)

Department of Earth and Planetary Science  
Graduate School of Science, The University of Tokyo

2011

# Contents

<b>I</b>	<b>General Introduction</b>	<b>11</b>
<b>1</b>	<b>Cyclic Variation of Solar Activity</b>	<b>11</b>
1.1	Observational History and Result . . . . .	11
<b>2</b>	<b>Dynamo Models</b>	<b>15</b>
2.1	Kinematic Dynamo and MHD dynamo . . . . .	16
2.2	Mean Field Model . . . . .	18
2.3	Axisymmetric Equation . . . . .	20
2.4	$\Omega$ -effect (Poloidal to Toroidal) . . . . .	22
2.5	$\alpha$ -effect (Toroidal to Poloidal) . . . . .	23
2.6	Dynamo Wave . . . . .	24
<b>3</b>	<b>Solar Large Scale Flow</b>	<b>29</b>
3.1	Differential Rotation . . . . .	29
3.2	Meridional Flow . . . . .	30
<b>4</b>	<b>Flux-Transport Dynamo</b>	<b>30</b>
4.1	Babcock-Leighton $\alpha$ -effect and Flux Emergence . . . . .	30
4.2	General Property of Flux-Transport Dynamo . . . . .	34
<b>5</b>	<b>Overview of this Thesis</b>	<b>36</b>

## II Turbulent Diffusion and Prediction of Next Maximum

<b>III</b>	<b>Importance of Surface Turbulent Diffusivity</b>	<b>43</b>
<b>6</b>	<b>Introduction</b>	<b>43</b>
<b>7</b>	<b>Model</b>	<b>45</b>
7.1	Basic Equations . . . . .	45
7.2	Differential Rotation . . . . .	46
7.3	Meridional Flow . . . . .	46
7.4	Diffusivity . . . . .	50
7.5	Poloidal Source Term . . . . .	50
7.6	Numerical Domain and Boundary Conditions . . . . .	53
<b>8</b>	<b>Reference Solution</b>	<b>54</b>
<b>9</b>	<b>Parameter Dependence</b>	<b>55</b>
9.1	Dependence of the Magnetic Field . . . . .	55
9.2	Dependence of cycle period . . . . .	64
<b>10</b>	<b>Cases with Shallow Meridional Flow</b>	<b>64</b>
<b>11</b>	<b>Distribution of <math>\alpha</math> effect</b>	<b>67</b>
<b>12</b>	<b>Discussion and Conclusion</b>	<b>71</b>
<b>IV</b>	<b>Parity of Solar Global Magnetic Field</b>	<b>75</b>

<b>13 Introduction</b>	<b>75</b>
<b>14 Model</b>	<b>77</b>
<b>15 Results</b>	<b>78</b>
<b>16 Discussion and Conclusion</b>	<b>82</b>
<b>V Differential Rotation in Rapidly Rotating Stars</b>	<b>86</b>
<b>17 Introduction</b>	<b>86</b>
<b>18 Model</b>	<b>88</b>
18.1 Equations . . . . .	88
18.2 Background Stratification . . . . .	91
18.3 Diffusivity Profile . . . . .	92
18.4 The $\Lambda$ effect . . . . .	94
18.5 Numerical Settings . . . . .	97
<b>19 Stellar Differential Rotation and the Taylor-Proudman Theorem</b>	<b>99</b>
<b>20 Results and discussion</b>	<b>100</b>
20.1 Stellar Differential Rotation . . . . .	100
20.2 Angular Velocity Difference on the Surface . . . . .	104
<b>21 Summary</b>	<b>109</b>
<b>VI Future perspective</b>	<b>114</b>

<b>A</b>	<b>List of Symbols</b>	<b>125</b>
<b>B</b>	<b>Vector Formula</b>	<b>125</b>
	B.1 General Formula . . . . .	125
	B.2 Formular in Spherical Polar Coordinate . . . . .	125
<b>C</b>	<b>Derivation for Axisymmetric Induction Equation</b>	<b>127</b>
<b>D</b>	<b>Derivation for Turbulent <math>\alpha</math> effect and Diffusivity</b>	<b>128</b>
<b>E</b>	<b>Non-dimensional Number in Solar Convection Zone</b>	<b>132</b>
<b>F</b>	<b>Physical Meaning of <math>\Lambda</math> effect</b>	<b>133</b>
<b>G</b>	<b>Numerical Method</b>	<b>135</b>
	G.1 modified Lax-Wendroff scheme . . . . .	135
	G.2 artificial viscosity which satisfied TVD criterion . . . . .	137

# Abstract

The number of the sunspots has an eleven-year cycle. This cycle is thought to be sustained by the dynamo action by the solar internal plasma. The dynamo is a transformation from kinetic energy to magnetic energy. The flux-transport dynamo model succeeds to reproduce some features of the solar cycle, e.g. the poleward migration of the general field and the equatorward migration of the latitude where the sunspots appear. The flux-transport dynamo model, however, significantly depends on the free parameters, because all flux-transport dynamo models adopt the mean field assumption in which the turbulent is took as a parameter and most of flux-transport dynamo models is solved with the kinematic assumption in which the fluid velocity is given and only the magnetic induction equation is solved. The magnetic turbulent diffusivity is one of the most important parameters for the solar dynamo. Turbulent diffusivity is caused by the solar internal turbulence on the magnetic field. It is difficult to evaluate the amplitude of the turbulent diffusivity by the observation. We show two studies to make some constraints on the distribution of the turbulent diffusivity.

The first study is published as Hotta & Yokoyama (2010a). It has been known that previous flux-transport dynamo models failed to avoid the strong polar surface field and the strong toroidal field at the base in the high latitude, both of which are not consistent with observations. We propose a new regime of the flux-transport dynamo model by assuming an additional intense diffusivity profile near the surface. The surface poloidal field generated by the  $\alpha$  effect is transported down to the base of the convection zone not by the meridional flow but by the surface diffusion mainly

in the mid-latitude. With a moderate  $\alpha$ -quenching, this prevents the concentration of the polar surface field and the amplification of the toroidal field at the high latitude. The condition to obtain the proper magnetic field strength near the pole is  $\eta_{\text{surf}}/v_0 > 2 \times 10^9$  cm, where  $\eta_{\text{surf}}$  and  $v_0$  are the surface diffusivity and the meridional flow speed, respectively. We also do some parameter studies to ensure the importance of the surface strong diffusivity. In addition, the dependence of the cycle period on free parameters, the speed of meridional flow and the surface diffusivity, is investigated.

Next study is published as Hotta & Yokoyama (2010b). We investigated the dependence of the solar magnetic parity between the hemispheres on two important parameters, the turbulent diffusivity and the meridional flow, by means of axisymmetric kinematic dynamo simulations based on the flux-transport dynamo model. It is known that the coupling of the magnetic field between hemispheres due to turbulent diffusivity is an important factor for the solar parity issue, but the detailed criterion for the generation of the dipole field has not been investigated. Our conclusions for this study are as follows. (1) The stronger diffusivity near the surface is more likely to cause the magnetic field to be a dipole. (2) The thinner layer of the strong diffusivity near the surface is also more apt to generate a dipolar magnetic field. (3) The faster meridional flow is more prone to cause the magnetic field to be a quadrupole, i.e., symmetric about the equator. These results show that turbulent diffusivity and meridional flow are crucial for the configuration of the solar global magnetic field.

We conduct a further investigation for the stellar activity. The flux-transport dynamo is thought to be adopted to study the stellar activity and there are some

studies for the stellar kinematic dynamo. It is, however, difficult in the kinematic dynamo model to evaluate the dynamo-generated magnetic field. Thus as a first step, we investigate differential rotation in rapidly rotating solar-type stars by means of an axisymmetric mean field model that was previously applied to the sun. This allows us to calculate the latitudinal entropy gradient with a reasonable physical basis. Our conclusions are as follows: (1) Differential rotation approaches the Taylor-Proudman state when stellar rotation is faster than solar rotation. (2) Meridional flow is insensitive to stellar angular velocity. (3) Turbulent viscosity and turbulent angular momentum transport determine the spatial difference of angular velocity  $\Delta\Omega$ . (4) The results of our mean field model can explain observations of stellar differential rotation.

## 要旨

太陽の黒点数は 11 年の周期をもって、増減していることが知られているが、これは太陽内部のダイナモという運動エネルギーから磁場のエネルギーへの変換機構によって維持されていると考えられている。中でも磁束輸送ダイナモというモデルは、一般磁場の極への移動、黒点出現緯度の赤道への移動などの観測事実を良く説明できるモデルとして受け入れられている。しかし、太陽内部で大きな役割を果たしていると考えられている対流をあらわに解かない平均場モデルを採用している上に、ほとんどのモデルで速度場は観測から与え、磁場の誘導方程式のみを解く、運動学的ダイナモで議論されているために、結果がパラメーターに依存することが知られている。中でも、太陽内部の乱流が磁場に作用し、実効的に拡散的に作用する効果である乱流磁気拡散は観測的に推定することが困難であるのに、計算結果を大きく変える重要なパラメータとして知られている。そこで、この乱流磁気拡散の太陽内部の分布に制限を与えるために、我々は二つの研究を行った。

一つ目は Hotta & Yokoyama (2010a) として論文にされた研究である。磁束輸送ダイナモモデルは、多くの太陽活動周期の特徴を再現できたモデルであるが、表面の極と、対流層の底の高緯度に観測と合わない強磁場を避けることができないことが知られている。我々はこの状況に対して、表面近くに強い乱流磁場拡散があるというモデルを提案した。表面で  $\alpha$  効果によって生成されたポロイダル磁場は子午面環流ではなく、中緯度付近で乱流拡散によって運ばれるとしたのである。このモデルによって、子午面環流による磁場の極への集中が抑えられた上に、ポロイダル磁場が極付近に運ばれないことから強いトロイダル磁場が対流層の底で生成されるのも抑えることができた。極付近の強い強磁場を避けるために我々は  $\eta_{\text{surf}}/v_0 > 2 \times 10^9 \text{ cm}$  という条件を得た、ここで  $\eta_{\text{surf}}$ 、 $v_0$  はそれぞれ表面付近の乱流磁気拡散、子午面環流

の速さである。また、周期の長さの子午面環流、表面乱流拡散への依存性も調べた。

次の研究は Hotta & Yokoyama (2010b) として論文にした。この研究では、太陽の大局的磁場の赤道に対する対称性の乱流拡散と子午面環流の速度という二つの重要なパラメータに対する依存性について磁束輸送ダイナモに基づいて調べた。乱流拡散による半球間での磁場の相互作用が太陽の対称性には重要であることが知られているが、双極子磁場を作るための詳細な条件はこれまでに知られていない。この研究の我々の結論は以下である。(1) 表面付近の乱流拡散が強いほど、磁場は双極子になりやすくなる。(2) 表面付近の強い乱流拡散の領域が狭いほど、磁場は双極子になりやすくなる。(3) 子午面環流が速いほど、磁場は四重極子磁場になりやすくなる。これらの結果から、乱流拡散や子午面環流の速さは磁場の対称性において重要なパラメータであることがわかる。

さらに続く研究として、我々は太陽以外の恒星の研究をおこなった。磁束輸送ダイナモは、恒星ダイナモにも適用できると考えられているために多くの運動学的ダイナモによる研究がなされている。しかし、運動学的ダイナモでは恒星で作られる磁場の強さを見積もることができない。ここで、磁気流体ダイナモが必要となるのであるが、我々はその足掛かりとして軸対称平均場流体モデルで自転角速度の大きい恒星の内部角速度分布を調べた。角速度の勾配が磁場をねじり、運動エネルギーから磁場のエネルギーへの変換をおこなうので、内部角速度分布はダイナモ研究にとって重要である。我々は太陽内部角速度分布の再現に成功したモデルに基づいた研究をおこなった。このモデルでは、対流層の底で太陽内部の角速度分布を再現することのできるエントロピーの勾配を作ることができ、恒星に適用する上でも利点となる。この研究の我々の結論は以下である。(1) 恒星内部の差動回転は自転角速度が大きくなると、テイラー・プラウドマン状態になりやすくなる。(2) 子午面環流の速度の自転角速度への依存性は弱い。(3) 乱流粘性と乱流角運動量輸送によって、

表面の角速度の差  $\Delta\Omega$  は決まる。

## Part I

# General Introduction

## 1 Cyclic Variation of Solar Activity

### 1.1 Observational History and Result

The sunspot is a black spot observed on the solar surface. The human being discovered the sunspot long years ago. A Chinese document in 165 BC has some information on the sunspots (Wittmann & Xu, 1987; Hathaway, 2010). The observation for the sunspots has one of the longest history in the astronomy. Galileo began the scientific observation in the Seventeenth century. We can say that the solar physics began with this sunspots observation.

Some further investigations suggest that the number of sunspots has a cyclic behavior. The first mention of possible periodic behavior in sunspots came from Christian Horrebow who wrote in his 1776 diary (Wolf, 1877; Hathaway, 2010). Then Schwabe (1843) truly discovered the ten-years cyclic behavior of the number of the sunspot. Wolf (1861) defined his relative sunspot number to evaluate the observation of the sunspot as,

$$R_{\text{wolf}} = k_{\text{wolf}}(10g_{\text{wolf}} + f_{\text{wolf}}), \quad (1.1.1)$$

where  $f_{\text{wolf}}$  is the number of individual sunspots.  $g_{\text{wolf}}$  is the number of identified sunspot groups.  $k_{\text{wolf}}$  is a correction factor for the observer, the instrument and the location. Wolf confirmed the result of Schwabe (1843) with his definition of the relative sunspot number and argued that the number of sunspot has a eleven-year cyclic behavior (Wolf, 1861; Hoyt & Schatten, 1997). This definition of the relative

sunspots number is used until now.

The variation of the sunspot area is shown in the bottom panel of Fig. 1. There are some interesting laws about the appearance latitude of the sunspots. The sunspots appear in the middle latitude (about  $30^\circ$ ) in the beginning of the cycle. The appearance latitude migrates equatorward as the cycle progresses. This law is called Carrington-Spörer's law (Carrington, 1858). As a result, we can find some forms like butterflies in time-latitude plot of the sunspot area (The upper panel of Fig. 1.) which is called the butterfly diagram.

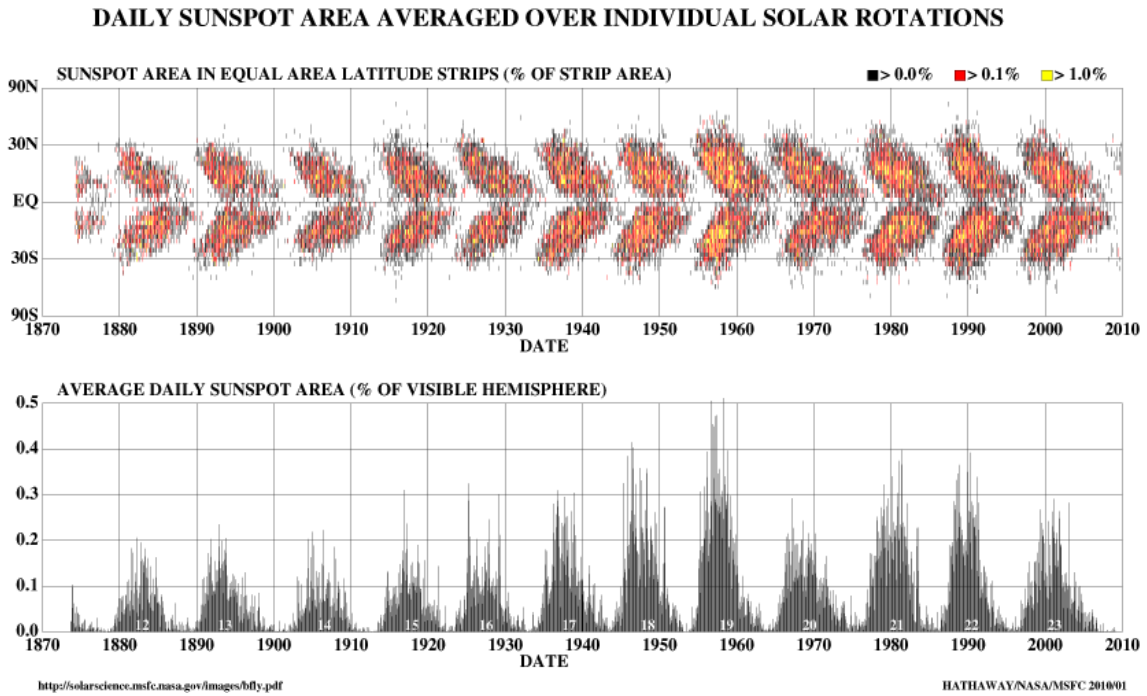


Figure 1: (top) The relative area in equal area latitude strips is illustrated with a color code. (bottom) Sunspot area as a function of latitude and time. The average daily sunspot area for each solar rotation since May 1874 is plotted as a function of time. (Hathaway, 2010)

Meanwhile Hale (1908) found that the sunspots have magnetic field. He discov-

ered that the absorbed line which is one line without the sunspot splits to two lines in the sunspot region. This behavior is caused by the Zeeman effect. This is the first discovery of the magnetic field in the space. In addition Hale suggested some laws about the sunspots. The sunspots almost always appear as a pair. These two sunspots have the opposite polarity and the line between them is almost parallel to east and west direction<sup>1</sup>. The west (east) side sunspot is called the preceding (following) spot. Hale et al. (1919) found that the preceding spot is closer to the equator than the following spot. This means that the line between the preceding and following spot has a tilt against iso-latitude lines. A. H. Joy suggested it earlier than Hale et al. (1919), so it is called Joy's law. Hale & Nicholson (1925) reported a law about the polarity of the sunspot pair. This law is called Hale-Nicholson's law. During one cycle, the preceding spot always has one polarity (N or S)<sup>2</sup>. When the polarity of the preceding spot is N in northern hemisphere, the polarity of the preceding spot in southern hemisphere has S polarity. In addition these polarities change in the next cycle. This law is explained in Fig. 2.

Then the accuracy of the observation was improved, so it was found that the magnetic field distributed in all of the surface of the sun. Babcock & Babcock (1955) called these "General field " to discriminate these and the active region. Babcock (1959) also found that the polarity of the polar magnetic field changes every eleven-year cycle. Fig. 3 shows the butterfly diagram of the magnetic field. It can be easily figured out that the general field migrates poleward and the polarity of the polar

---

<sup>1</sup>Solar north, south, east and west correspond to those of the earth. The right (left) direction from the observer in the earth is west (east) direction. The upward (downward) is north (south) direction. Fig. 2 shows its explanation.

<sup>2</sup>the N or positive (S or negative) polarity denotes the polarity of the magnetic field which comes to (goes away from) observer.

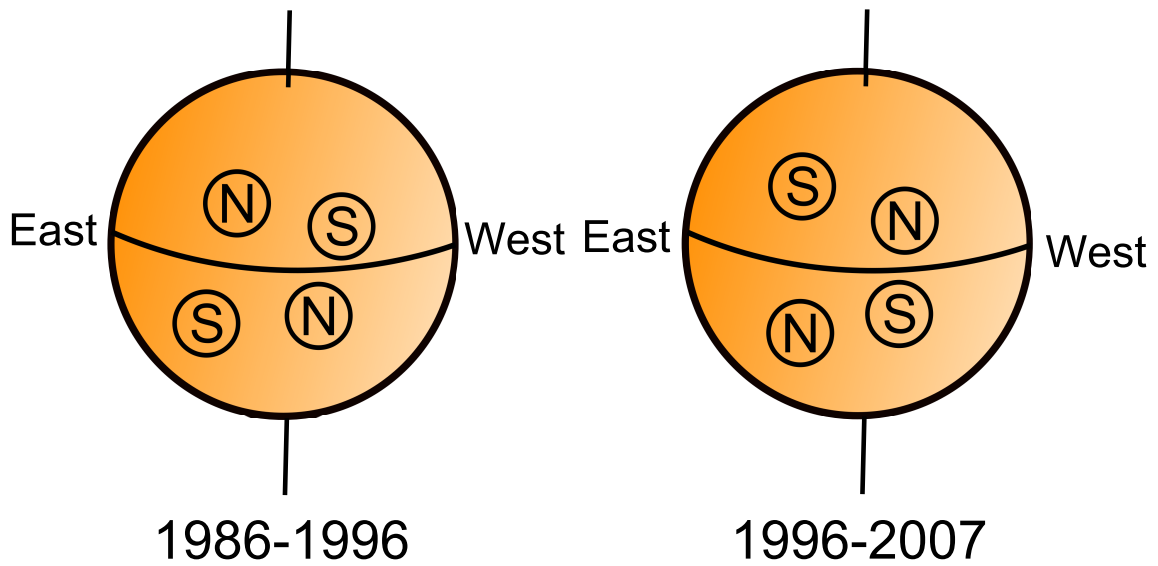


Figure 2: The schematic picture of Hale-Nicholson's law. N and S show the polarity of the sunspot in each cycle.

field is reversed.

The observational results are summarized as follows,

1. The number of sunspot has a eleven-year cyclic behavior (Schwabe's law).
2. The latitude where sunspot appears migrates from the mid-latitude to the low latitude during one cycle (Carrington-Spörer's law).
3. The line between the preceding and following spot has a tilt to the equator (Joy's law).
4. The polarity of the sunspot magnetic field has a pair structure between the hemispheres. This structure is kept during one cycle and reverses every eleven-year cycle (Hale-Nicholson's law).

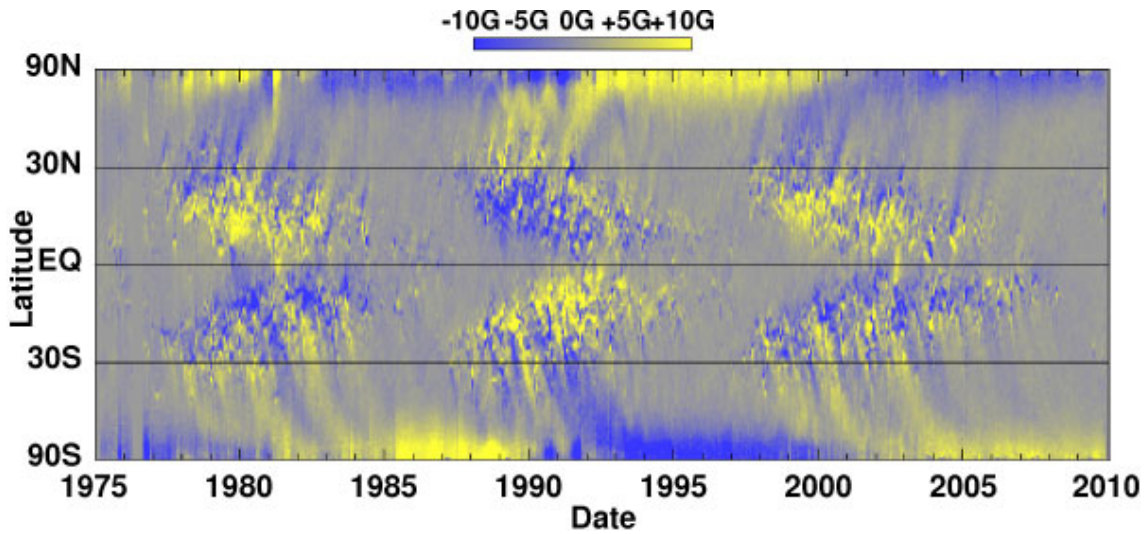


Figure 3: A Magnetic Butterfly Diagram constructed from the longitudinally averaged radial magnetic field obtained from instruments on Kitt Peak and SOHO. This illustrates Hale-Nicholson’s laws, Joy’s law, polar field reversals, and the transport of higher latitude magnetic field elements toward the poles Hathaway (2010).

5. The general magnetic field migrates from mid-latitude to the high latitude and the polarity of the polar magnetic field reverses every cycle.

We must explain these observational results by a model.

## 2 Dynamo Models

When the sun is born, the interstellar magnetic field is collected and the sun had magnetic field from the beginning of its life. These magnetic field must disappear in the long solar life by the turbulent diffusion. Therefore the current solar magnetic field indicates some maintenance mechanism. The solar dynamo is thought to be this maintenance mechanism. The dynamo means the transformation from the kinetic energy to the magnetic energy. The ionized plasma in the sun stretches the magnetic

field. The observational results explained in §1 is also thought to be achieved by this solar dynamo. In this section, we explain how the solar dynamo maintain the magnetic field and what the physical process of the observational results of the solar cycle is.

## 2.1 Kinematic Dynamo and MHD dynamo

In the interiors of the Sun, the collisional mean-free path of microscopic constituents is much shorter than competing plasma length scales. In this situation, the evolution of magnetic field is described by the combination of Ohm's and Ampere's laws, i.e. by the equation (Priest, 1987),

$$\frac{\partial \mathbf{B}}{\partial t} = \nabla \times (\mathbf{v} \times \mathbf{B} - \eta \nabla \times \mathbf{B}). \quad (1.2.1)$$

When we can solve eq. (1.2.1), the time-development of the magnetic field with given velocity  $\mathbf{v}$  is understood. The time-development of the velocity can be described by the Navier-Stokes equations in rotational system as,

$$\rho \frac{\partial \mathbf{v}}{\partial t} + \rho(\mathbf{v} \cdot \nabla)\mathbf{v} + 2\rho(\tilde{\boldsymbol{\Omega}} \times \mathbf{v}) = -\nabla p + \rho \mathbf{g} + \frac{1}{4\pi}(\nabla \times \mathbf{B}) \times \mathbf{B} + \nabla \cdot \boldsymbol{\Pi}. \quad (1.2.2)$$

We can understand consistently the interaction between the plasma and the magnetic field in the interior of the sun, i.e. the solar dynamo, by solving these two equations with the equation of continuity, the equation of energy and the equation of state. Concerning the transformation from the kinetic energy to the magnetic energy, we can understand more from eq. (1.2.1). Eq. (1.2.1) is modified as,

$$\begin{aligned} \frac{\partial \mathbf{B}}{\partial t} &= \nabla \times (\mathbf{v} \times \mathbf{B} - \eta \nabla \times \mathbf{B}) \\ &= (\mathbf{B} \cdot \nabla)\mathbf{v} - (\mathbf{v} \cdot \nabla)\mathbf{B} + \mathbf{B}(\nabla \cdot \mathbf{v}) + \eta \Delta \mathbf{B}, \end{aligned} \quad (1.2.3)$$

where the uniform magnetic diffusivity  $\eta$  is assumed. The first term of the right-side denotes that the magnetic field is stretched by the shear flow, i.e. the dynamo term. The magnetic field obtains the energy from the kinetic energy. The second term denotes the advection by means of the fluid velocity. The third term denotes that the magnetic field compresses (expands) with the convergence (divergence) flow. The fourth term denotes the magnetic diffusion. In this diffusion process, the magnetic field loses its energy. Whether the magnetic field keeps its energy or disappears is determined by the two opposing effects (the first and fourth terms). We must understand the physical mechanism of the solar dynamo i.e. the first term to maintain the solar magnetic activity. It is, however, very difficult to solve these equations simultaneously, because these equations are nonlinear and we know poorly about the physical process to maintain the solar large scale flow. Therefore we often adopt a simplified model i.e. the kinematic model. In the kinematic model, the fluid velocity is given from observation and other theory, so we solve only the magnetic induction equation (1.2.1). This simplification is justified because the amplitude of the variation of flow is relatively small (Vorontsov et al., 2002; Howe et al., 2009). In the kinematic model we assume that the energy of magnetic field is smaller than the kinetic energy. As we discuss in §3.1, the helioseismology reveals the internal structure of the global velocity. With this result, the magnetic induction equation becomes a linear equation which can be easily solved. Hereafter in this section we explain the development of the kinematic solar dynamo theory.

## 2.2 Mean Field Model

In most of solar kinematic model, the mean-field is assumed. The system is turbulent by the thermal convection in the solar internal convection zone. For simplicity, the magnetic and velocity field is decomposed to the mean field and perturbed field. Then only the equation for the mean field is solved. We must take some models for the influence from the perturbed field to the mean field. Krause & Rädler (1980) derived a formulation for the mean field model as follows. At first the magnetic and the velocity field is decomposed as,

$$\mathbf{B} = \overline{\mathbf{B}} + \mathbf{B}', \quad (1.2.4)$$

$$\mathbf{v} = \overline{\mathbf{v}} + \mathbf{v}', \quad (1.2.5)$$

where overline denotes the ensemble average. We take the ensemble average of the magnetic induction equation (1.2.1) as,

$$\frac{\partial \overline{\mathbf{B}}}{\partial t} = \nabla \times (\overline{\mathbf{v}} \times \overline{\mathbf{B}}) + \nabla \times (\overline{\mathbf{v}' \times \mathbf{B}'} - \eta \nabla \times \overline{\mathbf{B}}). \quad (1.2.6)$$

We can derive the formulation of  $\overline{\mathbf{v}' \times \mathbf{B}'}$  in an isotropic turbulence as,

$$\overline{\mathbf{v}' \times \mathbf{B}'} = \alpha \overline{\mathbf{B}} - \eta_t \nabla \times \overline{\mathbf{B}} \quad (1.2.7)$$

$$\alpha = -\frac{\tau}{3} \overline{\mathbf{v}' \cdot \nabla \times \mathbf{v}'}. \quad (1.2.8)$$

$$\eta_t = \frac{\tau}{3} \overline{\mathbf{v}'^2}. \quad (1.2.9)$$

The detailed derivation is given in Appendix D.  $\alpha$ ,  $\eta_t$  and  $\tau$  in eqs. (1.2.7)-(1.2.9) are the amplitude of the  $\alpha$ -effect by the turbulence, the turbulent diffusivity and the life time of turbulence respectively. It means that the amplitude of the turbulent  $\alpha$ -effect is determined by the kinetic helicity. For example, in Fig. 5, there is a positive

flow (upflow) with a negative vorticity, so  $\overline{\mathbf{v}' \cdot \nabla \times \mathbf{v}'} < 0$  and  $\alpha > 0$ . The sign of the turbulent  $\alpha$  is calculated numerically, and is positive (negative) in upper region of the northern (southern) hemisphere and negative (positive) in lower region, southern hemisphere (Gilman & Miller, 1981). Eq. (1.2.7) is substituted for eq. (1.2.6) and we can obtain the mean field dynamo equation as,

$$\frac{\partial \overline{\mathbf{B}}}{\partial t} = \nabla \times (\overline{\mathbf{v}} \times \overline{\mathbf{B}} + \alpha \overline{\mathbf{B}}) + (\eta_t + \eta) \Delta \overline{\mathbf{B}}, \quad (1.2.10)$$

where molecular and turbulent diffusivity ( $\eta$  and  $\eta_t$ ) are assumed uniform. Then we explain that the turbulent diffusivity is stronger effect than the molecular one as follows. At the base of convection zone, the amplitude of the molecular diffusivity is about  $4 \text{ cm}^2 \text{ s}^{-1}$  (see Appendix E). On the other hand, the amplitude of the turbulent diffusivity  $\eta_t$  can be evaluated with the characteristic velocity and the characteristic length scale ( $U$  and  $L$ , respectively) as  $\eta_t \sim UL$ . At the base of the convection zone the characteristic velocity is evaluated as  $U \sim 10^3 \text{ cm s}^{-1}$  by the mixing length theory (Stix, 2004). The length scale can be the same as the scale height, so we can evaluate it as  $L \sim 10^9 \text{ cm}$  as the base of convection zone. Therefore the turbulent diffusivity can have a value of  $\eta_t \sim 10^{13}$ . The turbulent diffusivity should be calculated with the first principle, but this calculation has not been achieved yet. It is clear that the turbulent diffusivity is much stronger than the molecular one, so the equation often adopted in mean field model is expressed as,

$$\frac{\partial \overline{\mathbf{B}}}{\partial t} = \nabla \times (\overline{\mathbf{v}} \times \overline{\mathbf{B}} + \alpha \overline{\mathbf{B}}) - \eta_t \Delta \overline{\mathbf{B}}. \quad (1.2.11)$$

### 2.3 Axisymmetric Equation

The axisymmetric assumption is a good simplification for the solar magnetic field, because the sun rotates. The magnetic field can be decomposed to two component, toroidal field (longitudinal component  $B_\phi$ ) and poloidal field (component on the meridional plane  $B_r, B_\theta$ ) with this simplification, because when the field is axisymmetric ( $\partial/\partial\phi = 0$ ), the poloidal field  $B_r, B_\theta$  can be expressed with longitudinal component of the magnetic vector potential as,

$$B_r = \frac{1}{r \sin \theta} \frac{\partial}{\partial \theta} (A_\phi \sin \theta) \quad (1.2.12)$$

$$B_\theta = -\frac{1}{r} \frac{\partial}{\partial r} (r A_\phi). \quad (1.2.13)$$

The axisymmetric magnetic field can be expressed only with longitudinal component of the magnetic field  $B_\phi$  and vector potential  $A_\phi$  as,

$$\mathbf{B}(r, \theta, t) = \nabla \times (A_\phi(r, \theta, t) \mathbf{e}_\phi) + B_\phi(r, \theta, t) \mathbf{e}_\phi. \quad (1.2.14)$$

We can derive the equations for both toroidal and poloidal field from the magnetic induction equation (1.2.1) as,

$$\begin{aligned} \frac{\partial B_\phi}{\partial t} = & -\frac{1}{r} \frac{\partial}{\partial r} (r v_r B_\phi) - \frac{1}{r} \frac{\partial}{\partial \theta} (v_\theta B_\phi) + r \sin \theta \mathbf{B}_p \cdot \nabla \Omega \\ & + \frac{1}{r} \frac{\partial \eta}{\partial r} \frac{\partial}{\partial r} (r B_\phi) + \frac{1}{r^2} \frac{\partial \eta}{\partial \theta} \frac{1}{\sin \theta} \frac{\partial}{\partial \theta} (\sin \theta B_\phi) + \eta \left( \Delta - \frac{1}{r^2 \sin^2 \theta} \right) B_\phi \end{aligned} \quad (1.2.15)$$

$$\frac{\partial A_\phi}{\partial t} = -\frac{v_r}{r} \frac{\partial}{\partial r} (r A_\phi) - \frac{v_\theta}{r \sin \theta} \frac{\partial}{\partial \theta} (\sin \theta A_\phi) + \eta \left[ \Delta - \frac{1}{r^2 \sin^2 \theta} \right] A_\phi \quad (1.2.16)$$

Appendix C shows the detailed derivation of above equations. The first and second terms of the right side of eq. (1.2.15) denote the advection by the flow on the meridional plane. The third term denotes the dynamo term (see §2.4 in detail).

The fourth and fifth term is called the diamagnetic transport (Charbonneau, 2005). When the magnetic diffusivity is not uniform, the magnetic field is advected to the direction  $-\nabla\eta$  effectively. The sixth term denotes the magnetic diffusion. Next, the first and second terms of the right side of eq. (1.2.16) denote the advection on the meridional plane. The second term denotes the magnetic diffusion. It is clear that the axisymmetric system cannot keep the dynamo. The equation for the toroidal field (1.2.15) includes the dynamo term  $(r \sin\theta \mathbf{B}_p \cdot \nabla\Omega)$  in the third term. This term denotes the transformation from the poloidal field to the toroidal field i.e.,  $\Omega$ -effect. When this mechanism is more effective than the magnetic diffusion, the system keeps the magnetic field. On the other hand, the equation for the poloidal field (1.2.16) does not include the dynamo term which denotes the transformation from the toroidal field to the poloidal field. In this situation only the magnetic diffusion occurs and the system cannot keep the magnetic field. This situation is caused by the axisymmetry assumption. The transformation from the toroidal field to the poloidal field requires a flow which has a shear in the longitudinal direction. In the axisymmetric system, a variation along the longitudinal direction is prohibited. Therefore the axisymmetric system cannot keep the magnetic field by the dynamo. This theorem is called Cowling's anti-dynamo theorem (Cowling, 1934). The transformation from the toroidal field to the poloidal field requires some non-axisymmetric mechanisms. Parker (1955) suggested an  $\alpha\Omega$  dynamo model as a solution for this situation. The  $\alpha$ -effect and the  $\Omega$ -effect denote the generation process of poloidal and toroidal magnetic fields respectively (see §2.4 and §2.5).

## 2.4 $\Omega$ -effect (Poloidal to Toroidal)

The physical mechanism of the  $\Omega$ -effect is explained in this section. As explained in the preceding section, the third term of the right side of eq. (1.2.15),  $r \sin \theta \mathbf{B}_p \cdot \nabla \Omega$  denotes the  $\Omega$ -effect. The poloidal field is transformed to the toroidal field with the shear of the angular velocity  $\Omega$ . Fig. 4 shows the explanation of  $\Omega$ -effect. On the

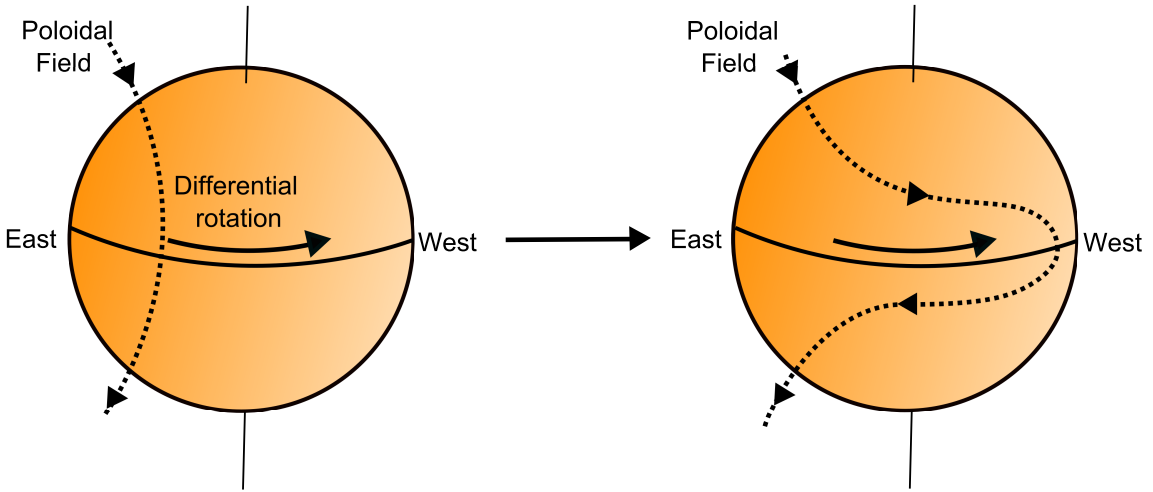


Figure 4: Schematic picture of  $\Omega$ -effect. The poloidal field is stretched by the differential rotation on the surface.

surface, the period of rotation is about 25 days in equator and about 30 days in the pole (Howard & Harvey, 1970). Though stretching the frozen-in poloidal field by the plasma flow, the toroidal field is generated (Fig. 4). The distribution of the angular velocity i.e. the differential rotation is significant information for the  $\Omega$ -effect. The  $\Omega$ -effect is thought to be the most important transformation mechanism from the kinetic energy to the magnetic energy. Almost all scientists have a consensus about this  $\Omega$ -effect.

## 2.5 $\alpha$ -effect (Toroidal to Poloidal)

As already explained in §2.3, the axisymmetric system cannot keep the dynamo, under the limitation stated by Cowling's anti-dynamo theorem. The essential difficulties are in the production of a poloidal field from a toroidal one. Several mechanisms are proposed for this process and they are called " $\alpha$ -effect" in general. Parker (1955) suggests that. The solar internal convection is affected by Coriolis force and this convection bends the toroidal magnetic field to generate the poloidal field. Fig.

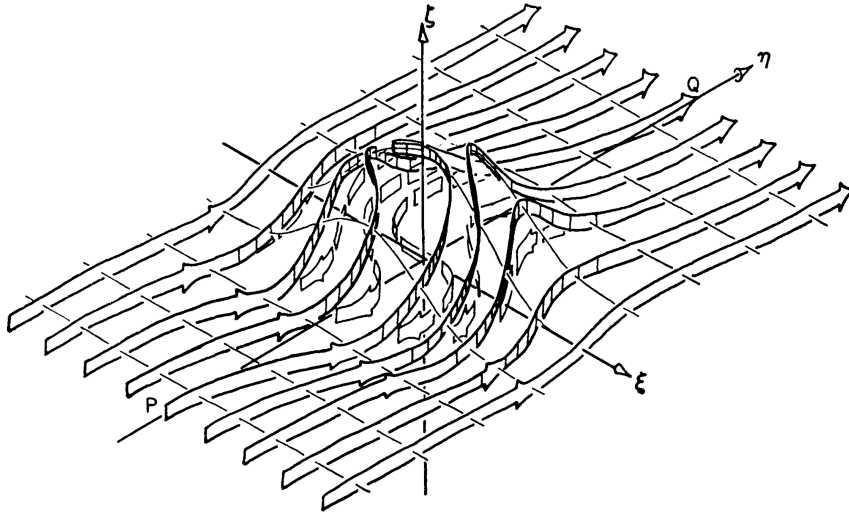


Figure 5: Parker's view of cyclonic turbulence twisting of a toroidal magnetic field. (Parker, 1955)

5 shows the physical mechanism of Parker's  $\alpha$ -effect. The convergent flow at the bottom of convection is bent to the right in northern hemisphere. This bending generates the twist like Fig 5. This mechanism occurs everywhere in the solar convection zone and the global poloidal field is generated through the reconnection between each poloidal field. The poloidal field which is generated by this  $\alpha$ -effect is assumed to

be proportional to the toroidal field. The term  $\alpha B_\phi$  is added to eq. (1.2.16) as,

$$\frac{\partial A_\phi}{\partial t} = -\frac{v_r}{r} \frac{\partial}{\partial t}(rA_\phi) - \frac{v_\theta}{r \sin \theta} \frac{\partial}{\partial \theta}(\sin \theta A_\phi) + \eta \left[ \Delta - \frac{1}{r^2 \sin^2 \theta} \right] A_\phi + \alpha B_\phi. \quad (1.2.17)$$

The combination of eqs. (1.2.15) and (1.2.17) is called dynamo equation. The amount of energy which is transformed from kinetic one to magnetic one is not so large compared with that of the  $\Omega$ -effect. The  $\alpha$ -effect is a significant mechanism for the polarity reversal of the solar cycle. There is no stringent consensus among the dynamo researches on the dominant process as for the generation of the poloidal field. Dikpati et al. (2003) suggested the  $\alpha$ -effect by the hydrodynamic instability and Ferriz-Mas et al. (1994) suggested the magnetohydrodynamic instability for the  $\alpha$ -effect. In addition, there is an important  $\alpha$ -effect confirmed by the observation i.e. Babcock-Leighton  $\alpha$ -effect (Babcock, 1961; Leighton, 1969). The sunspots pair which obeys the Joy's law diffuses and generates global poloidal magnetic field. This mechanism is important for this master thesis so the detailed explanation is given in §4.1.

## 2.6 Dynamo Wave

Parker (1955) and Yoshimura (1975) suggested that there is a kind of waves called dynamo wave, in the mean field model with the differential rotation and the  $\alpha$ -effect. We explain this dynamo wave in Cartesian coordinate which is shown in Fig. 6. When we assume that there is no meridional flow  $\mathbf{v}_p = (v_x, v_z) = 0$  and the differential rotation has only the shear of  $z$ -direction i.e.  $v_y (= r \sin \theta \Omega)$  depends only on  $z$ , the dynamo equation in axisymmetric system ( $\partial/\partial y = 0$ ), can be expressed as

$$\left[ \frac{\partial}{\partial t} - \eta_t \nabla^2 \right] B_y = \frac{dv_y}{dz} \frac{\partial A_y}{\partial x}, \quad (1.2.18)$$

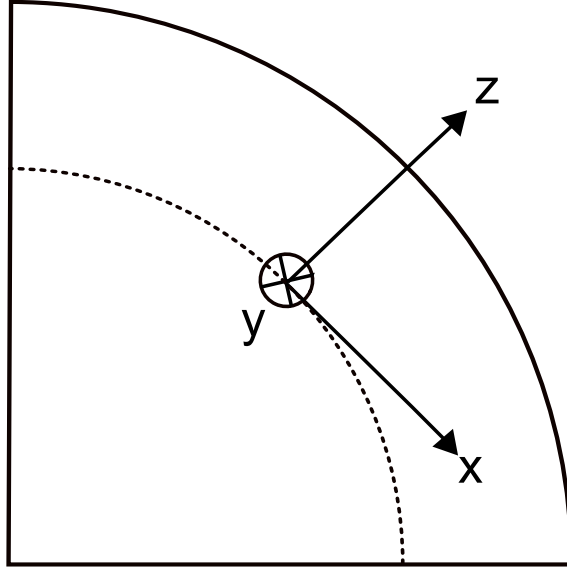


Figure 6: Local Cartesian coordinate to explain the dynamo wave.

$$\left[ \frac{\partial}{\partial t} - \eta_t \nabla^2 \right] A_y = \alpha B_y. \quad (1.2.19)$$

We assume  $\alpha$ ,  $\eta_t$  and  $dv_y/dz$  as constants. From these, we obtain,

$$\left[ \frac{\partial}{\partial t} - \eta_t \nabla^2 \right]^2 A_y = \alpha \frac{dv_y}{dz} \frac{\partial A_y}{\partial x}. \quad (1.2.20)$$

Taking a solution in a form,

$$A_y = A_0 \exp[i\omega t + i(k_x x + k_z z)], \quad (1.2.21)$$

we can obtain the dispersion relation of the dynamo wave,

$$i\omega = \eta_t k^2 \left[ -1 \pm (1 \pm i) \left( \frac{\alpha k_x}{2\eta_t^2 k^4} \frac{dv_y}{dz} \right)^{\frac{1}{2}} \right], \quad (1.2.22)$$

where  $k^2 = k_x^2 + k_z^2$ . We define non-dimensional number, dynamo number as

$$N_D = \frac{\alpha k_x}{2\eta_t^2 k^4} \frac{dv_y}{dz}. \quad (1.2.23)$$

Eq. (1.2.22) has two  $\pm$ . It means that this equation has four solutions. When  $N_D > 0$ , the real part of  $i\omega$  can be expressed as

$$Re(i\omega) = \eta_t k^2 (-1 \pm N_D^{\frac{1}{2}}). \quad (1.2.24)$$

When the real part of  $i\omega$  is negative, the solution decays. We should take a positive value for the real part of  $i\omega$  for the solution of the dynamo wave as,

$$Re(i\omega) = \eta_t k^2 (-1 + N_D^{\frac{1}{2}}). \quad (1.2.25)$$

When  $N_D < 0$ , we should take a solution which does not decay and eq. (1.2.22) should be expressed as,

$$i\omega = \eta_t k^2 [-1 + (1 \pm i)|N_D|^{\frac{1}{2}}]. \quad (1.2.26)$$

Above two solutions can be expressed as the dynamo wave. The double sign in eq. (1.2.26) is  $+$  ( $-$ ), when  $N_D > 0$  ( $N_D < 0$ ). The magnetic field is amplified (dissipated) with  $|N_D| > 1$  ( $|N_D| < 1$ ). The phase velocity of the dynamo is  $-Re(\omega)/k_x = \pm|N_D|^{\frac{1}{2}}$ , where the double sign's rule is the same as that for eq. (1.2.26). The dynamo wave propagates the negative (positive)  $x$ -direction with  $N_D > 0$  ( $N_D < 0$ ). We assume that  $\eta_t$  and  $k_x$  are positive. Therefore the dynamo wave propagates poleward (equatorward) when  $\alpha dv_y/dz$  is positive (negative). This is called Parker-Yoshimura's sign rule. In general, the direction of the dynamo wave propagation is expressed as,

$$\mathbf{s} = \alpha \nabla \Omega \times \mathbf{e}_\phi. \quad (1.2.27)$$

It means that the dynamo wave propagate along the contour line of the angular velocity in meridional plane.

We explain the physical process of the dynamo wave with Fig. 7. We assume the positive  $\alpha$ -effect and the positive radial shear of the angular velocity,  $\partial\Omega/\partial r$ . In the stage 1, there is a positive toroidal field around the shear layer. Then in the stage 2, the clockwise poloidal field is generated with the positive  $\alpha$ -effect. This poloidal field corresponds to the positive (negative) radial field in the mid (low) latitude. In the stage 3, the positive poloidal (negative) toroidal field is generated by the positive  $\partial\Omega/\partial r$ , i.e.  $\Omega$ -effect. As a result, the generated toroidal field in the low latitude cancels the initial toroidal field. On the other hand, the generated toroidal field in the mid-latitude is the same as that of the initial toroidal field. It means that the toroidal and poloidal field propagate to higher latitude. In this situation,  $\alpha dv_y/dz > 0$ , Parker-Yoshimura's sign rule says that the dynamo wave propagates poleward. This is consistent with our explanation. The dynamo wave with a constant amplitude occurs with  $|N_D| = 1$  and its period is evaluated as,

$$P = \frac{2\pi}{\omega} = \frac{2\pi}{\eta_t k^2}. \quad (1.2.28)$$

In solar case, we can use the values for the turbulent diffusivity and the wave number as  $\eta_t = 1 \times 10^{13} \text{ cm}^2 \text{ s}^{-1}$  and  $k = 1/(2 \times 10^{10}) \text{ cm}^{-1}$ . We specify the wave number as the reciprocal of the depth of the convection zone ( $\sim 2 \times 10^{10} \text{ cm}$ ). The period of the dynamo wave can be evaluated as  $P \sim 2 \times 10^8 \text{ s} \sim 7 \text{ year}$ . This is consistent with the period of solar cycle.

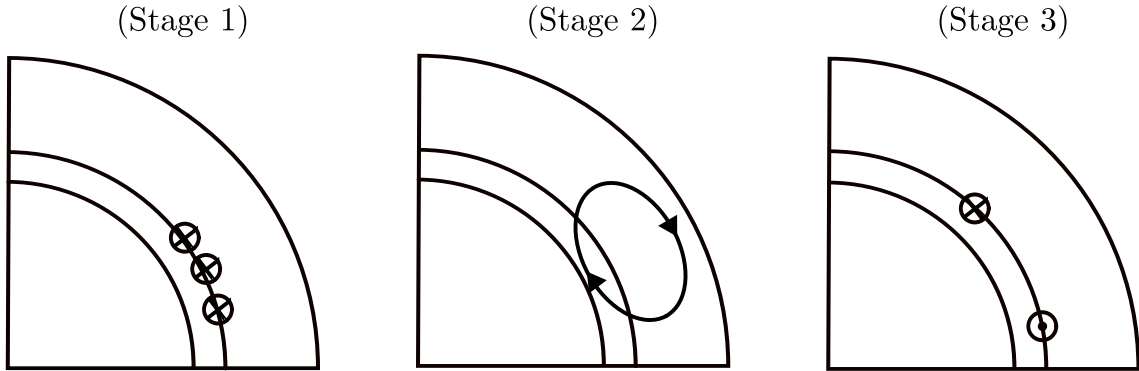


Figure 7: Schematic picture of the dynamo wave.

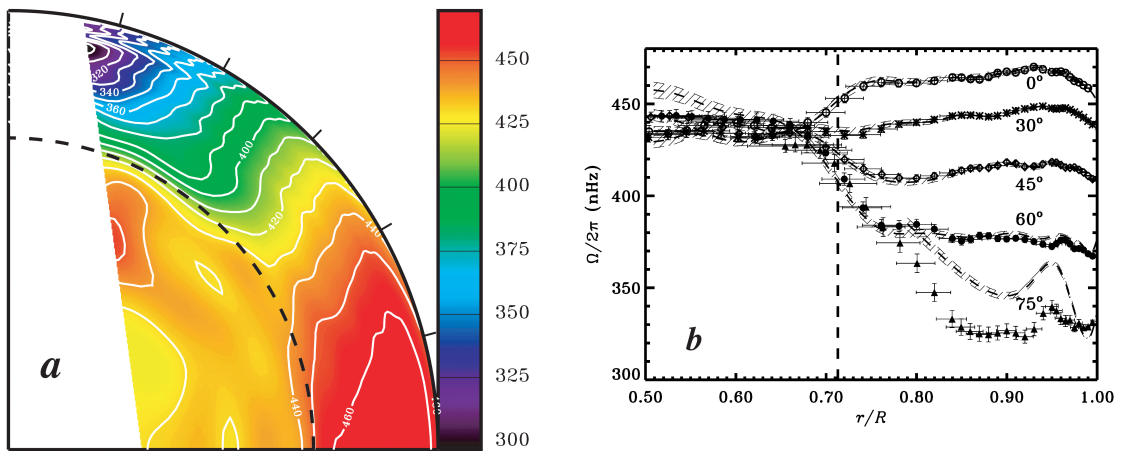


Figure 8: (a) the distribution of the latitudinally averaged angular velocity in meridional plane is shown. (b) the radial profile of angular velocity for several selected latitudes (symbols, with  $1\sigma$  error bars) is shown. (Thompson et al., 2003; Miesch, 2005)

## 3 Solar Large Scale Flow

### 3.1 Differential Rotation

The information on the internal structure of the sun, especially that of the differential rotation profile is an important element for the dynamo process. It has been revealed recently by the helioseismology (a review by Thompson et al. (2003)). Fig. 8 shows that the rotation rate decreases monotonically toward the poles by about 30%. Angular velocity contours at mid-latitudes are nearly radial. Near the base of the convection zone, there is a sharp transition between differential rotation in the convective envelope and nearly uniform rotation in the radiative interior. This transition region has become known as the solar tachocline. The tachocline is thought to be a main region where the  $\Omega$ -effect is working. This result was unexpected because the Taylor-Proudman theorem says that under certain condition, the fluid velocity will be uniform along any line parallel to the axis of rotation. The solar internal differential rotation revealed by the helioseismology is not in the Taylor-Proudman state. These structure of the differential rotation is thought to be generated by the latitudinal entropy gradient at the base of the convection zone. A detailed explanation is given in §V.

The distribution of the angular velocity determines the direction of the dynamo wave propagation. The low-latitude part of the tachocline has a positive radial shear of the angular velocity i.e.  $\partial\Omega/\partial r > 0$ . The dynamo wave propagate poleward with a positive (negative)  $\alpha$ -effect in the northern (southern) hemisphere. This behavior of the dynamo wave is not consistent with the observational result i.e. the butterfly diagram. We must reconstruct the dynamo model with this unexpected result of

the helioseismology.

Note that there is a shear layer near the surface where the gradient  $\partial\Omega/\partial r < 0$  in low latitude. In this region, the dynamo wave can propagate equatorward and this behavior is consistent with the observational result. Although we cannot rule out this equatorward dynamo wave near the surface in the low latitude, this model has a problem in phase between polar field and active region (Dikpati et al., 2002). In this thesis we will not discuss it.

## 3.2 Meridional Flow

The existence of the meridional flow ( $\bar{v}_r, \bar{v}_\theta$ ) was found by means of Doppler observation, the tracer techniques and the local helioseismology. These observations show that there is a poleward flow whose velocity is  $10 - 20 \text{ cm s}^{-1}$  in both hemispheres. The distribution of the meridional flow in polar region is unknown. Fig. 9 shows the distribution of the meridional flow. In the deep interior of the sun (under about 20 Mm), The distribution of the meridional flow is not well-known (Giles et al., 1997). Although the location of the return flow is the crucial information for the solar dynamo, there is not a consensus between the studies. The meridional flow is the consequence of the angular momentum transport. The detailed explanation of it is given in §V.

# 4 Flux-Transport Dynamo

## 4.1 Babcock-Leighton $\alpha$ -effect and Flux Emergence

In the  $\alpha\Omega$  dynamo, the toroidal field is assumed to stay in the convection zone for relatively long time compared with solar cycle. Then the interaction between

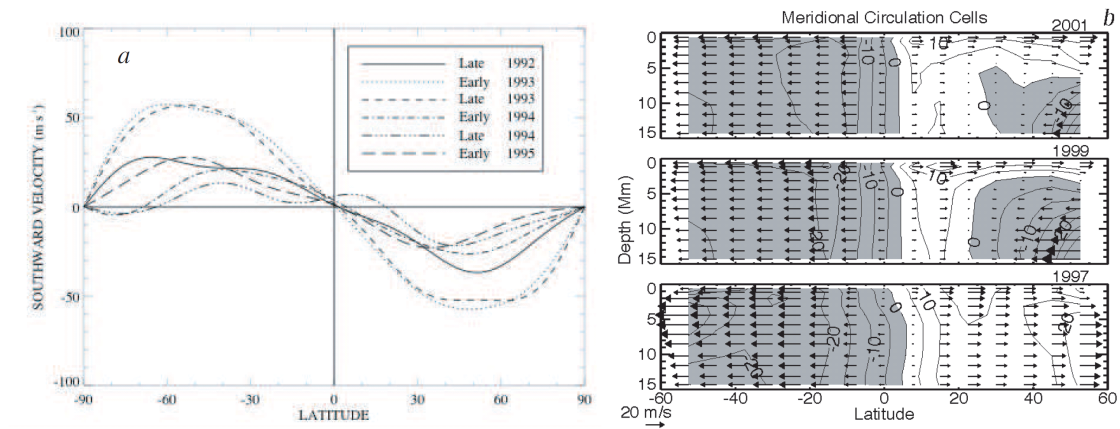


Figure 9: Spatial and temporal variation of the meridional circulation in the surface layers of the Sun. (a) The colatitudinal velocity  $\langle v_\theta \rangle$  in the solar photosphere obtained from Doppler measurements, averaged over longitude and time. Positive values represent southward flow and different curves correspond to adjacent 6-month averaging intervals between 1992 and 1995 (Hathaway et al., 1996). (b)  $\langle v_\theta \rangle$  as a function of latitude and depth. Grey and white regions represent southward and northward flow, respectively. A contour plot of the velocity amplitude underlies the arrow plots, with contours labeled in  $\text{m s}^{-1}$  (Haber et al., 2002). See also Miesch (2005).

the toroidal field and the convection generates the global poloidal field i.e., the turbulent  $\alpha$ -effect. Parker (1975) suggested that the amplified toroidal field takes only one month to rise to the solar surface by the magnetic buoyancy, so there is not enough time for the toroidal field to generate poloidal field by the turbulent  $\alpha$ -effect. Moreno-Insertis (1983) confirmed this theory by the numerical calculation of the thin flux tube (see also Fan, 2009a,b). Due to the fact that the turbulent  $\alpha$ -effect is not ineffective in the solar convection zone, many studies suggest that the Babcock-Leighton  $\alpha$ -effect is significant. Babcock (1961) argued that the sunspots pair which obey the Joy's law and tilted to the equator generates the global poloidal field through reconnections. This mechanism is shown in Fig. 10. Leighton (1969) calculated numerically the solar cycle using this effect and confirmed that the eleven-year cycle can be reproduced. Thus this effect is called Babcock-Leighton  $\alpha$ -effect. The calculation of Leighton (1969) used an unreal differential rotation which is not consistent with the result of the helioseismology, but the regeneration process on the surface is important for the solar dynamo until now. Wang & Sheeley (1991) suggested that the Babcock-Leighton  $\alpha$ -effect is caused by the Coriolis force which operates on the flux tube: when the flux tube rises to the surface, the flux tube expand as it rises due to a reduction of the gas pressure. This expanding motion is bend by the Coriolis force and generates the poloidal component of the magnetic field. This mechanism is shown in Fig. 11. When the tilt is caused by the Coriolis force, the dependence of the tilt angle should show the dependence  $\propto \cos \theta$ . This is consistent with observational result. D'Silva & Choudhuri (1993) confirmed this theory with the numerical calculation of the thin flux tube. According to above theoretical and observational studies, the Babcock-Leighton  $\alpha$ -effect is thought to

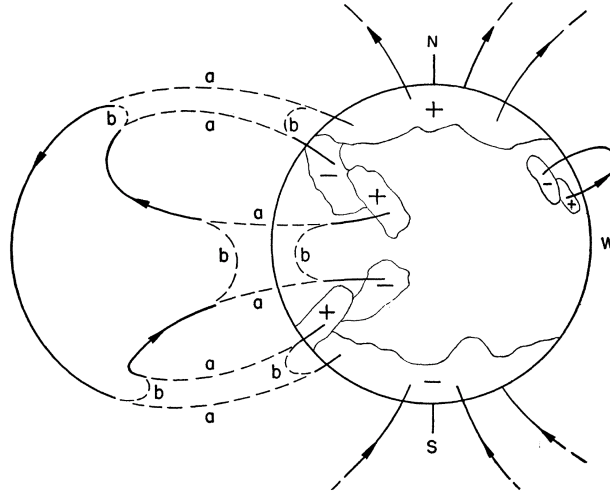


Figure 10: The Babcock-Leighton mechanism of poloidal field production from the decay of bipolar active regions showing opposite polarity patterns in each solar hemisphere (Babcock, 1961).

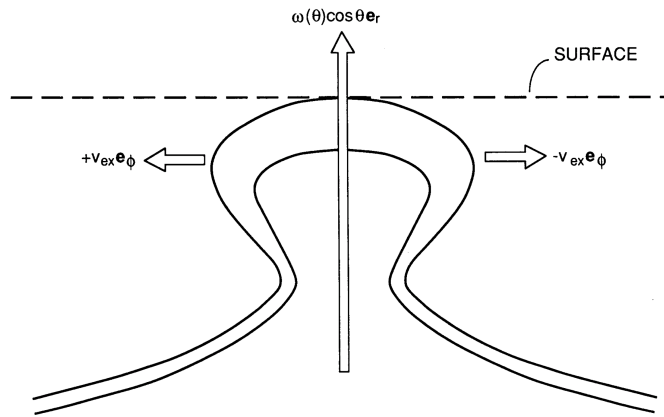


Figure 11: A buoyant flux loop rises to the solar surface, expanding in the longitudinal direction. The flux tube is bent by the Coriolis force.

be important.

In this master thesis, we carried out the studies in Part III and Part IV by adopting this Babcock-Leighton  $\alpha$ -effect for the poloidal-field generation mechanism. Note that, however, we are not claiming that the Babcock-Leighton mechanism is the only one which can explain the observations. We cannot rule out the  $\alpha$ -effect operated near the overshoot region between the convection zone and the radiative zone.

## 4.2 General Property of Flux-Transport Dynamo

The flux-transport dynamo is suggested to explain the observational result of the solar magnetic cycle. Toroidal magnetic field is generated by the  $\Omega$ -effect in the shear layer, i.e. the tachocline and poloidal field is generated near the surface by the Babcock-Leighton  $\alpha$ -effect. As explained, when these regions are connected by the diffusion, the dynamo wave propagates poleward due to the positive shear of the angular velocity i.e.,  $\partial\Omega/\partial r > 0$  and the positive  $\alpha$ -effect. This behavior is not consistent with the butterfly diagram. The flux-transport dynamo solves this problem by incorporating the meridional flows. The meridional flow which is in poleward near the surface is thought to be in equatorward due to the conservation of mass (van Ballegoijen & Choudhuri, 1988). This equatorward meridional flow near the base of the convection zone transports the magnetic field to the equator against the poleward dynamo wave (Choudhuri et al., 1995). Dikpati & Charbonneau (1999) built the basic idea of the flux-transport dynamo: Fig. 12 shows the processes of the flux-transport dynamo. In the stage 1, the toroidal field amplified by the  $\Omega$ -effect in the tachocline begins to rise to the solar surface due to the magnetic buoyancy. In

the stage 2, the Coriolis force bends the toroidal magnetic field and generates the poloidal field during the rising motion (Babcock-Leighton  $\alpha$ -effect). In the stage 3, the generated poloidal field is transported by the meridional field to the tachocline. In the stage 4, the toroidal field is generated again by the  $\Omega$ -effect in the tachocline from the transported poloidal field. This flux-transport dynamo can explain some

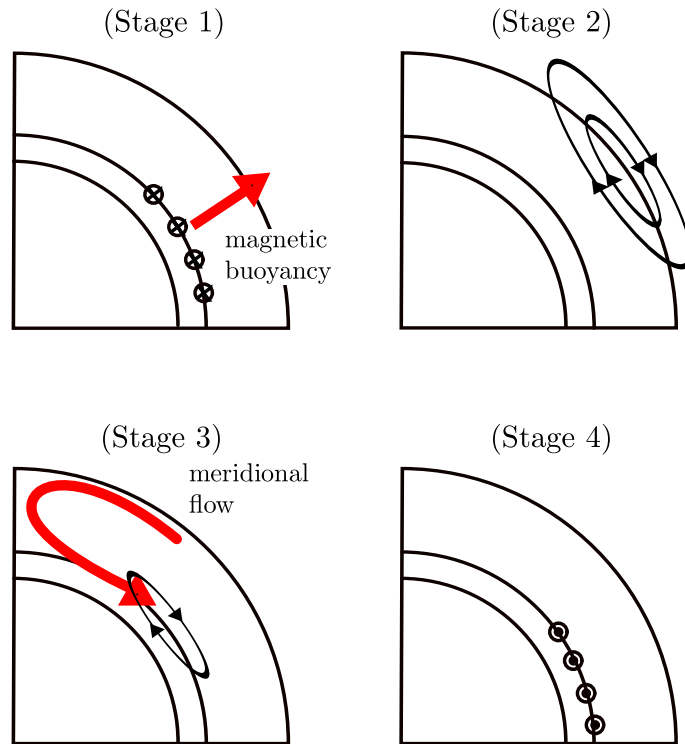


Figure 12: The schematic picture of flux-transport dynamo

features of the solar cycle: The poleward migration of the general field can be explained by the transportation of the poloidal field by the meridional flow. The equatorward migration of the active region can be explained by the transport of the toroidal field through the equatorward meridional flow near the base of the convection zone. Dikpati & Charbonneau (1999) reported the relation between the parameters

and the solar cycle period  $P_{\text{cyc}}$  as,

$$P_{\text{cyc}} = 56.8v_0^{-0.89}s_0^{-0.13}\eta_t^{0.22}, \quad (1.4.1)$$

where  $s_0$  is the amplitude of the  $\alpha$ -effect. This result shows that the period significantly depends on the meridional flow. When the meridional flow is fast, the period is short.

## 5 Overview of this Thesis

In this thesis, we carried out researches on the issues on solar dynamo based on the mean field model. Part II is the specific introduction for Part III and IV, we introduce the importance of the turbulent diffusivity. The prediction of the next solar maximum significantly depends on the distribution of the turbulent diffusivity, since the amplitude of the turbulent diffusivity differentiates the advection- and diffusion-dominated regime of the flux-transport dynamo. Part III is for the study on the problematic features of the flux-transport dynamo. In the flux-transport dynamo model the strong polar field is generated by the converging motion of the meridional flow and the strong toroidal field is generated by the  $\Omega$ -effect at the high-latitude of the base of convection zone. These strong fields are not consistent with observations. To solve these, we develop a new regime of the flux-transport dynamo model with strong turbulent diffusivity near the surface. Part IV is for the study on the parity of the solar global magnetic field. The sun has distinct parity, i.e., dipole. It is known that the parity of the magnetic field is depends on free parameters especially in turbulent diffusivity in flux-transport dynamo model. We carried out the parameter study for the magnetic parity to have a insight of

the internal structure of the turbulent diffusivity. Part V is for the study on the differential rotation in rapidly rotating stars. As explained, the differential rotation is the essential factor for the solar dynamo. We investigate the morphology of the differential rotation in rapidly rotating stars.

## Part II

# Turbulent Diffusion and Prediction of Next Maximum

Dikpati & Gilman (2006) and Choudhuri et al. (2007) have predicted the next solar maximum based on the kinematic solar flux-transport dynamo model. These studies show that the amplitude of the solar cycle depends on various parameters among which the most important is the turbulent diffusivity. Two prediction studies whose results are significantly different are introduced in this section to emphasize the importance of the distribution of the turbulent diffusivity.

Fig. 13 shows the result of the prediction based on Dikpati & Gilman (2006) model. This result shows that their model can reproduce the past solar cycle and the next solar maximum (cycle 24) is stronger than that of cycle 23.

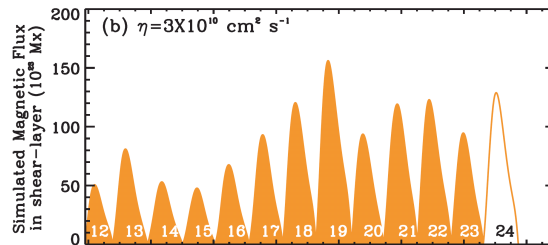


Figure 13: Prediction of Dikpati & Gilman (2006) model

On the other hand, Choudhuri et al. (2007) suggested a different prediction (see also Jiang et al., 2007). Fig. 14 shows their result. Their model can also reproduce the past solar cycle, but their model suggested that the cycle 24 is weaker than that of the cycle 23.

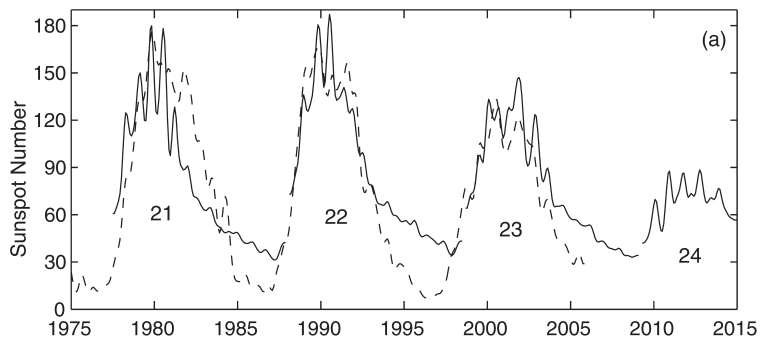


Figure 14: Prediction of Choudhuri et al. (2007) model

We explain the reason to generate this difference between the results of these models. Dikpati & Gilman (2006) and Yeates et al. (2008) claimed that this difference is caused by the difference of the turbulent diffusivity. Fig. 15 shows the relation between the amplitude of the turbulent diffusivity, time and the thickness of the layer where the turbulent diffusivity is in charge. Dikpati & Gilman (2006) assumed the amplitude of the turbulent diffusivity  $10^{10}$ - $10^{11}$   $\text{cm}^2 \text{s}^{-1}$  in the convection zone, thus the magnetic field takes more than thirty years to diffuse. It means that the amplitude of  $n$ th cycle is determined by the  $(n - 1)$ th,  $(n - 2)$ th and  $(n - 3)$ th cycle. On the other hand, Choudhuri et al. (2007) assumed the amplitude of the turbulent diffusivity about  $10^{12}$   $\text{cm}^2 \text{s}^{-1}$  in the convection zone, thus the magnetic field takes about ten years to diffuse. Therefore the  $n$ th cycle is determined only by the  $(n - 1)$ th cycle, so the model of Choudhuri et al. (2007) can reproduce the relation between the polar field and the number of sunspots. Therefore it is important for the solar prediction to understand the distribution of the turbulent diffusivity in the solar convection zone. Meanwhile Yeates et al. (2008) gave a interesting suggestion about the turbulent diffusivity. The flux-transport dynamo has two regime i.e.

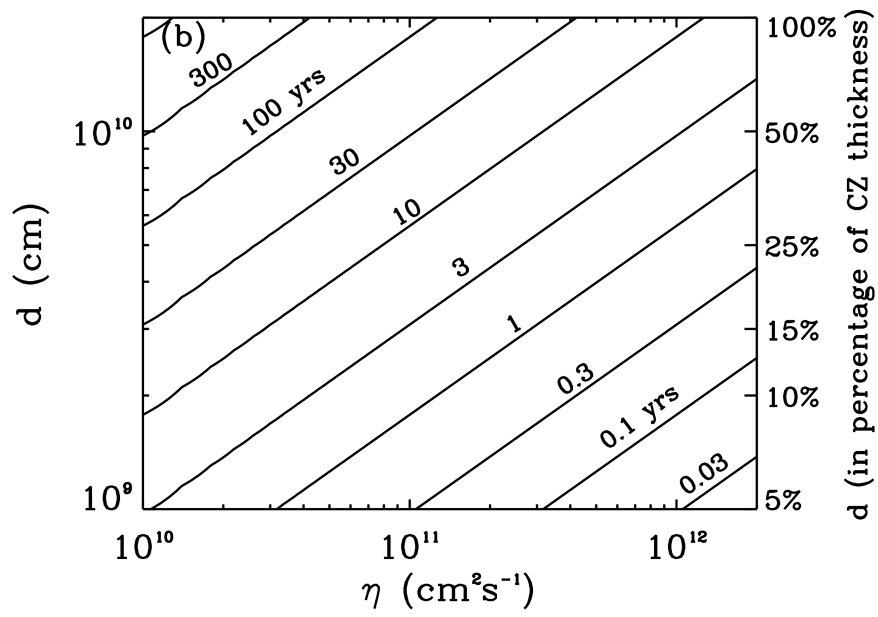


Figure 15: Contours in the diffusion-time plane show the time taken by the poloidal fields to diffuse down to a certain depth from the surface

advection-dominated and diffusion-dominated.

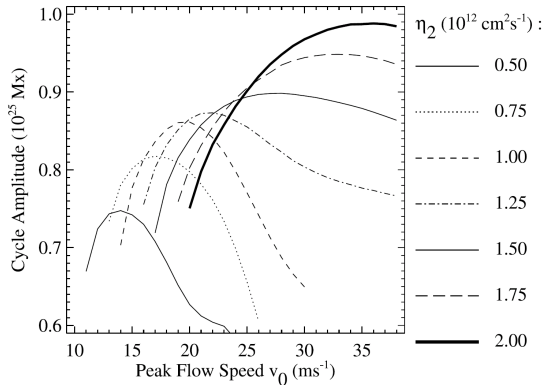


Figure 16: Dependence of cycle amplitude on the meridional circulation speed  $v_0$ . Each line style corresponds to a different value of  $\eta_{\text{yeates}}$  (the poloidal diffusivity in the convection zone) as given in the legend.

Fig. 16 shows the relation between the amplitude of the meridional flow and the cycle amplitude. When the meridional flow is slow, the cycle amplitude becomes strong as the meridional flow becomes fast. On the other hand, when the meridional flow is relatively fast, the cycle amplitude becomes weak as the meridional flow becomes fast. The similar thing occurs in the relation between the amplitude of the turbulent diffusivity and the cycle amplitude (Fig. 17). Yeates et al. (2008) said that when the meridional flow is relatively slow, the regime is diffusion-dominated. In this situation, the fast meridional flow means that the short diffusion time by the turbulence. When the regime is the advection-dominated, the fast meridional flow means the short amplification time of the  $\Omega$ -effect. In this way, the behavior of the flux-transport dynamo is significantly different between these two regime. Yeates et al. (2008) said that the model of Dikpati & Gilman (2006) is advection-dominated regime and that of Choudhuri et al. (2007) is diffusion-dominated regime.

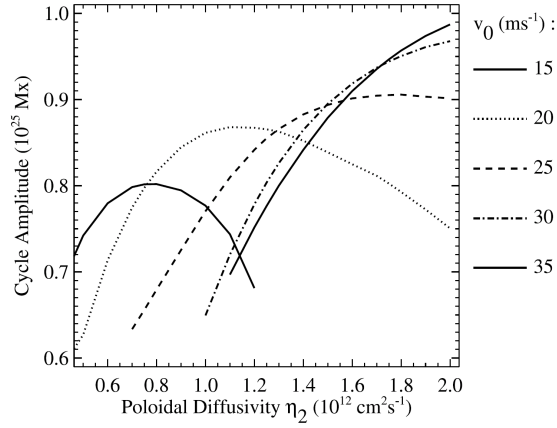


Figure 17: Dependence of cycle amplitude on the poloidal diffusivity  $\eta_{\text{yeates}}$  in the convection zone. Each line style corresponds to a different value of the meridional circulation speed  $v_0$ , as given in the legend.

Therefore it is very important to know the distribution of the turbulent diffusivity in the solar convection zone, but it is difficult to observe it and calculate it from the first principle by the ability of the current computer. In this master thesis, we give some indications on the distribution of the turbulent diffusivity.

## Part III

# Importance of Surface Turbulent Diffusivity

## 6 Introduction

After the helioseismology revealed the internal differential rotation and the meridional flow, recent dynamo models have been constructed on this observation, including the new process, i.e. the flux transport by the meridional flow (Choudhuri et al., 1995; Dikpati & Charbonneau, 1999; Küker et al., 2001). This flow transports poloidal fields generated on the surface by the  $\alpha$  effect to the tachocline where the toroidal field is generated by the  $\Omega$  effect. It is called the “flux-transport dynamo”. This model succeeded to reproduce the solar cycle basic features, i.e. the poleward drifting of poloidal fields on the surface and the equatorward migrating of toroidal fields at the base of the convection zone. Note that Yeates et al. (2008) recently pointed out the importance of the diffusion in transporting the flux (see also Jiang et al., 2007; Choudhuri & Karak, 2009).

In the flux transport dynamo, however, there are two problematic features which do not agree with the observations. The first is strong poloidal fields at the pole on the surface. The observations indicate that the polar fields are of strength  $\sim 10$  G in average (Tsuneta et al., 2008), whereas the previous models reproduced about 400 G fields (e.g. Dikpati & Charbonneau, 1999; Charbonneau, 2005). This is due to the concentration of the poloidal magnetic flux by the converging motion of the meridional flow into the pole. It is not avoidable to make such strong poloidal fields in the dynamo model with the transport of the meridional flow. The other is a

generation of strong toroidal fields at the high latitude at the base of the convection zone. This is due to the efficient transport of the poloidal field by the meridional flow as well as by the stretching motion of the strong shear at the high latitude. This strong toroidal field would emerge to become high-latitude sunspots, which is inconsistent with the observations.

Nandy & Choudhuri (2002) avoided strong toroidal fields near the pole by the deep penetration of the meridional flow below the tachocline where the magnetic fields can not rise due to the subadiabatic restoring force. But the depth of the penetration of the meridional flow is still controversial. Guerrero & de Gouveia Dal Pino (2007) were able to avoid strong toroidal fields at the high latitude by using the thin ( $\sim 0.02R_{\odot}$ ), where  $R_{\odot}$  is the solar radius. tachocline in which the  $\Omega$  effect is relatively ineffective. Dikpati et al. (2004) used the “tachocline  $\alpha$  effect” (See also Dikpati & Gilman, 2001) and obtained the result which agrees with the observations, especially weak polar radial fields ( $\sim 30$  G) and the absence of the strong magnetic field at the tachocline at the high latitude.

In this study we introduce a new regime in which we can avoid the above two problematic features of the flux transport dynamo and can reproduce the equatorward-migrating sunspots. We use the strong diffusivity ( $\sim 10^{13}$  cm<sup>2</sup> s<sup>-1</sup>) above  $r = 0.8R_{\odot}$  and the relatively weak diffusivity ( $\sim 10^{10}$  cm<sup>2</sup> s<sup>-1</sup>) in  $r = 0.7R_{\odot} - 0.8R_{\odot}$ . Therefore our regime is diffusion-dominated only near the surface while advection-dominated around the base of the convection zone. The relative localization of the diffusion near the surface is essential for this model. In §7 our model is described. In §8 we show the reference numerical demonstrate solution to explain the achievement of our dynamo model. In §9 we show the results of

parameter-space studies. The cases with the shallow meridional flow are shown in §10. We discuss about the distribution of the  $\alpha$  effect in §11. We conclude in §12.

## 7 Model

### 7.1 Basic Equations

In this study, we solve the kinematic mean field dynamo problem. An axisymmetric magnetic field can be expressed in the spherical coordinate  $(r, \theta, \phi)$  as (see also §2.3)

$$\mathbf{B} = B_\phi(r, \theta)\mathbf{e}_\phi + \mathbf{B}_p \quad (3.7.1)$$

where  $B_\phi(r, \theta)$  and  $\mathbf{B}_p = \nabla \times [A_\phi(r, \theta)\mathbf{e}_\phi]$  correspond to the toroidal and poloidal components, respectively.  $A_\phi$  is the  $\phi$  component of the vector potential. The mean field induction equation then leads to the following standard forms for the  $\alpha$ - $\Omega$  dynamo problem, i.e.

$$\begin{aligned} \frac{\partial B_\phi}{\partial t} + \frac{1}{r} \left[ \frac{\partial}{\partial r}(rv_r B_\phi) + \frac{\partial}{\partial \theta}(v_\theta B_\phi) \right] \\ = r \sin \theta (\mathbf{B}_p \cdot \nabla) \Omega - (\nabla \eta \times \nabla \times B_\phi \mathbf{e}_\phi) \cdot \mathbf{e}_\phi \\ + \eta \left( \nabla^2 - \frac{1}{r^2 \sin^2 \theta} \right) B_\phi, \end{aligned} \quad (3.7.2)$$

$$\begin{aligned} \frac{\partial A_\phi}{\partial t} + \frac{1}{r \sin \theta} (\mathbf{v} \cdot \nabla)(r \sin \theta A_\phi) \\ = \eta \left( \nabla^2 - \frac{1}{r^2 \sin^2 \theta} \right) A_\phi + S(r, \theta; B_\phi). \end{aligned} \quad (3.7.3)$$

We specify the meridional flow  $\mathbf{v} = v_r \mathbf{e}_r + v_\theta \mathbf{e}_\theta$ , the differential rotation  $\Omega$ , and the turbulent diffusivity  $\eta$ . A source term  $S(r, \theta; B)$  is artificially added to the right-hand side of equation (3.7.3). This source term describes the generation of poloidal fields at the solar surface from the decay of bipolar sunspots. This is the so-called

‘Babcock-Leighton  $\alpha$  effect’ (Babcock, 1961; Leighton, 1969). We describe below how we specify  $\mathbf{v}, \Omega, \eta$  and  $S$ . Once these quantities are specified, we can solve equations (3.7.2) and (3.7.3) to study the behavior of the dynamo kinematically.

## 7.2 Differential Rotation

The formula for the differential rotation is given as

$$\Omega(r, \theta) = \Omega_c + \frac{1}{2} \left[ 1 + \operatorname{erf} \left( 2 \frac{r - r_c}{d_c} \right) \right] \{ \Omega_s(\theta) - \Omega_c \} \quad (3.7.4)$$

where  $\Omega_s(\theta) = \Omega_{\text{Eq}} + a_2 \cos^2 \theta + a_4 \cos^4 \theta$  is the surface latitudinal differential rotation and erf is the error function. The other parameters are set as  $\Omega_c/2\pi = 432.8$  nHz,  $\Omega_{\text{Eq}}/2\pi = 460.7$  nHz,  $a_2/2\pi = -62.69$  nHz,  $a_4/2\pi = -67.13$  nHz, and  $r_c = 0.7R_\odot$  and  $d_c = 0.05R_\odot$ , which closely resemble the best-fit helioseismic solution. This differential rotation profile has a purely latitudinal difference with equatorial acceleration in the convection zone. It smoothly matches across the ‘tachocline’ on the ‘core’ rotating rigidly. We specify the central radius  $r_c$  and the thickness of the tachocline  $d_c$ , and the rotating rate of the core  $\Omega_c$ . A contour plot of  $\Omega$  given by eq (3.7.4) is shown in Fig. 18. This profile is used in all our calculations in this study.

## 7.3 Meridional Flow

We now describe how the meridional flow is specified. While a poleward meridional flow is observed at the solar surface, the form of the internal return flow is at present unconstrained observationally. We choose here an analytical form suggested by van Ballegooijen & Choudhuri (1988) with the density profile in the convection zone given by  $\rho(r) = \rho_c [(R_\odot/r) - 1]^m$ , the  $r$  and  $\theta$  components of this flow are as

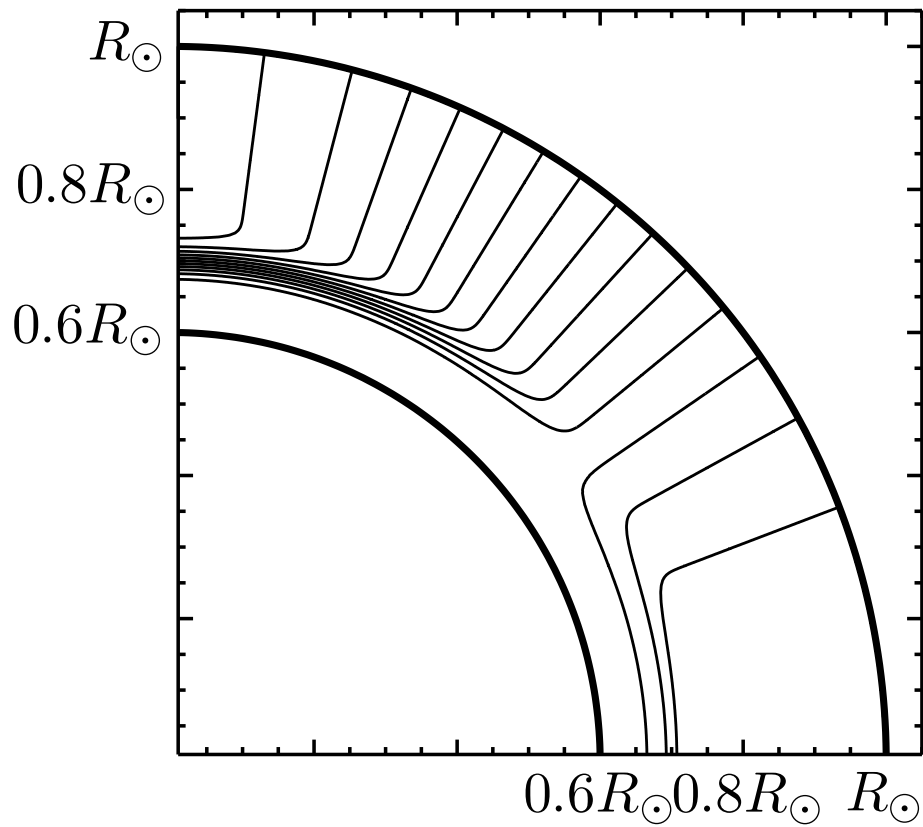


Figure 18: Contour of the angular velocity as obtained from Equation (3.7.4). This profile is used in all of our calculations in this study.

follows:

$$v_r(r, \theta) = \frac{v_0}{f} \left( \frac{R_\odot}{r} \right)^2 \times \left[ -\frac{1}{m+1} + \frac{c_1}{2m+1} \xi^m - \frac{c_2}{2m+p+1} \xi^{m+p} \right] \times \xi \sin^q \theta [(q+2) \cos^2 \theta - \sin^2 \theta] \quad (3.7.5)$$

$$v_\theta(r, \theta) = \frac{v_0}{f} \left( \frac{R_\odot}{r} \right)^3 [-1 + c_1 \xi^m - c_2 \xi^{m+p}] \times \sin^{q+1} \theta \cos \theta, \quad (3.7.6)$$

where

$$\xi(r) = \frac{R_\odot}{r} - 1, \quad (3.7.7)$$

$$c_1 = \frac{(2m+1)(m+p)}{(m+1)p} \xi_p^{-m}, \quad (3.7.8)$$

$$c_2 = \frac{(2m+p+1)m}{(m+1)p} \xi_p^{-(m+p)}, \quad (3.7.9)$$

$$\xi_p = \frac{R_\odot}{r_p} - 1. \quad (3.7.10)$$

Here we specify the amplitude of the velocity  $v_0$ , the radial and latitudinal dependence of the flow by  $p$  and  $q$ , respectively, the bottom of the meridional flow  $r_p$ , and the normalization constant  $f$  to set the maximum speed of the meridional flow of the  $\theta$  component to  $v_0$ . We use the parameter values  $m = 0.5$ ,  $p = 0.25$  and  $q = 0$ . Gilman & Miesch (2004) argued that the penetration of the meridional flow would be limited to a shallow Ekman layer close to the base of the convection zone. On the other hand Garaud & Brummell (2008) suggested that the meridional flow can penetrate deeper down into the radiative interior. At this point there is no consensus on the profile of the meridional flow in the solar interior. Therefore, we treat  $r_p$  as a free parameter. Fig. 19 shows the streamlines of the meridional circulation obtained by taking  $r_p = 0.62R_\odot$ .

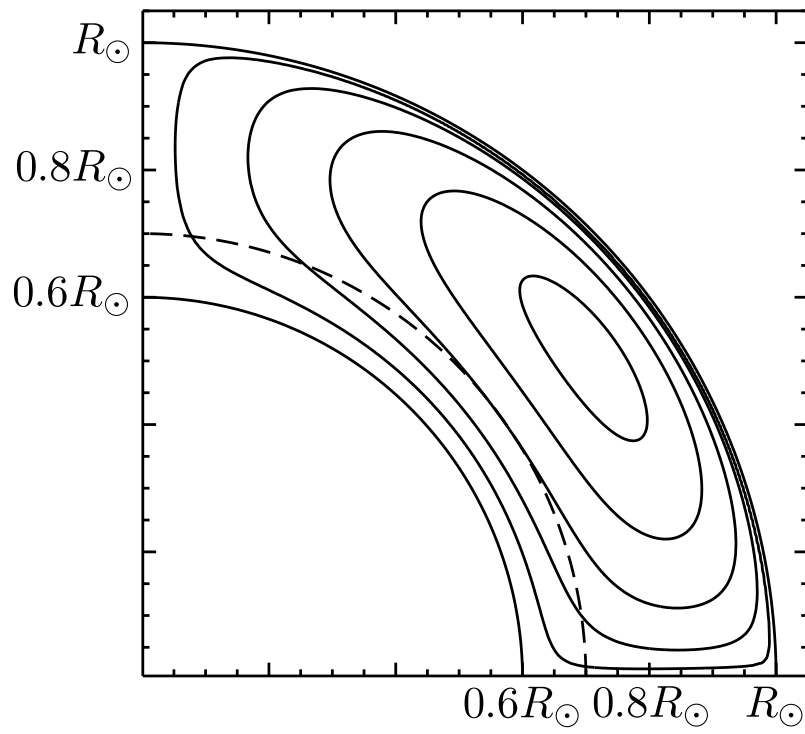


Figure 19: Streamlines of the meridional circulation of the reference case ( $r_p = 0.62R_\odot$ ). A counter-clockwise flow is assumed. The tachocline ( $r_c = 0.7R_\odot$ ) is shown by a dashed line.

## 7.4 Diffusivity

We assume that the net magnetic diffusivity in the convection zone is dominated by its turbulent contribution. Since direct measurement of the magnetic diffusivity as a function of the depth is not possible yet, the amplitude of the magnetic diffusivity in convection zone is given based on the mixing length theory (Spruit, 1974). We adopt a diffusivity profile of the form

$$\begin{aligned} \eta(r) = & \eta_{\text{core}} + \frac{\eta_t}{2} \left[ 1 + \operatorname{erf} \left( \frac{r - r_1}{d_1} \right) \right] \\ & + \frac{\eta_{\text{surf}}}{2} \left[ 1 + \operatorname{erf} \left( \frac{r - r_2}{d_2} \right) \right]. \end{aligned} \quad (3.7.11)$$

Here,  $r_1 = 0.7R_\odot$ ,  $r_2 = 0.95R_\odot$ ,  $d_1 = 0.05R_\odot$  and  $d_2 = 0.05R_\odot$ . This profile consists of three layers (Fig. 20). In the supergranular layer near the surface ( $r > r_2$ ), the diffusivity is strong and is prescribed by  $\eta_{\text{surf}}$  within  $10^{12} - 10^{14} \text{ cm}^2 \text{ s}^{-1}$ . Wang et al. (1989) argued that the surface diffusivity should be  $6 \times 10^{12} \text{ cm}^2 \text{ s}^{-1}$  for the consistency with observations. The radial range of the surface diffusive layer is slightly larger than the previous studies (e.g. Dikpati & Gilman, 2007) since we would study the diffusion-dominated regime. In the convection zone we use the fixed value  $\eta_t = 5 \times 10^{10} \text{ cm}^2 \text{ s}^{-1}$ . In the stratified core there is no turbulence (or at least, far less), so that the diffusivity is presumably much weaker. We use the value  $\eta_{\text{core}} = 5 \times 10^8 \text{ cm}^2 \text{ s}^{-1}$ .

## 7.5 Poloidal Source Term

Some parts of the toroidal field in the tachocline rise to the surface due to the magnetic buoyancy and make active regions. There is an observational evidence (Babcock, 1959) that the decay of tilted bipolar active regions can produce a substantial

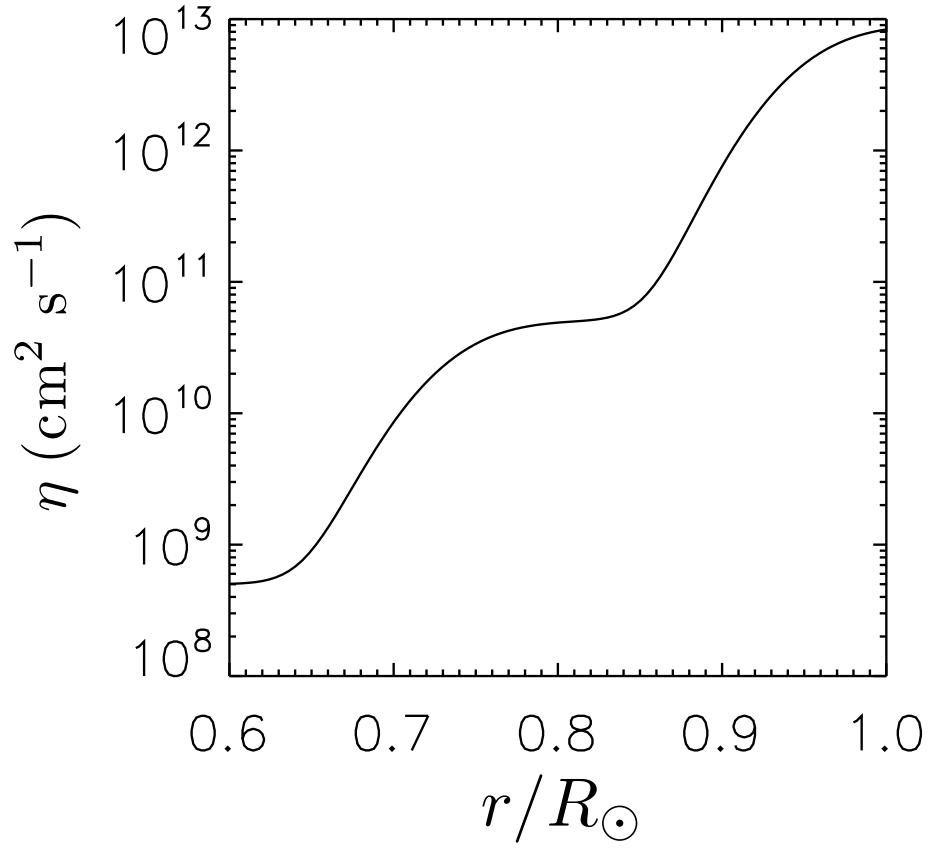


Figure 20: Diffusivity profile as a function of the radial distance for the reference case ( $\eta_{\text{surf}} = 9 \times 10^{12} \text{ cm}^2 \text{ s}^{-1}$ ).

amount of the net poloidal fields near the surface (Wang & Sheeley, 1991). It is called the ‘‘Babcock-Leighton  $\alpha$  effect’’. Based on this, we assume that the poloidal source term is taken in the form

$$S(r, \theta; B_\phi) = \alpha(r, \theta) B_\phi(r_c, \theta) \times \left[ \frac{1}{1 + (B_\phi(r_c, \theta)/B_{\text{eq}})^2} \right], \quad (3.7.12)$$

where

$$\alpha(r, \theta) = \frac{\alpha_0}{4} \times \left[ 1 + \operatorname{erf} \left( \frac{r - r_4}{d_4} \right) \right] \left[ 1 - \operatorname{erf} \left( \frac{r - r_5}{d_5} \right) \right] \times \sin \theta \cos \theta \left[ \frac{1}{1 + e^{-\gamma(\theta - \pi/4)}} \right]. \quad (3.7.13)$$

The parameters are  $r_4 = 0.95R_\odot$ ,  $r_5 = R_\odot$ ,  $d_4 = 0.05R_\odot$ ,  $d_5 = 0.01R_\odot$ ,  $\alpha_0 = 100 \text{ cm s}^{-1}$  and  $\gamma = 30$ . Fig. 21 shows the profile of the poloidal source, as functions of the colatitude (Fig. 21a) and the radius (Fig. 21b). We concentrate the  $\alpha$  effect by the last factor in eq. (3.7.13) at the low latitude in which there are many observed active regions (Dikpati et al., 2004). We use slightly wide radial range for this poloidal source to maintain the dynamo against the strong surface turbulent diffusivity. The source term is made proportional to the toroidal field strength at the same latitude at the tachocline  $r = r_c$ , the base of the convection zone since it is assumed here to be originated from the radially emerged magnetic fluxes. The ‘‘quenching’’ term  $\{1 + [B_\phi(r_c, \theta)/B_{\text{eq}}]^2\}^{-1}$  ensures that the poloidal field production rapidly vanishes as the deep toroidal field strength exceed  $B_{\text{eq}}$  (Cattaneo & Hughes, 1996), since the Coriolis force cannot bend strong magnetic field ( $> B_{\text{eq}}$ ) in the convection zone. We use a fixed value  $B_{\text{eq}} = 4 \times 10^4 \text{ G}$ , where  $B_{\text{eq}}$  is the equipartition magnetic field at the tachocline and the scale of the magnetic field as

well. All our result changes in proportion to  $B_{\text{eq}}$ . Note that some authors argue that a magnetic flux tube in the tachocline should be as strong as  $10^5$  G, while the toroidal magnetic field is only about  $10^4$  G in our results. It is not inconsistent since the magnetic field is intermittent in the tachocline and their filling factor can be  $f \sim 0.1$  (Choudhuri, 2003).

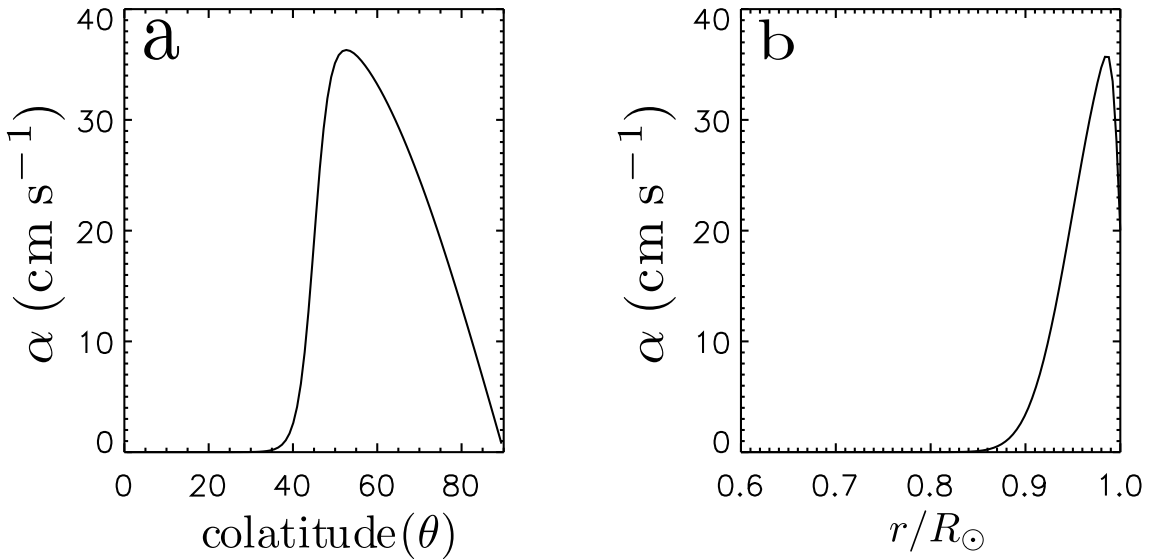


Figure 21: (a) Profile of  $\alpha$  along  $r = 0.975R_{\odot}$  as a function of the colatitude  $\theta$ . (b) Profile of  $\alpha$  at ( $\theta = 60^{\circ}$ ) as a function of  $r$ .

## 7.6 Numerical Domain and Boundary Conditions

We solve equations (3.7.2) and (3.7.3) numerically in the northern half of the meridional plane in  $0.6R_{\odot} < r < R_{\odot}$  and  $0 < \theta < \pi/2$  with the modified Lax-Wendroff scheme. We use a moderate resolution of around 100 grid points both in the radial and the latitudinal directions. The same boundary conditions as Dikpati & Charbonneau (1999) are used: At the lower boundary ( $r = 0.6R_{\odot}$ ), we set both  $B_{\phi}$  and  $A_{\phi}$  to zero, indicating that the radiative core is a perfect conductor. At the

top boundary ( $r = R_\odot$ ), we set  $B_\phi = 0$  and smoothly match  $A_\phi$  onto an exterior potential field solution (Dikpati & Choudhuri, 1994). At the pole ( $\theta = 0$ ), we set  $B_\phi = A_\phi = 0$  for the regularity. To obtain antisymmetric solutions about the equator, we set  $B_\phi = 0$  and  $\partial A_\phi / \partial \theta = 0$  at  $\theta = \pi/2$ . Each run starts from an arbitrary initial state, and then evolves until initial transients disappear, leaving a steady periodic dynamo solution. The numerical convergence is checked by runs with different grid spacings.

## 8 Reference Solution

We first show a representative reference solution, computed with the parameter values  $v_0 = 1000 \text{ cm s}^{-1}$ ,  $r_p = 0.62R_\odot$  and  $\eta_{\text{surf}} = 9 \times 10^{12} \text{ cm}^2 \text{ s}^{-1}$ . The results are shown in time-latitude plots in Fig. 22. The top panel shows the strength of the radial field at the solar surface ( $r = R_\odot$ ). This shows a poleward propagating branch with the strength at the pole  $\sim 40 \text{ G}$ . The strength is more consistent with observations than that obtained by the previous studies (e.g. Dikpati & Charbonneau, 1999). The bottom panel of Fig. 22 shows toroidal fields strength at the tachocline ( $r = 0.7R_\odot$ ). This is consistent with the solar butterfly diagram in which the latitude where strong magnetic fields appear migrates equatorward during the solar cycle. The important feature is that there is weak toroidal field ( $\sim 1000 \text{ G}$ ) at the high latitude in spite of the strong radial shear flow in the tachocline.

Fig. 23 shows the evolution of the toroidal field (left column) and the poloidal field lines (right column) in a meridional quadrant for four successive epochs during a half cycle period. In the first snapshot (Figs. 23a and 23e) there is a negative toroidal field in the tachocline from which a new counter-clockwise poloidal flux

system is generated in the surface layer. The poloidal fields begin to diffuse due to the strong surface diffusivity (Fig. 23f). This is in contrast with the previous flux transport models (Dikpati & Charbonneau, 1999; Chatterjee et al., 2004) in which the meridional flow transports poloidal fields to the high latitude on this stage. In our model the meridional flow has weaker effect on the surface poloidal fields because of the relatively strong surface diffusivity. The poloidal fields are not advected to the pole but are radially diffused to the base of the convection zone (Fig. 23h). In Fig. 23a-23d there are weaker toroidal fields at the high-latitude tachocline than those at the low latitude since the toroidal fields in the tachocline are advected equatorward by the meridional flow. This is an advantage of our model to the previous diffusion-dominated regime (Yeates et al., 2008). In our model where the diffusion is strong only near the surface the meridional flow transports the fields more sufficiently to the equator at the base of the convection zone. The importance of the diffusivity profile is discussed in §9.

## 9 Parameter Dependence

### 9.1 Dependence of the Magnetic Field

In this subsection the dependence of the magnetic field on the surface diffusivity  $\eta_{\text{surf}}$  and the speed of the meridional flow  $v_0$  is discussed. We show the results for the surface diffusivity  $\eta_{\text{surf}}$  from  $9 \times 10^{10} \text{ cm}^2 \text{ s}^{-1}$  to  $9 \times 10^{12} \text{ cm}^2 \text{ s}^{-1}$ . Other parameters are unchanged from the reference case (e.g.  $v_0 = 1000 \text{ cm s}^{-1}$ ,  $r_p = 0.62R_{\odot}$ ). With a stronger diffusivity than  $9 \times 10^{12} \text{ cm}^2 \text{ s}^{-1}$ , we do not obtain a periodic solution.

We compare the radial field strength  $|B_r|$  at the pole (colatitude  $0^\circ$ ) with that at  $45^\circ$  both at the surface. Fig. 24 shows  $\max|B_{r(\text{pole})}|/\max|B_{r(\theta=45^\circ)}|$ , the ratio of the

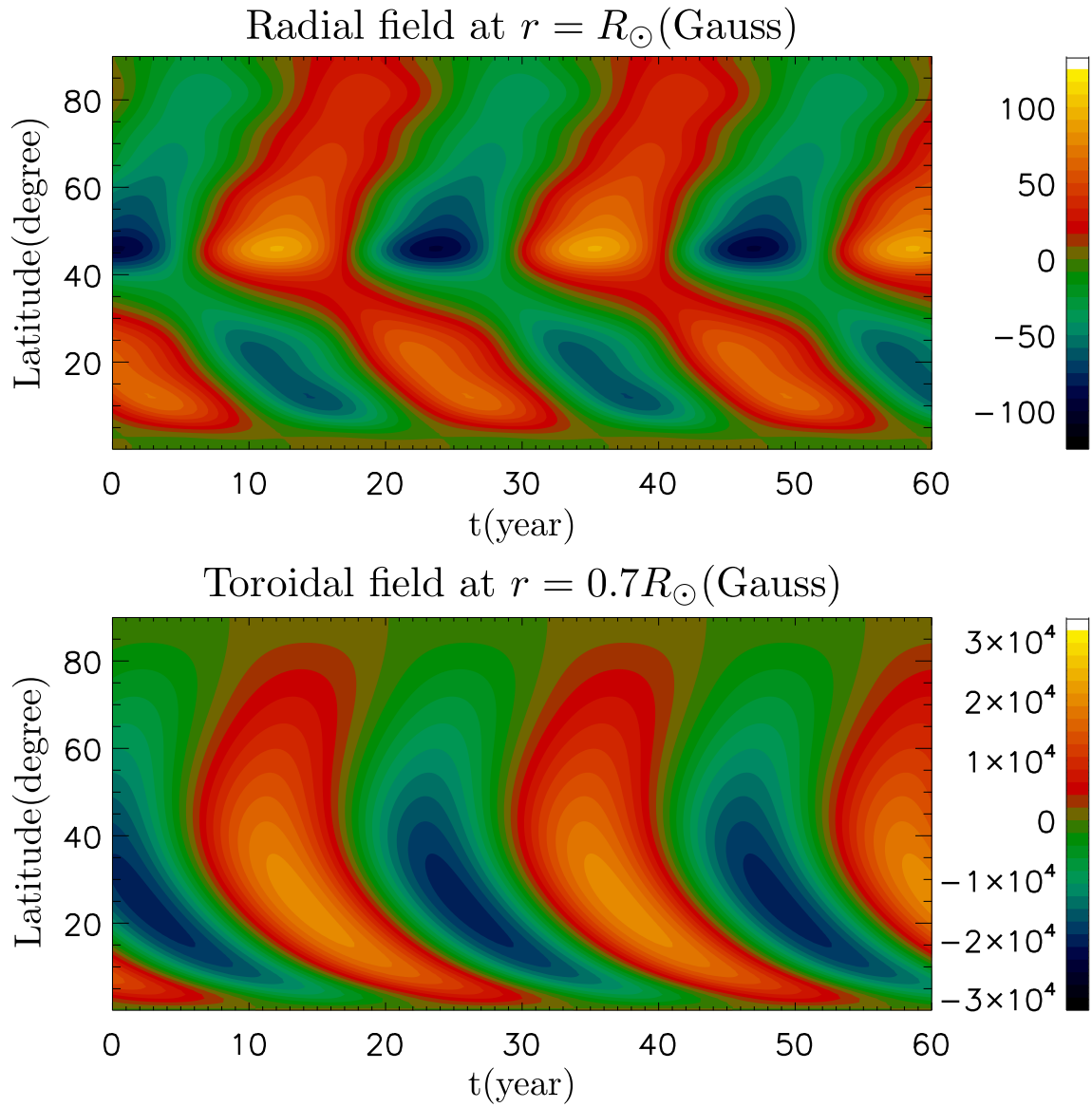


Figure 22: Butterfly diagrams for the reference solution. (Top) Time-latitude plot of the surface radial field  $B_{r(r=R_{\odot})}$ . (Bottom) Time-latitude plot of the toroidal field at the tachocline  $B_{\phi(r=0.7R_{\odot})}$ . Color bars are given for the radial and toroidal field, respectively, in unit of Gauss .

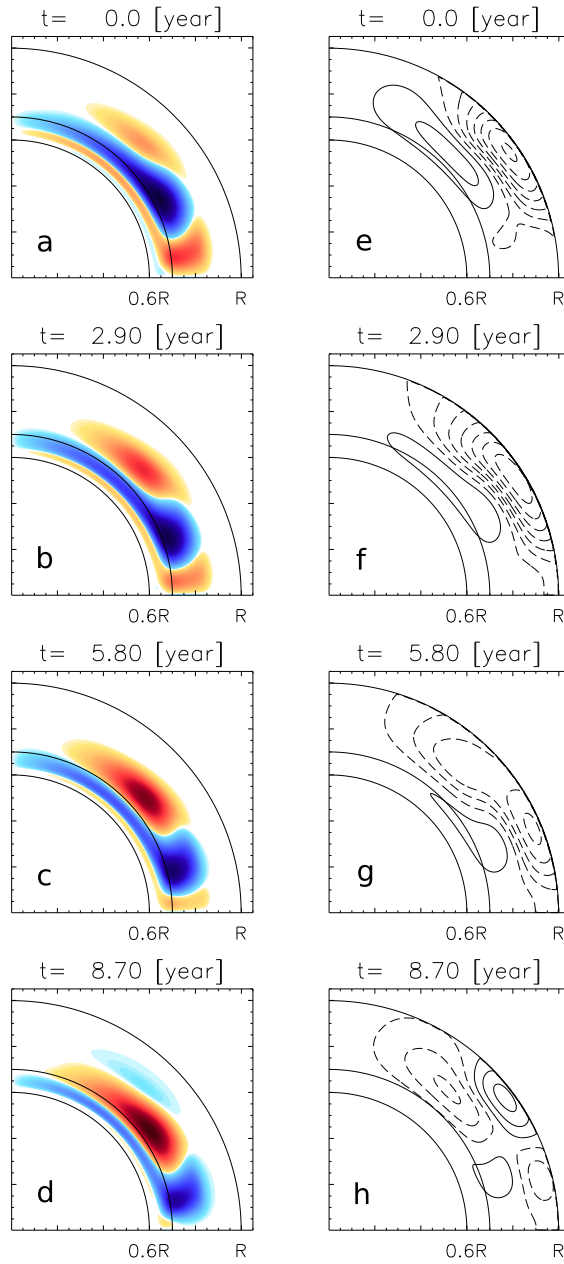


Figure 23: (left) Snapshots of the positive (negative) toroidal field contours in blue (red). (right) The field lines of the clockwise-oriented (counterclockwise-oriented) poloidal field in solid (dashed) lines. Also indicated is the location of the tachocline at  $r_c = 0.7R_\odot$ .

temporal peak values of  $|B_r|$  for each location as a function of the surface diffusivity  $\eta_{\text{surf}}$ . When we use the strong surface diffusivity in  $\eta_{\text{surf}} = 2 \times 10^{12} - 9 \times 10^{12} \text{ cm}^2 \text{ s}^{-1}$ , the ratio  $\max|B_{r(\text{pole})}|/\max|B_{r(\theta=45^\circ)}|$  is under or around unity. On the other hand, when we use a weak surface diffusivity, the ratio suddenly becomes larger, reaching  $\sim 100$  when  $\eta \sim 10^{11} \text{ cm}^2 \text{ s}^{-1}$ . This is explained as follows. When the surface diffusivity is relatively weak, poloidal fields become strong due to the convergence at the high latitude by the meridional flow. On the other hand, when the diffusivity is stronger, the diffusive transport is more effective than that by the meridional flow. The poloidal flux, therefore, radially diffuses down before it converges at the pole.

The condition for preventing poloidal fields from the polar convergence is determined by balance between the diffusion and the advection by the meridional flow at the surface, i.e. the time scale of the surface diffusion is shorter than that of the advection. Namely

$$\frac{L^2}{\eta_{\text{surf}}} < \frac{L}{\tilde{v}}, \quad (3.9.1)$$

where  $L$  is the size of the polar region and  $\tilde{v}$  is the average flow speed near the pole. We specify  $L$  by the length of the arc between the latitudes  $80^\circ$  and  $90^\circ$  on the surface and  $\tilde{v}$  by the average of the  $\theta$ -component of the meridional flow in the same latitudinal range on the surface. (Note that  $L$  would be changed with a different distribution of the meridional flow. A further study is necessary about the dependence on the distribution of the meridional flow that is beyond the scope of this study.) By taking into account the given spatial distribution of the meridional flow, it is shown  $\tilde{v}/v_0 \sim 0.15$ . With this and the given geometry  $L \sim 10^{10} \text{ cm}$ , we obtain the necessary condition for the ratio of the speed of the meridional flow to

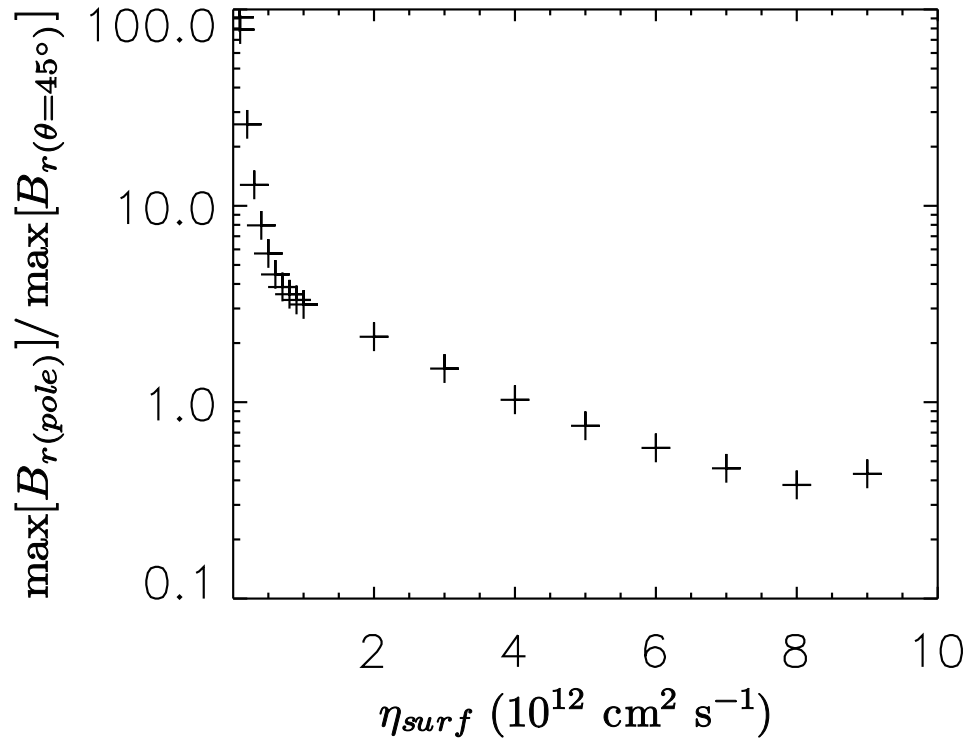


Figure 24: Dependence of the ratio  $\max|B_{r(\text{pole})}|/\max|B_{r(\theta=45^\circ)}|$  on the surface diffusivity  $\eta_{\text{surf}}$ .

the surface diffusivity to be

$$\frac{\eta_{\text{surf}}}{v_0} > 2 \times 10^9 \text{ cm.} \quad (3.9.2)$$

According to this condition, the surface critical diffusivity becomes  $2 \times 10^{12} \text{ cm}^2 \text{ s}^{-1}$  when  $v_0 = 1000 \text{ cm s}^{-1}$ . This is consistent with our results (see Fig. 24). Other diffusion-dominated regimes by Chatterjee et al. (2004) and Yeates et al. (2008) did not satisfy this requirement. Both of them used  $v_0 = 2000 \text{ cm s}^{-1}$  and  $\eta_{\text{surf}} = 2 \times 10^{12} \text{ cm}^2 \text{ s}^{-1}$ . Our simulation results indicate that the strong surface diffusivity is necessary to obtain the proper poloidal fields. We call our diffusion-dominated regime as “strongly diffusion-dominated” hereafter.

The ratio  $\max|B_{\phi(\theta=9^\circ)}|/\max|B_{\phi(\theta=72^\circ)}|$ , i.e. the ratio of the toroidal field  $|B_\phi|$  at the colatitudes  $9^\circ$  (close to the pole) to that at  $72^\circ$  (close to the active latitude) both at the tachocline ( $r = 0.7R_\odot$ ), is shown in Fig. 25. The result resembles that of Fig. 24. By using the strong diffusivity, generation of a strong toroidal field is avoided in the high latitude at the tachocline.

Fig. 26 shows the ratio of  $\max|B_{r(\text{pole})}|/\max|B_{r(\theta=45^\circ)}|$  as a function of  $v_0$  from  $50 \text{ cm s}^{-1}$  to  $3000 \text{ cm s}^{-1}$  with fixing  $\eta_{\text{surf}} = 1 \times 10^{12}$ . Although there is no clear transition, the ratio is large ( $> 1$ ) when the speed of the meridional flow is larger than  $800 \text{ cm s}^{-1}$ . Fig. 27 shows the ratio of the toroidal field strength  $\max|B_{\phi(\theta=9^\circ)}|/\max|B_{\phi(\theta=72^\circ)}|$ . When the value of  $v_0$  is between  $50 \text{ cm s}^{-1}$  and  $2000 \text{ cm s}^{-1}$ , the ratio monotonously increases. This can be understood as in the discussion for the  $\eta_{\text{surf}}$  dependence. With the faster meridional flow than  $2000 \text{ cm s}^{-1}$ , the ratio decreases, because the toroidal fluxes are transported by the flow before they are amplified by the  $\Omega$  effect.

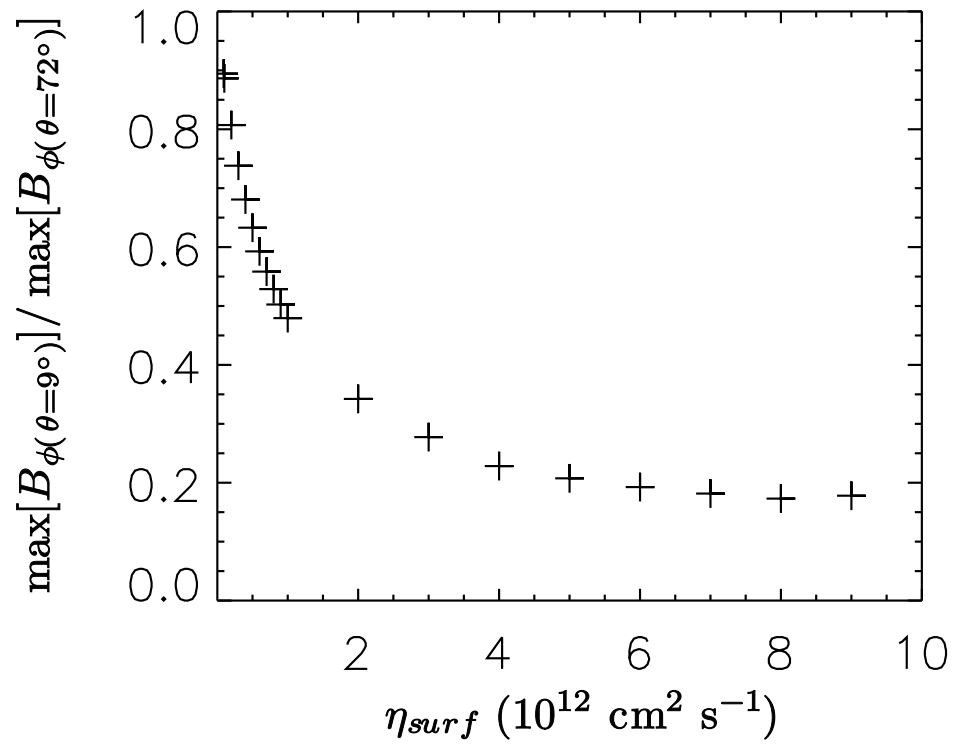


Figure 25: Dependence of the ratio  $\max|B_{\phi(\theta=9^\circ)}|/\max|B_{\phi(\theta=72^\circ)}|$  on the surface diffusivity.

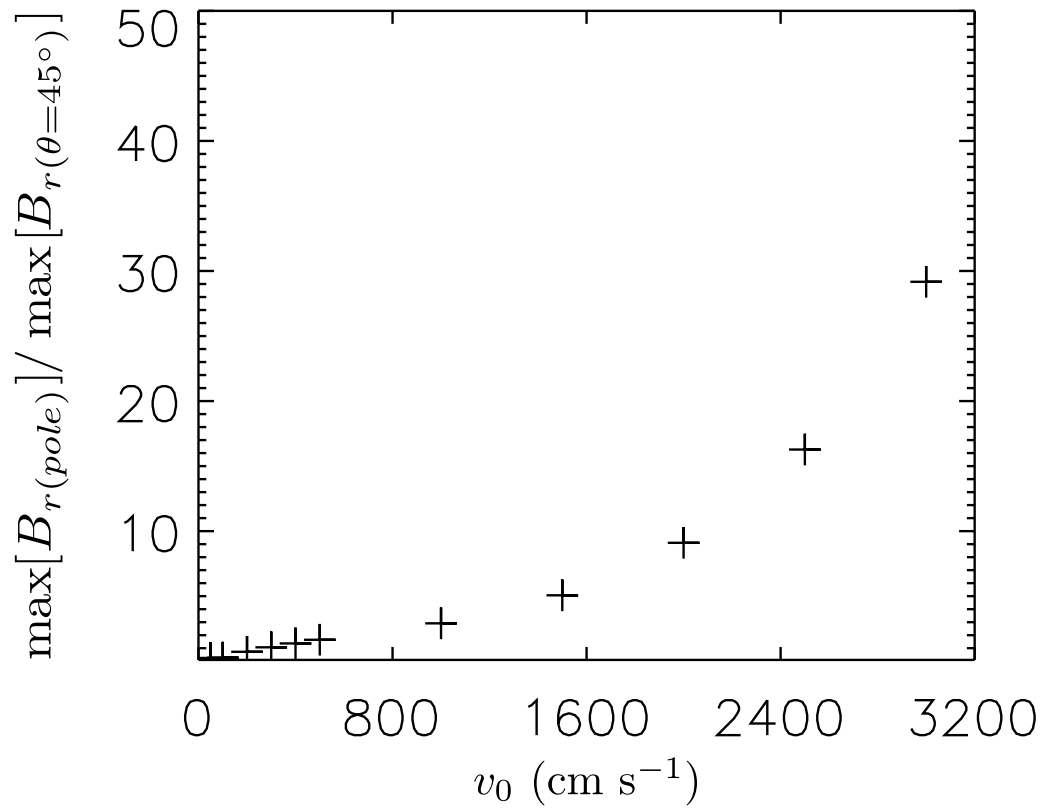


Figure 26: Dependence of the ratio  $\max|B_{r(\text{pole})}|/\max|B_{r(\theta=45^\circ)}|$  on the speed of the meridional flow  $v_0$ .

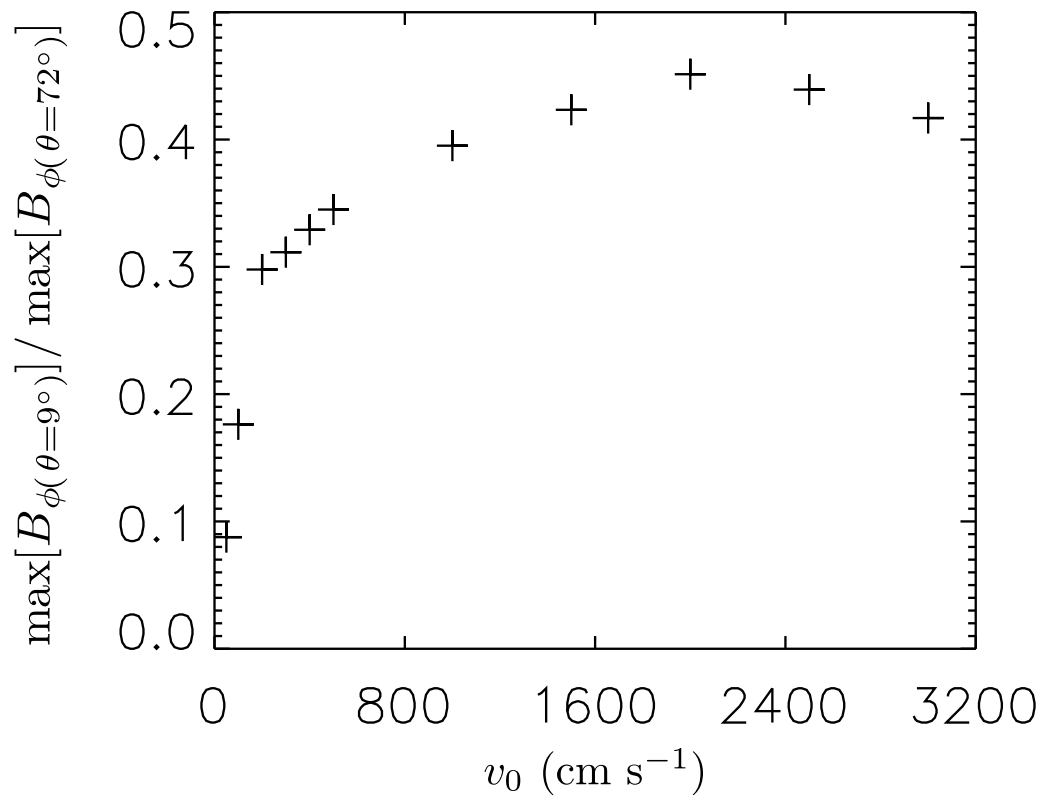


Figure 27: Dependence of the ratio  $\max|B_{\phi(\theta=9^\circ)}|/\max|B_{\phi(\theta=72^\circ)}|$  on the speed of the meridional flow  $v_0$ .

## 9.2 Dependence of cycle period

In this section we investigate the dependence of the cycle period. First we vary the parameter  $v_0$  in the range of  $600 \text{ cm s}^{-1}$  to  $2000 \text{ cm s}^{-1}$  and fix the surface diffusivity  $\eta_{\text{surf}} = 9 \times 10^{12} \text{ cm}^2 \text{ s}^{-1}$ . Using the weak surface diffusivity, Dikpati & Charbonneau (1999) found the dependence of the cycle period on the meridional flow speed as  $P \propto v_0^{-0.89}$ . Yeates et al. (2008) obtained a weaker dependence  $P \propto v_0^{-0.76}$  in their diffusion-dominated regime with the strong diffusivity throughout the convection zone. In our model, the dependence of the cycle period is  $P \propto v_0^{-0.91}$  (Fig. 28) and  $P \propto \eta_{\text{surf}}^{0.06}$  (Fig. 29). Our dependence on  $v_0$  is stronger than the weak diffusion cases of Dikpati & Charbonneau (1999) in which the faster meridional flow converges more magnetic flux at the pole and it takes more time to cancel this field. In the studied range of  $v_0$  and  $\eta_{\text{surf}}$ , the condition of eq. (3.9.1) is satisfied, i.e. in the “strongly diffusion-dominated” regime. In our model, since the duration for cancelling the weak polar flux in the previous cycle is shorter the period directly reflects the transport efficiency by the meridional flow.

## 10 Cases with Shallow Meridional Flow

In this section we discuss the cases with a shallower meridional flow (cf. Nandy & Choudhuri, 2002; Muñoz-Jaramillo et al., 2009). Fig. 30 shows the typical result for the case in which  $r_p = 0.7R_\odot$ ,  $\alpha_0 = 225 \text{ cm s}^{-1}$  and the other parameters are the same as the reference solution in §8. By taking this larger  $\alpha_0$  the amplitudes of the  $\alpha$  effect is set to be relatively strong to complement the weak transport of the poloidal field by the meridional flow to the tachocline due to the shallower penetration. The toroidal field at the high latitude is similar to or less than that the

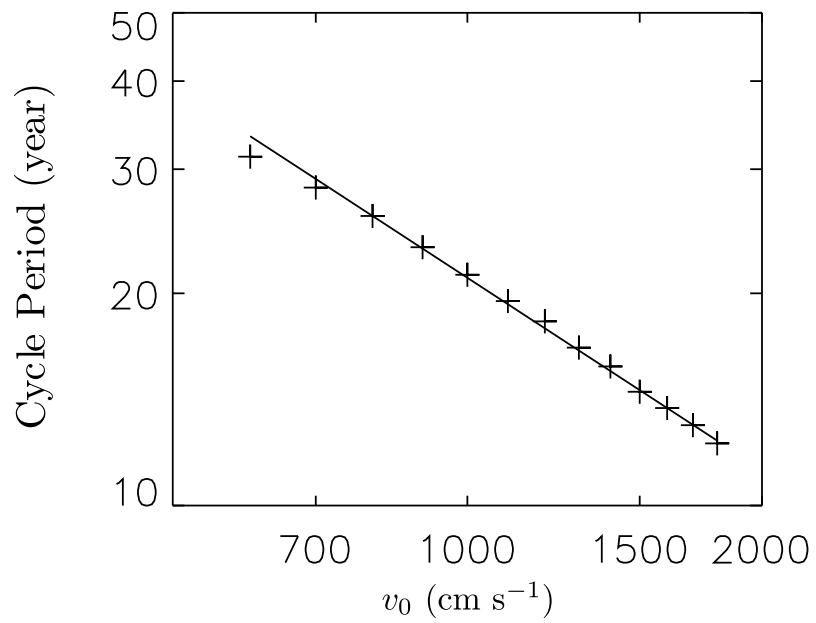


Figure 28: Dependence of the cycle period  $P$  on the speed of the meridional flow  $v_0$  when the bottom of the flow is at  $r_p = 0.62R_\odot$ . The solid line is the least squares line of best fit,  $P \propto v_0^{-0.91}$ .

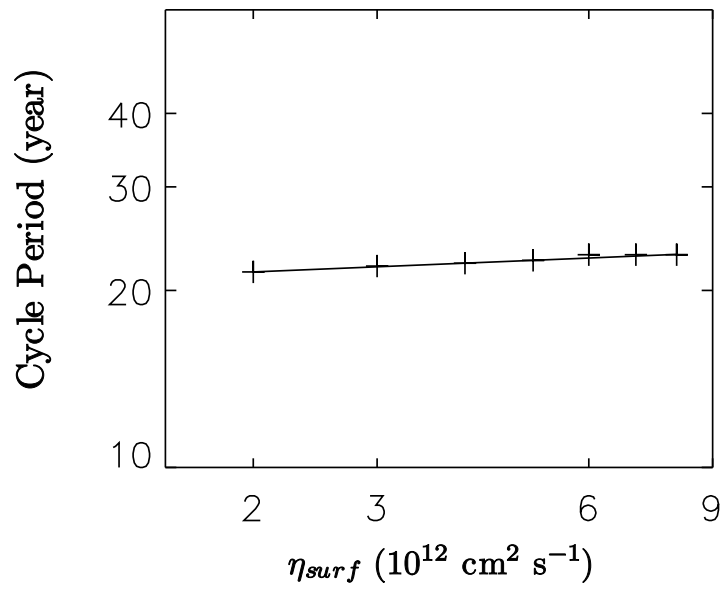


Figure 29: Dependence of the cycle period  $P$  on the surface diffusivity  $\eta_{\text{surf}}$  when the bottom of the meridional flow is at  $r_p = 0.62R_{\odot}$ . The solid line is the least squares line of best fit,  $P \propto \eta_{\text{surf}}^{0.06}$ .

reference case in Fig. 22. This is because the shallower meridional flow transports poloidal flux equatorward more efficiently in the convection zone. It is found that the cycle period becomes longer ( $\sim 38$  year) than the that of reference case ( $\sim 10$  year) (cf. Muñoz-Jaramillo et al., 2009). Since the efficiency of the radial transport through the tachocline is lower, it takes more time to amplify the toroidal field by the  $\Omega$  effect hence yielding a longer cycle period.

Fig. 31 shows the dependence on the meridional flow speed with  $r_p = 0.7R_\odot$ . It is  $P \propto v_0^{-0.21}$  and is weaker than that of the reference case  $P \propto v_0^{-0.91}$ . This is because of the relatively weaker influence of the meridional flow on the flux transport locally in the tachocline not in the convection zone. Fig. 32 shows dependence of the cycle period on the surface diffusivity. The result is  $P \propto \eta_{\text{surf}}^{-0.21}$ . When the surface diffusivity is strong, the diffusive transport is rapid and the cycle period becomes short. Through the results here, we find an importance of the depth of the penetration of the meridional flow across the tachocline.

## 11 Distribution of $\alpha$ effect

The  $\alpha$  effect is quenched at high latitudes in our reference model (eq. 3.7.13, Dikpati et al., 2004). Some other authors used functional forms of the  $\alpha$  effect which is more moderately quenched at high latitudes. In order to study the influence of this difference, we carried out simulations with moderate quenching distribution for the  $\alpha$  effect. When adopted  $\alpha \propto \sin\theta \cos\theta$  same as Dikpati & Charbonneau (1999), we found that the high latitudinal toroidal field in the tachocline does not become strong ( $B_{\phi(\theta=72^\circ)}/B_{\phi(\theta=9^\circ)}=0.56$ ) without any poleward migration and that the strength of polar magnetic field does not become so strong ( $\sim 50$  G).

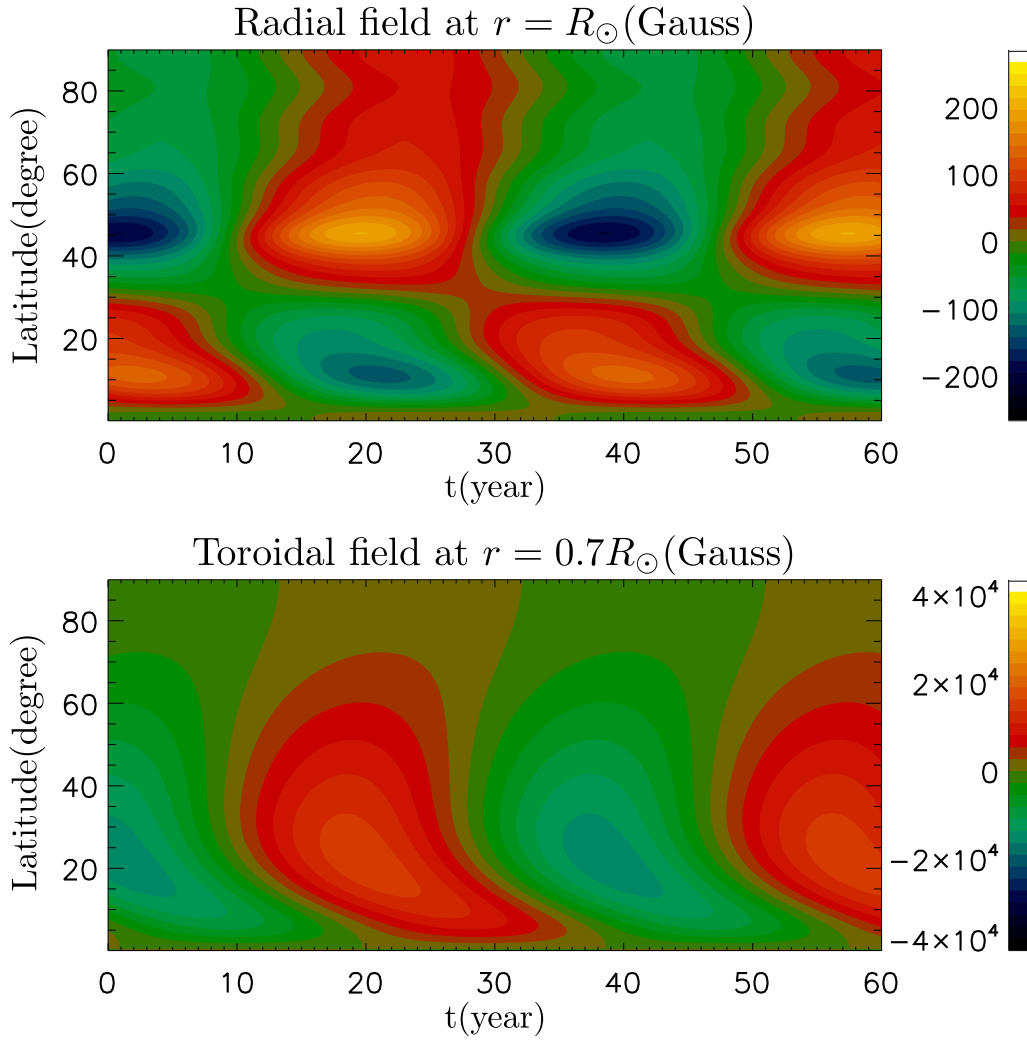


Figure 30: Butterfly diagrams for the case with the shallow meridional flow ( $r_p = 0.7R_{\odot}$ ). Top: time-latitude plot of the surface radial field  $B_r(r = R_{\odot})$ . Bottom: time-latitude plot of the toroidal field at the tachocline  $B_{\phi}(r = 0.7R_{\odot})$ . Color bars are given for the radial and toroidal field, respectively, in the unit of Gauss.

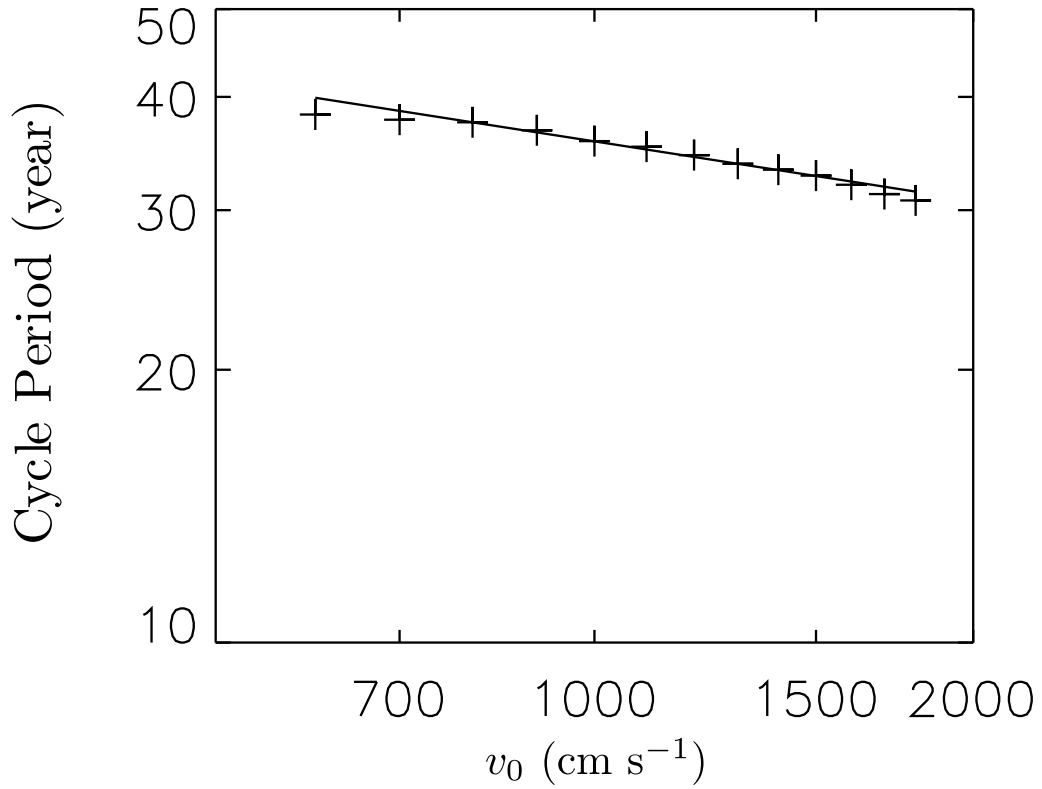


Figure 31: Dependence of the cycle period  $P$  on the speed of the meridional flow  $v_0$  when the bottom of the flow field is at  $r_p = 0.7R_\odot$ . The solid line is the least squares line of best fit,  $P \propto v_0^{-0.21}$ .

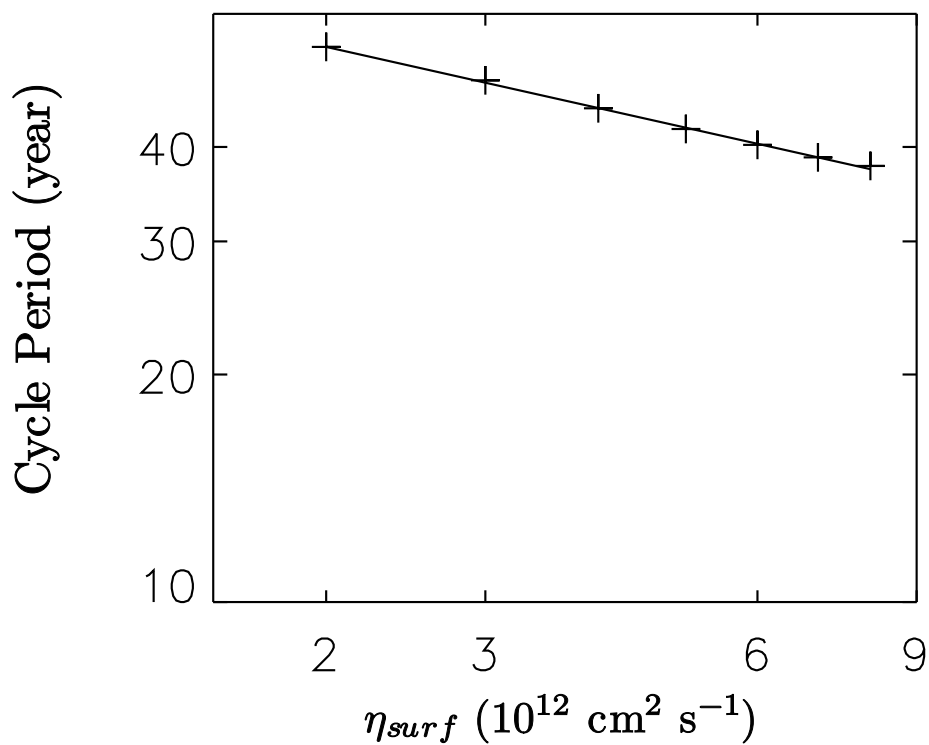


Figure 32: Dependence of the cycle period  $P$  on the surface diffusivity  $\eta_{surf}$  when the bottom of the meridional flow is at  $r_p = 0.7R_{\odot}$ . The solid line is the least squares line of best fit,  $P \propto \eta_{surf}^{-0.21}$ .

When adopted the distribution without any quenching, i.e.  $\alpha \propto \cos \theta$  as Chatterjee et al. (2004), the strong toroidal field appears ( $B_{\phi(\theta=72^\circ)}/B_{\phi(\theta=9^\circ)}=0.97$ ) at high latitudes with the poleward migration. This migration can be avoided, although the field is not weak ( $B_{\phi(\theta=72^\circ)}/B_{\phi(\theta=9^\circ)}=0.78$ ), by introducing a shallow bottom ( $r_p = 0.7R_\odot$ ) because, with the shallow meridional flow, the equatorward transport is effective in the convection zone so that most poloidal flux cannot reach high latitudinal tachocline. Without any quenching (i.e.  $\alpha \propto \cos \theta$ ), the strong polar field ( $\sim 100$  G) is not avoidable, irrespective of the meridional flow depth. It might alternatively suggest a different structure of the meridional flow sinking at latitudes substantially away from the poles.

## 12 Discussion and Conclusion

The flux transport dynamo models has succeeded to reproduce the general cyclic behavior of the solar activity. Previous models, however, could not avoid two problematic features. In this paper we remove these by using the new regime with an additional intense diffusivity profile near the surface.

One of the problematic features is the strong poloidal field ( $\sim 400$  G) at the pole at the surface that does not agree with the observations. This strong field is the consequence of the advection by the poleward meridional flow. It is found that by using a strong surface diffusivity, the poloidal field diffuses radially before it converges at the pole. We derive the condition for avoiding the concentration of the poloidal field (eq. 3.9.2). Previous diffusion-dominated regimes (Chatterjee et al., 2004; Yeates et al., 2008) were not able to avoid the strong polar field simply because the diffusivity was not strong enough. To our knowledge, Muñoz-Jaramillo

et al. (2009) carried out simulations in the parameter range of “strongly diffusion-dominated” regime, but they did not discuss its importance in detail.

The other problematic feature is the strong toroidal field at the high latitude at the tachocline which is generated by the strong radial shear of the angular velocity. In our new model, the poleward advection of the meridional flow is not effective near the surface, while the equatorward advection is effective around the tachocline because of the weaker diffusion. Thus the most magnetic flux is transported radially near the middle latitude and does not concentrate at the high latitude. Some other authors already introduced in §6 (Bonanno et al., 2002; Guerrero & de Gouveia Dal Pino, 2007; Dikpati et al., 2004) avoided the high latitudinal strong toroidal field with the deep penetration of the meridional flow, the thin tachocline or the tachocline  $\alpha$  effect. In this study we could remove the strong toroidal field at the high latitude by introducing stronger surface diffusivity. Dikpati et al. (2004) used the “tachocline  $\alpha$  effect” (see also Dikpati & Gilman, 2001) and obtained the result which agrees with the observations, especially weak polar radial fields ( $\sim 30$  G) and the absence of the strong magnetic field at the tachocline at the high latitude. To obtain their calibrated solution, it needs a careful step-by-step procedure (Dikpati & Gilman, 2007) and we have not succeeded yet.

We use locally strong diffusivity only near the surface and relatively weak one below  $r = 0.8R_{\odot}$ . If we use the strong diffusivity throughout the convection zone (e.g. Yeates et al., 2008), the equatorward drift of the toroidal field is not be obtained because the equatorward transportation by meridional flow is not so effective.

We find that the influence of  $v_0$  is larger in the “strongly diffusion-dominated” regime than the ordinary weak surface diffusivity regime. In the ordinary flux trans-

port dynamo with weak diffusion, the faster the meridional flow concentrates the more radial fields at the pole and it takes the new cycle’s field longer time to cancel it. It does not occur in the “strongly diffusion-dominated” regime.

Our conclusions are summarized as follows: (1) With an intense diffusivity profile only near the surface, the poloidal field is transported down to the tachocline by the diffusion and the toroidal field is transported by the meridional flow in the tachocline. This results in avoiding the concentration of the polar surface field and the amplification of the toroidal field at the high latitude. (2) With the parameters which satisfy the condition  $\eta_{\text{surf}}/v_0 > 2 \times 10^9$  cm and a moderate  $\alpha$  quenching, the distribution of the magnetic field changes especially in the pole i.e. the absence of the strong polar field. (3) With the meridional flow which has a shallower penetration, the influence of  $v_0$  on the cycle period  $P$  is weak ( $P \propto v_0^{-0.21}$ ) compared to the deep penetration case ( $P \propto v_0^{-0.91}$ ). The depth of the meridional flow is an important parameter.

Since we solve the dynamo equations only in a northern half of the meridional plane ( $0 < \theta < \pi/2$ ), we cannot discuss the problem of the parity (Dikpati & Gilman, 2001). Chatterjee et al. (2004) found that the strong surface diffusivity is necessary to obtain a dipole solution. The diffusivity profile may be one of the important element for the parity issue since reconnection of the poloidal and toroidal field plays a important role. With the frequent reconnection of the poloidal field over the equator, the global field tends to be dipole i.e. the asymmetry field about the equator. In contrast, the frequent reconnection of the toroidal field is apt to make the global field symmetry (see also Chatterjee & Choudhuri, 2006; Goel & Choudhuri, 2009). It will be our future work to study the possibility of the dipole

solution by covering the full hemisphere in our new regime.

## Part IV

# Parity of Solar Global Magnetic Field

## 13 Introduction

The solar global field has a distinct parity: the poloidal field is a dipole, i.e., antisymmetric about the equator. The polar fields almost always have the different sign between hemispheres, even though they show the occasional weak north-south asymmetry in phase and amplitude. In addition, Hale's polarity law states that the sunspots between hemispheres are nearly always antisymmetric about the equator (Hale, 1908). It can then be interpreted that the toroidal fields ( $B_\phi$ ) below the surface are antisymmetric about the equator. This interesting feature is, however, not axiomatically explained by the flux transport dynamo model since this model significantly depends on three free parameters, i.e., the  $\alpha$ -effect, the meridional flow, and the turbulent diffusivity.

It has been suggested that the  $\alpha$ -effect around the base of the convection zone leads to the generation of the global dipolar magnetic field. (Dikpati & Gilman, 2001; Bonanno et al., 2002; Chatterjee et al., 2004). The existence of the poloidal fields around the tachocline and the coupling of these fields between hemispheres are significant factors for the generation of the dipole field. A detailed explanation of this process is given in the next paragraph. Chatterjee et al. (2004) also suggested, however, that the dipole field can be obtained with the strong diffusivity in the convection zone without the presence of the  $\alpha$ -effect around the tachocline. Hence the exact necessity of the  $\alpha$ -effect in generating the dipole field is still inconclusive.

The dependence of the parity on these parameters can be explained when we understand the role of the turbulent diffusivity in the solar magnetic parity issue. If the global magnetic field is antisymmetric, i.e. is a dipole like our sun, the  $\phi$  component of the magnetic vector potential in each hemisphere has the same sign (Fig. 33a). When the cyclic phase in one hemisphere slightly differs from the other, the coupling effect by the turbulent diffusivity of the poloidal field distinguishes the phase difference in the vector potential and causes the magnetic field to be a dipole. On the other hand, when the magnetic field is symmetric, i.e., is a quadrupole, this effect does not occur. Therefore the substantial coupling of the poloidal field generates the antisymmetric (a dipole) magnetic field. The sign of the toroidal field in one hemisphere differs from that in the other hemisphere when the global magnetic field is a solar-like dipole. With the same logic posited above, it is obvious that the substantial diffusive coupling of the toroidal field between the hemispheres helps the magnetic field to become symmetric (a quadrupole; Fig 33b). In summary, the parity of the stellar global magnetic field depends on which field, the toroidal or the poloidal, is more coupled by the turbulent diffusivity between the hemispheres. Detailed systematic parameter studies are necessary to understand for the parity issue.

In this study, we investigate the dependence of the solar magnetic parity on the distribution of the turbulent diffusivity and the amplitude of the meridional flow. The obtained constraint on the turbulent diffusivity is important since it is one of the key components of the solar dynamo model, although it is difficult to measure by direct observations.

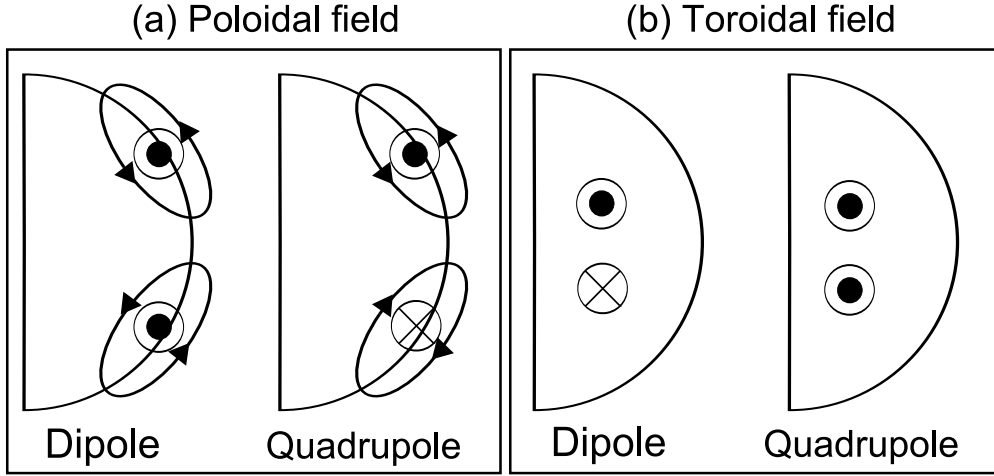


Figure 33: Illustration of the parity issue. Panel (a) shows the poloidal fields (line) for a dipole and a quadrupole field and the corresponding vector potentials. Panel (b) shows the toroidal field for a dipole and a quadrupole.

## 14 Model

The model is almost the same as that of Part III. The differential rotation profile and the poloidal source term ( $\alpha$ -effect) is completely the same as those of Part III. We want to emphasize the some parameters. We use the parameter values  $r_p = 0.62R$  for the meridional flow in eq. (3.7.5) and (3.7.6). Our meridional flow slightly penetrates into the rigidly rotating core, i.e.  $r_p < r_c$  (Hotta & Yokoyama, 2010a). The amplitude of the meridional flow  $v_0$  is took as a parameter. We adopt a diffusivity profile of the form which is expressed in eq. (3.7.11). In this part we specify  $d_1 = d_2 = 0.02R_\odot$ . For convenience, we define the surface depth  $d_s = R_\odot - r_2$  which denotes the thickness of the strong diffusivity layer. We take  $d_s$  and  $\eta_{\text{surf}}$  as free parameters, since they affect the parity of the magnetic field.

We solve equations (3.7.2) and (3.7.3) numerically in all the sphere of the merid-

ional plane in  $0.6R_\odot < r < R_\odot$  and  $0 < \theta < \pi$  with the modified Lax-Wendroff scheme. We use a moderate resolution of around 64 grid points in the radial direction and 128 grid points in the latitudinal direction. At the lower boundary ( $r = 0.6R_\odot$ ), we set both  $B_\phi$  and  $A_\phi$  at zero, indicating that the radiative core is a perfect conductor. At the top boundary ( $r = R_\odot$ ), we set  $B_\phi = 0$  and smoothly match  $A_\phi$  onto an exterior potential field solution (Dikpati & Choudhuri, 1994). At both poles ( $\theta = 0$  and  $\pi$ ), we set  $B_\phi = A_\phi = 0$  for the regularity. The numerical convergence is checked by runs with different grid spacings.

## 15 Results

A new indicator of the magnetic parity is defined in this study. The radial magnetic field at the surface can be decomposed as

$$B_r(R_\odot, \theta) = \sum_{n=0} c_n P_n(\cos \theta), \quad (4.15.1)$$

where  $P_n$  is the Legendre polynomial. Then we define the symmetric parameter as

$$\text{SP} = \frac{\sum_{i=0} |c_{2i}| - \sum_{i=0} |c_{2i+1}|}{\sum_{i=0} |c_i|}. \quad (4.15.2)$$

Each even (odd) order of the Legendre polynomial is symmetric (antisymmetric) about the equator. Therefore,  $\text{SP} = 1$  corresponds to the purely symmetric mode about the equator and  $\text{SP} = -1$  is the antisymmetric mode.

We first show a representative reference solution, computed with the amplitude of the meridional flow  $v_0 = 1000 \text{ cm s}^{-1}$ , the amplitude of the  $\alpha$ -effect  $\alpha_0 = 160 \text{ cm s}^{-1}$ , the amplitude of the turbulent diffusivity near the surface layer  $\eta_{\text{surf}} =$

$2 \times 10^{12} \text{ cm}^2 \text{ s}^{-1}$  and the thickness of the strong diffusivity layer  $d_s = 0.1R_\odot$ . The results are shown in the time-latitude plots in Fig. 34. This simulation is started with a symmetric initial condition. As time passes, the global magnetic field becomes antisymmetric. In such a case, the symmetric parameter develops as shown in Fig. 35. The black (red) line denotes the result with a symmetric (antisymmetric) initial condition. Regardless of the initial condition, the parity of the magnetic field approaches the stationary antisymmetric state where the symmetric parameter becomes  $\sim -1$ . We conclude that the magnetic field with these reference parameters finally becomes a dipole field.

We investigate the asymptotic stationary values of the symmetric parameter for runs in different setups. We carried out runs by choosing a value for the surface diffusivity  $\eta_{\text{surf}}$ , from 8 points in the range  $6 \times 10^{11}$  to  $1 \times 10^{13} \text{ cm}^2 \text{ s}^{-1}$  and the surface depth  $d_s$ , from 5 points in the range  $0.1R_\odot$  to  $0.25R_\odot$ . We specify the amplitude of the  $\alpha$ -effect by

$$\alpha_0 = 160 \text{ cm s}^{-1} \left( \frac{\eta_{\text{surf}}}{2 \times 10^{12} \text{ cm}^2 \text{ s}^{-1}} \right)^2 \left( \frac{d_s}{0.1R_\odot} \right)^2 \quad (4.15.3)$$

The background reason for this setup is to fix the value of the surface integrated dynamo number,

$$N_D = \frac{\alpha_0 k_x R_\odot d_\alpha}{\eta_{\text{surf}}^2 d_s^2 k^4} \frac{d}{dr} (r \Omega \sin \theta), \quad (4.15.4)$$

where  $k_x$  and  $k$  denote the wavenumber of the magnetic field and  $d_\alpha$  denotes the thickness of the layer where the  $\alpha$ -effect is effective, and where  $k_x$ ,  $k$  and  $d_\alpha$  are assumed to be unchanged from case to case. This dynamo number is kept unchanged since it determines the oscillatory nature of the dynamo. The reason for this idea is because the strong  $\alpha$ -effect is necessary to endure the diffusivity in the large area.

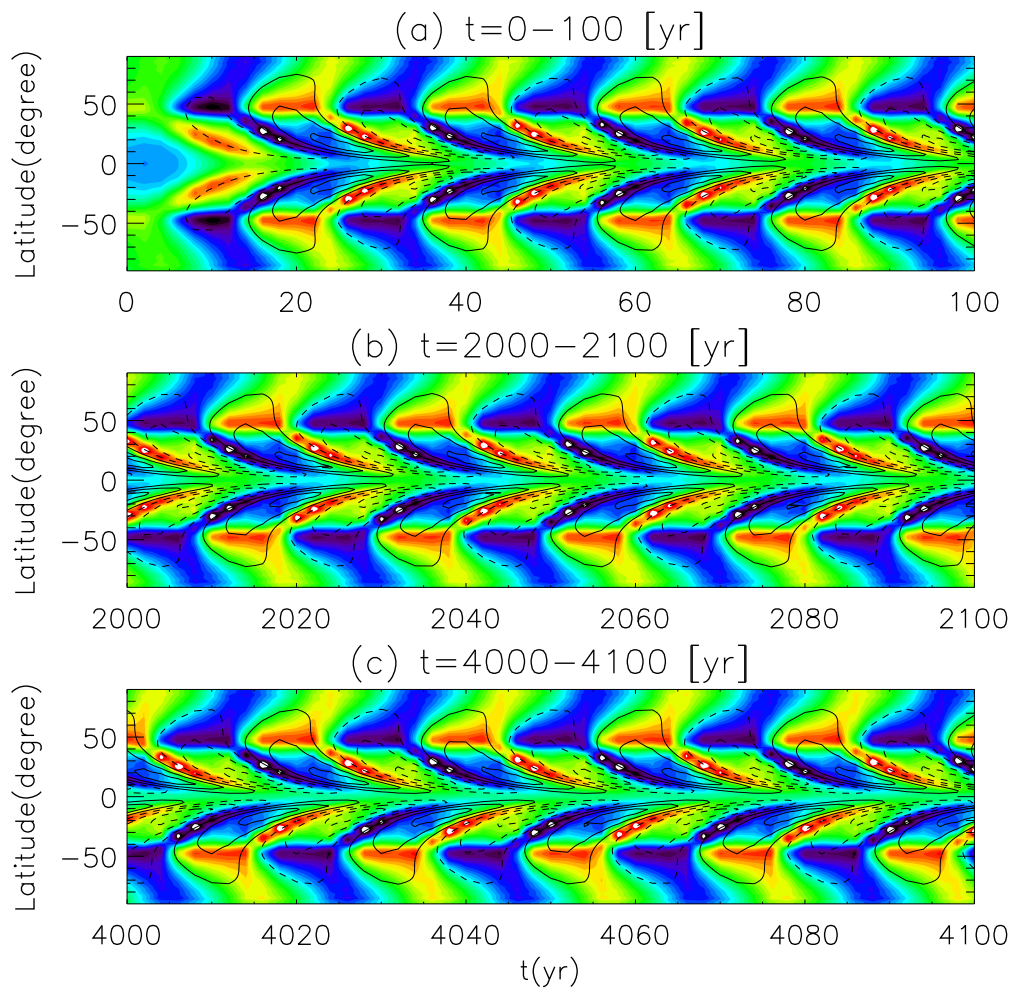


Figure 34: Butterfly diagram for the reference solution. Time-latitude plot of  $B_\phi|_{r=0.7R_\odot}$  by contour is superposed on the color map of the surface radial fields.

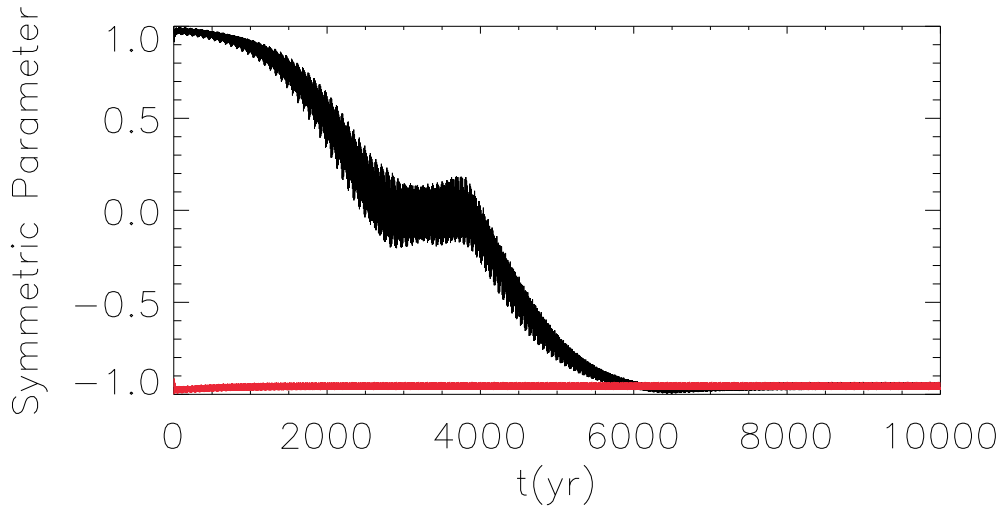


Figure 35: Time-development of the symmetric parameters. The black (red) line corresponds to the results of the symmetric (antisymmetric) initial condition. Regardless of the initial condition the symmetric parameter finally becomes  $\sim -1$  (antisymmetric solution).

We also vary the amplitude of the meridional flow:  $v_0 = 1000 \text{ cm s}^{-1}$  (slow meridional flow case) and  $2000 \text{ cm s}^{-1}$  (fast meridional flow case). For every parameter set, we conducted runs with both symmetric and antisymmetric initial conditions to ensure that the asymptotic value of the symmetric parameter does not depend on the initial parity.  $8(\text{diffusivity}) \times 4(\text{surface depth}) \times 2(\text{meridional flow}) \times 2(\text{initial parity}) = 128$  simulation runs carried out. All simulations are calculated for more than 10000 years.

There are two types of solutions when the value of the SP is around zero and we categorize them as “mixed-parity” cases. One type is similar to the reference case (Fig. 36a). The value of the SP finally converges. The other type is interesting in that the value of the symmetric parameter does not converge and continues to oscillate between the quadrupole and the dipole solutions (Fig. 36b). Since the

averaged value in the calculation duration is close to zero, we adopted it for that the SP in such cases.

The results of this parameter space study are shown in Fig. 37. The dynamo cycle period is also shown by the contour lines. The period is shorter when the surface depth is thicker since the transport of the magnetic flux by the diffusivity is more effective. Panel (a) shows the result of the slow meridional flow case ( $v_0 = 1000 \text{ cm s}^{-1}$ ). Two points can be ascertained from this figure. One is that regardless of the surface depth, the strong diffusivity ( $> 3 \times 10^{12} \text{ cm}^2 \text{ s}^{-1}$ ) can make the magnetic field to become a dipole ( $\text{SP} \sim -1$ ). The other is that with the thinner surface depth, no strong diffusivity ( $> 1 \times 10^{12} \text{ cm}^2 \text{ s}^{-1}$ ) is needed to generate the dipole field. This means that the magnetic field is more likely to be a dipole with the thinner surface depth. Fig. 4b shows the result of the fast meridional flow case ( $v_0 = 2000 \text{ cm s}^{-1}$ ). It is obvious that the parameter area for the symmetric solutions, i.e.  $\text{SP} > 0$ , increases. This indicates that the fast meridional flow causes the magnetic field to be symmetric.

## 16 Discussion and Conclusion

We investigated the dependence of the global magnetic parity on the distribution of the diffusivity (the amplitude and the surface depth) and the amplitude of the meridional flow. Three results were obtained. First, the model shows that the stronger diffusivity near the surface acts to make the magnetic field a dipole. The diffusivity near the surface enhances mainly the coupling of the poloidal field near the surface between the hemispheres, leading to the generation of dipolar magnetic field. The second result is that the thinner layer of the strong surface diffusivity

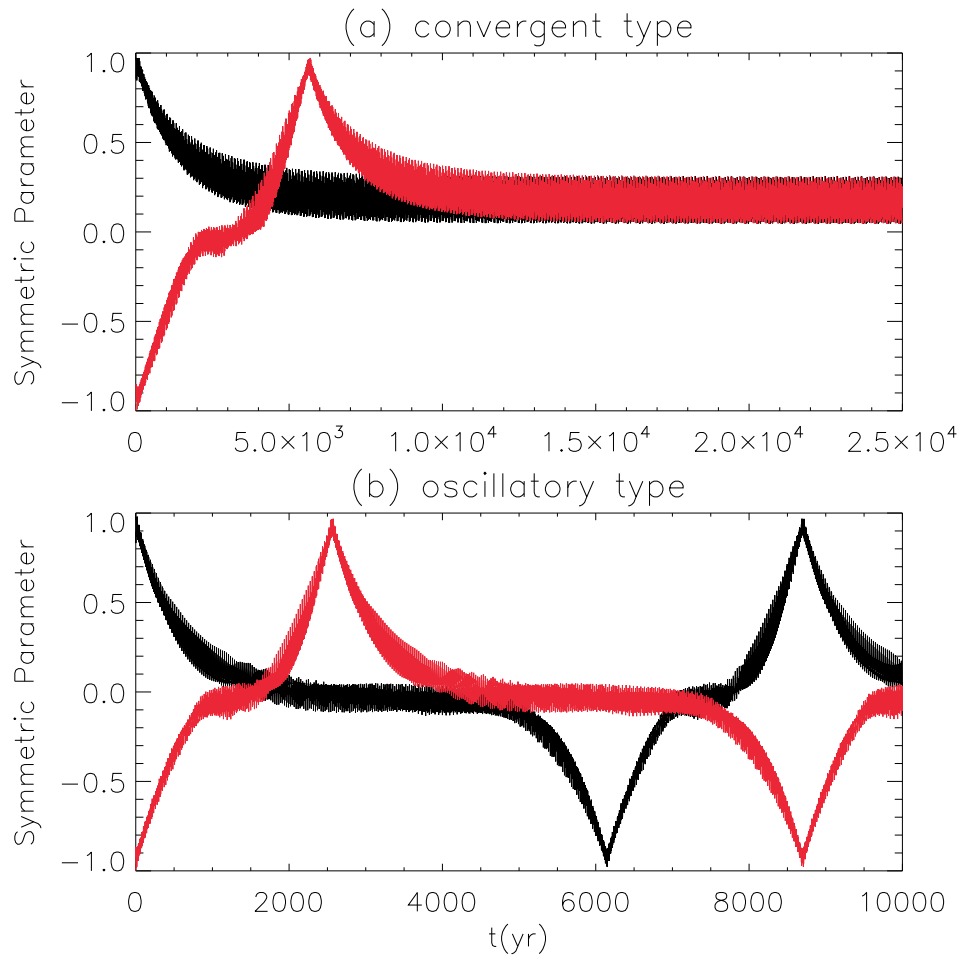


Figure 36: Two types in "zero" symmetric parameter cases. The time-development of the symmetric parameter for each type is shown. The format is the same as in Fig. 35. Panel (a) shows the convergent type in which the value of the symmetric parameter finally converges to zero. Panel (b) shows the oscillation type in which the symmetric parameter continues to oscillate between the quadrupole ( $SP \sim -1$ ) and the dipole ( $SP \sim 1$ ) solutions.

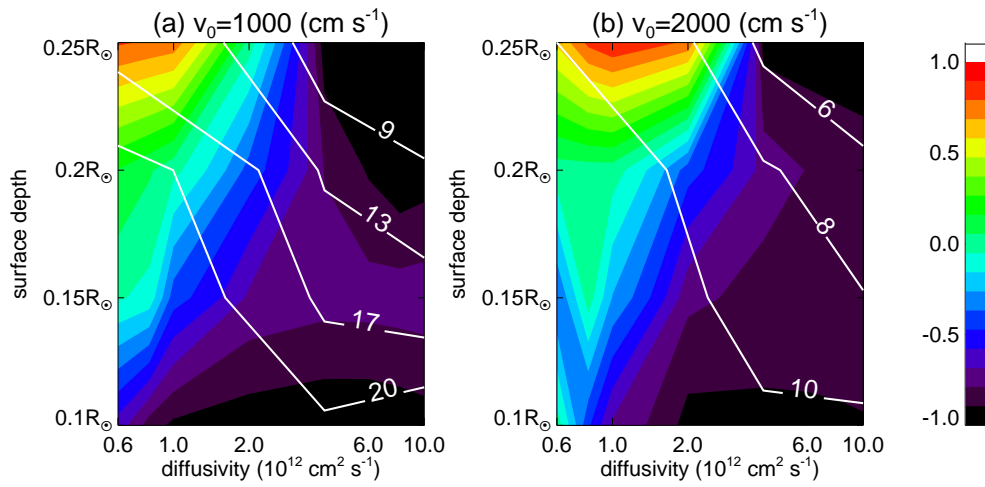


Figure 37: Symmetric parameter SP as a function of the diffusivity  $\eta_{\text{surf}}$  and the surface depth  $d_s$ . The superposed lines indicate the contours of the dynamo cycle period over periods of years. Panel (a) shows the results for the slow meridional flow case ( $v_0 = 1000 \text{ cm s}^{-1}$ ). Panel (b) shows the result for the fast meridional flow case ( $v_0 = 2000 \text{ cm s}^{-1}$ ).

also works to cause the magnetic field to become dipolar. The thinner surface depth suppresses the coupling of the toroidal field between the hemispheres since most of the toroidal field exists around the tachocline. The third result is that the fast meridional flow causes the magnetic field to become a quadrupole. The fast meridional flow prevents the poloidal field from coupling near the surface of the equator because the flow transports the poloidal field poleward. In addition, the flow transports the toroidal field around the tachocline equatorward, thus causing the coupling of the toroidal field. These three results quantitatively constrain the distribution and the amplitude of turbulent diffusivity, which cannot be determined by observation and is an important factor for the dynamo problem.

In this study, we did not investigate the dependence of the parity on the  $\alpha$ -effect in the convection zone, which may be a strong factor in causing the magnetic field to become a dipole. The poloidal field generated by this effect around the tachocline is transported equatorward by the meridional flow, and this process enhances the coupling of the poloidal field between the hemispheres (Dikpati & Gilman, 2001; Bonanno et al., 2002; Chatterjee et al., 2004). It is possible that the criterion for a dipole field we obtain in this study may be modified with this type of  $\alpha$ -effect. We will discuss the possibility of the existence and the influence of the  $\alpha$ -effect in a forthcoming paper. Another interesting issue to be addressed is the possibility that the variation of the velocity field in the solar cycle affects the parity. In the calculations for the earth dynamo there is the significant difference between the kinematic and the MHD cases in the parity issue (Nishikawa & Kusano, 2008). Thus, in the future we will investigate the parity issue with the Lorentz feedback (Rempel, 2006).

## Part V

# Differential Rotation in Rapidly Rotating Stars

## 17 Introduction

Our sun has an eleven-year magnetic activity cycle, which is thought to be sustained by the dynamo motion of internal ionized plasma, i.e., a transformation of kinetic energy to magnetic energy (Parker, 1955). Our understanding of the solar dynamo has significantly improved during the past fifty years, and some kinematic studies can now reproduce solar magnetic features such as equatorward migration of sunspots and poleward migration of the magnetic field (Choudhuri et al., 1995; Dikpati & Charbonneau, 1999; Küker et al., 2001; Charbonneau, 2005; Hotta & Yokoyama, 2010a,b). The most important mechanism of the solar dynamo is the  $\Omega$  effect, the bending of pre-existing poloidal magnetic fields by differential rotation and the generation of toroidal magnetic fields. Thus, the distribution of the differential rotation in the convection zone is a significant factor for the solar dynamo. Using helioseismology, it has recently been shown that the solar internal differential rotation is in a non-Taylor-Proudman state (see review by Thompson et al., 2003), meaning the iso-rotation surfaces are *not* parallel to the axis.

Based on solar observations, it is known that Ca H-K fluxes can be a signature of stellar chromospheric activity, and such chromospheric signatures are in correlation with magnetic activity. Wilson (1968, 1978) and Baliunas et al. (1995) discuss a class of stars that shows a periodic variation in Ca H-K fluxes, which suggests that they have a magnetic cycle similar to our sun. It is natural to conjecture that

such magnetic activity is maintained by dynamo action. Various studies have been conducted to investigate the relationship between stellar angular velocity  $\Omega_0$  and its latitudinal difference  $\Delta\Omega$  i.e.,  $\Delta\Omega \propto \Omega_0^n$ , where the suggested range of  $n$  is  $0 < n < 1$  (Donahue et al., 1996; Reiners & Schmitt, 2003; Barnes et al., 2005). This means that the angular velocity difference  $\Delta\Omega$  increases and the relative difference  $\Delta\Omega/\Omega_0$  decreases with increases in the stellar rotation rate  $\Omega_0$ .

In this paper, we investigate differential rotation in rapidly rotating stars using a mean field framework. Our study is based on the work of Rempel (2005b), in which he suggests the importance of the role of the subadiabatic layer below the convection zone in order to maintain a non-Taylor-Proudman state in the Sun. The aim of this paper is to use a mean field model to analyze firstly the dependence of the morphology of differential rotation on stellar angular velocity, and secondly the physical process which determines the observable angular velocity difference  $\Delta\Omega$ . According to our knowledge, this is the first work which systematically discusses the application of Rempel's (2005b) solar model to stars.

Numerical studies on stellar differential rotation exist (Brown et al., 2008; Miesch & Toomre, 2009), and although they resolve stellar thermal driven convection and can calculate a self-consistent turbulent angular momentum transport, the reproduction of an adequate entropy gradient and the solar differential rotation have not yet been achieved. In our present study we succeed in obtaining the latitudinal entropy gradient which is necessary for reproducing the solar differential rotation (see §19 in detail).

## 18 Model

Using numerical settings similar to those of Rempel's (2005b), we solve the axisymmetric hydrodynamic equations in spherical geometry  $(r, \theta)$ , where  $r$  is the radius, and  $\theta$  is the colatitude. The basic assumptions are as follows.

1. A mean field approximation is adopted. All processes on the convective scale are parameterized. Thus, the coefficients for turbulent viscosity, turbulent heat conductivity, and turbulent angular momentum transport are explicitly given in the equations.
2. The perturbations of the density and pressure associated with differential rotation are small, i.e.,  $\rho_1 \ll \rho_0$  and  $p_1 \ll p_0$ . Here  $\rho_0$  and  $p_0$  denote the reference state density and pressure respectively, whereas  $\rho_1$  and  $p_1$  are the perturbations. We neglect the second-order terms of these quantities. Note that the perturbation of angular velocity ( $\Omega_1$ ) and meridional flow ( $v_r, v_\theta$ ) are not small.
3. Since the reference state is assumed to be in an energy flux balance, the entropy equation includes only perturbations.

### 18.1 Equations

We do not use the anelastic approximation here. The equations in an inertial frame can be expressed as

$$\frac{\partial \rho_1}{\partial t} = -\frac{1}{r^2} \frac{\partial}{\partial r} (r^2 v_r \rho_0) - \frac{1}{r \sin \theta} \frac{\partial}{\partial \theta} (\sin \theta v_\theta \rho_0), \quad (5.18.1)$$

$$\begin{aligned}\frac{\partial v_r}{\partial t} = & -v_r \frac{\partial v_r}{\partial r} - \frac{v_\theta}{r} \frac{\partial v_r}{\partial \theta} + \frac{v_\theta^2}{r} - \frac{1}{\rho_0} \left[ \rho_1 g + \frac{\partial p_1}{\partial r} \right] \\ & + (2\Omega_0\Omega_1 + \Omega_1^2)r \sin^2 \theta + \frac{F_r}{\rho_0},\end{aligned}\quad (5.18.2)$$

$$\begin{aligned}\frac{\partial v_\theta}{\partial t} = & -v_r \frac{\partial v_\theta}{\partial r} - \frac{v_\theta}{r} \frac{\partial v_\theta}{\partial \theta} - \frac{v_r v_\theta}{r} - \frac{1}{\rho_0} \frac{1}{r} \frac{\partial p_1}{\partial \theta} \\ & + (2\Omega_0\Omega_1 + \Omega_1^2)r \sin \theta \cos \theta + \frac{F_\theta}{\rho_0},\end{aligned}\quad (5.18.3)$$

$$\frac{\partial \Omega_1}{\partial t} = -\frac{v_r}{r^2} \frac{\partial}{\partial r} [r^2(\Omega_0 + \Omega_1)] - \frac{v_\theta}{r \sin^2 \theta} \frac{\partial}{\partial \theta} [\sin^2 \theta (\Omega_0 + \Omega_1)] + \frac{F_\phi}{\rho_0 r \sin \theta}, \quad (5.18.4)$$

$$\frac{\partial s_1}{\partial t} = -v_r \frac{\partial s_1}{\partial r} - \frac{v_\theta}{r} \frac{\partial s_1}{\partial \theta} + v_r \frac{\gamma \delta}{H_p} + \frac{\gamma - 1}{p_0} Q + \frac{1}{\rho_0 T_0} \text{div}(\kappa_t \rho_0 T_0 \text{grad} s_1), \quad (5.18.5)$$

where  $\Omega_0$  is a constant value that represents the angular velocity of the rigidly rotating radiative zone. We set it as a parameter in Table 1.  $\gamma$  is the ratio of specific heats, with the value for an ideal gas being  $\gamma = 5/3$ .  $\kappa_t$  is the coefficient of turbulent thermal conductivity.  $\delta = \nabla - \nabla_{\text{ad}}$  represents superadiabaticity, where  $\nabla = d(\ln T)/d(\ln p)$  (see §18.2).  $g$  denotes gravitational acceleration. Following from this, the perturbation of pressure  $p_1$  and pressure scale height  $H_p$  are expressed as

$$p_1 = p_0 \left( \gamma \frac{\rho_1}{\rho_0} + s_1 \right), \quad (5.18.6)$$

$$H_p = \frac{p_0}{\rho_0 g}. \quad (5.18.7)$$

$s_1$  is dimensionless entropy normalized by the specific heat capacity at constant volume  $c_v$ . Turbulent viscous force  $\mathbf{F}$  follows from

$$F_r = \frac{1}{r^2} \frac{\partial}{\partial r} (r^2 R_{rr}) + \frac{1}{r \sin \theta} \frac{\partial}{\partial \theta} (\sin \theta R_{\theta r}) - \frac{R_{\theta\theta} + R_{\phi\phi}}{r}, \quad (5.18.8)$$

$$F_\theta = \frac{1}{r^2} \frac{\partial}{\partial r} (r^2 R_{r\theta}) + \frac{1}{r \sin \theta} \frac{\partial}{\partial \theta} (\sin \theta R_{\theta\theta}) + \frac{R_{r\theta} - R_{\phi\phi} \cot \theta}{r}, \quad (5.18.9)$$

$$F_\phi = \frac{1}{r^2} \frac{\partial}{\partial r} (r^2 R_{r\phi}) + \frac{1}{r \sin \theta} \frac{\partial}{\partial \theta} (\sin \theta R_{\theta\phi}) + \frac{R_{r\phi} + R_{\theta\phi} \cot \theta}{r}, \quad (5.18.10)$$

with the Reynolds stress tensor

$$R_{ik} = \rho_0 \left[ \nu_{\text{tv}} \left( E_{ik} - \frac{2}{3} \delta_{ik} \text{div} \mathbf{v} \right) + \nu_{\text{tl}} \Lambda_{ik} \right]. \quad (5.18.11)$$

Here  $\nu_{\text{tv}}$  is the coefficient of turbulent viscosity and  $\nu_{\text{tl}}$  is the coefficient of the  $\Lambda$  effect (Kitchatinov & Rüdiger, 1995), a non-diffusive angular momentum transport caused by turbulence.  $\nu_{\text{tv}}$  and  $\nu_{\text{tl}}$  are expected to have the same value, since both effects are caused by turbulence, i.e., thermal driven convection. We discuss this in more detail in §18.3.  $E_{ik}$  denotes the deformation tensor, which is given in spherical coordinates by

$$E_{rr} = 2 \frac{\partial v_r}{\partial r}, \quad (5.18.12)$$

$$E_{\theta\theta} = 2 \frac{1}{r} \frac{\partial v_\theta}{\partial \theta} + 2 \frac{v_r}{r}, \quad (5.18.13)$$

$$E_{\phi\phi} = \frac{2}{r} (v_r + v_\theta \cot \theta), \quad (5.18.14)$$

$$E_{r\theta} = E_{\theta r} = r \frac{\partial}{\partial r} \left( \frac{v_\theta}{r} \right) + \frac{1}{r} \frac{\partial v_r}{\partial \theta}, \quad (5.18.15)$$

$$E_{r\phi} = E_{\phi r} = r \sin \theta \frac{\partial \Omega_1}{\partial r}, \quad (5.18.16)$$

$$E_{\theta\phi} = E_{\phi\theta} = \sin \theta \frac{\partial \Omega_1}{\partial \theta}. \quad (5.18.17)$$

An expression for the  $\Lambda$  effect ( $\Lambda_{ik}$ ) is given later. The amount of energy that is converted by the Reynolds stress from kinematic energy to internal energy is given by

$$Q = \sum_{i,k} \frac{1}{2} E_{ik} R_{ik}. \quad (5.18.18)$$

## 18.2 Background Stratification

We use an adiabatic hydrostatic stratification for the spherically symmetric reference state of  $\rho_0$ ,  $p_0$  and  $T_0$ . Gravitational acceleration is assumed to have  $\sim r^{-2}$  dependence, since the radiative zone ( $r < 0.65R_\odot$ ) has most of the solar mass. This is expressed as,

$$\rho_0(r) = \rho_{bc} \left[ 1 + \frac{\gamma - 1}{\gamma} \frac{r_{bc}}{H_{bc}} \left( \frac{r_{bc}}{r} - 1 \right) \right]^{1/(\gamma-1)}, \quad (5.18.19)$$

$$p_0(r) = p_{bc} \left[ 1 + \frac{\gamma - 1}{\gamma} \frac{r_{bc}}{H_{bc}} \left( \frac{r_{bc}}{r} - 1 \right) \right]^{\gamma/(\gamma-1)}, \quad (5.18.20)$$

$$T_0(r) = T_{bc} \left[ 1 + \frac{\gamma - 1}{\gamma} \frac{r_{bc}}{H_{bc}} \left( \frac{r_{bc}}{r} - 1 \right) \right], \quad (5.18.21)$$

$$g(r) = g_{bc} \left( \frac{r}{r_{bc}} \right)^{-2}, \quad (5.18.22)$$

where  $\rho_{bc}$ ,  $p_{bc}$ ,  $T_{bc}$ ,  $H_{bc} = p_{bc}/(\rho_{bc}g_{bc})$  and  $g_{bc}$  denote the values at the base of the convection zone  $r = r_{bc}$  of density, pressure, temperature, pressure scale height and gravitational acceleration, respectively. In this study we use  $r_{bc} = 0.71R_\odot$ , with  $R_\odot$  representing the solar radius ( $R_\odot = 7 \times 10^{10}$  cm). We adopt solar values  $\rho_{bc} = 0.2$  g cm $^{-3}$ ,  $p_{bc} = 6 \times 10^{13}$  dyn cm $^{-2}$ ,  $T_{bc} = mp_{bc}/(k_B\rho_{bc}) \sim 1.82 \times 10^6$  K and  $g_{bc} = 5.2 \times 10^4$  cm s $^{-2}$ , where  $k_B$  is the Boltzmann constant, and  $m$  is the mean particle mass. Fig. 38 shows the profiles of background density, pressure and temperature, and gravitational acceleration.

Although the real sun's stratification is not adiabatic in the convection zone, our reference state is valid, since the absolute value of superadiabaticity is small. In order to include the deviation from adiabatic stratification, we assume superadiabaticity  $\delta$  has the following profile:

$$\delta = \frac{\delta_{os}}{2} \left[ 1 - \tanh \left( \frac{r - r_{tran}}{d_{tran}} \right) \right]. \quad (5.18.23)$$

Here  $\delta_{\text{os}}$  denotes the value of superadiabaticity in the overshoot region.  $r_{\text{tran}}$  and  $d_{\text{tran}}$  denote the position and the steepness of the transition toward the subadiabatically stratified overshoot region, respectively. We specify  $\delta_{\text{os}} = -1.5 \times 10^{-5}$ ,  $r_{\text{tran}} = 0.725R_{\odot}$  and  $d_{\text{tran}} = 0.0125R_{\odot}$  in our simulations. In the convection zone ( $r > 0.725R_{\odot}$ ), superadiabaticity is zero in our model, which is justified because the most important factor for solar and stellar differential rotation is the subadiabatically stratified region in which the latitudinal entropy gradient is generated (see also Rempel, 2005b). The entropy gradient can be expressed as

$$\frac{ds_0}{dr} = -\frac{\gamma\delta}{H_p}. \quad (5.18.24)$$

The third term of eq. (42),  $v_r\gamma\delta/H_p$ , includes the effect of deviations from adiabatic stratification. The term indicates that an upflow (downflow) can make negative (positive) entropy perturbations in the subadiabatically stratified layers ( $\delta < 0$ ).

### 18.3 Diffusivity Profile

We assume the coefficients of turbulent viscosity and thermal conductivity to be constant within the convection zone, and these smoothly connect with the values of the overshoot region. We assume that the diffusivities only depend on the radial coordinate:

$$\nu_{\text{tv}} = \nu_{\text{os}} + \frac{\nu_{0v}}{2} \left[ 1 + \tanh \left( \frac{r - r_{\text{tran}} + \Delta}{d_{\kappa\nu}} \right) \right] f_c(r), \quad (5.18.25)$$

$$\nu_{\text{tl}} = \frac{\nu_{0l}}{2} \left[ 1 + \tanh \left( \frac{r - r_{\text{tran}} + \Delta}{d_{\kappa\nu}} \right) \right] f_c(r), \quad (5.18.26)$$

$$\kappa_{\text{t}} = \kappa_{\text{os}} + \frac{\kappa_0}{2} \left[ 1 + \tanh \left( \frac{r - r_{\text{tran}} + \Delta}{d_{\kappa\nu}} \right) \right] f_c(r), \quad (5.18.27)$$

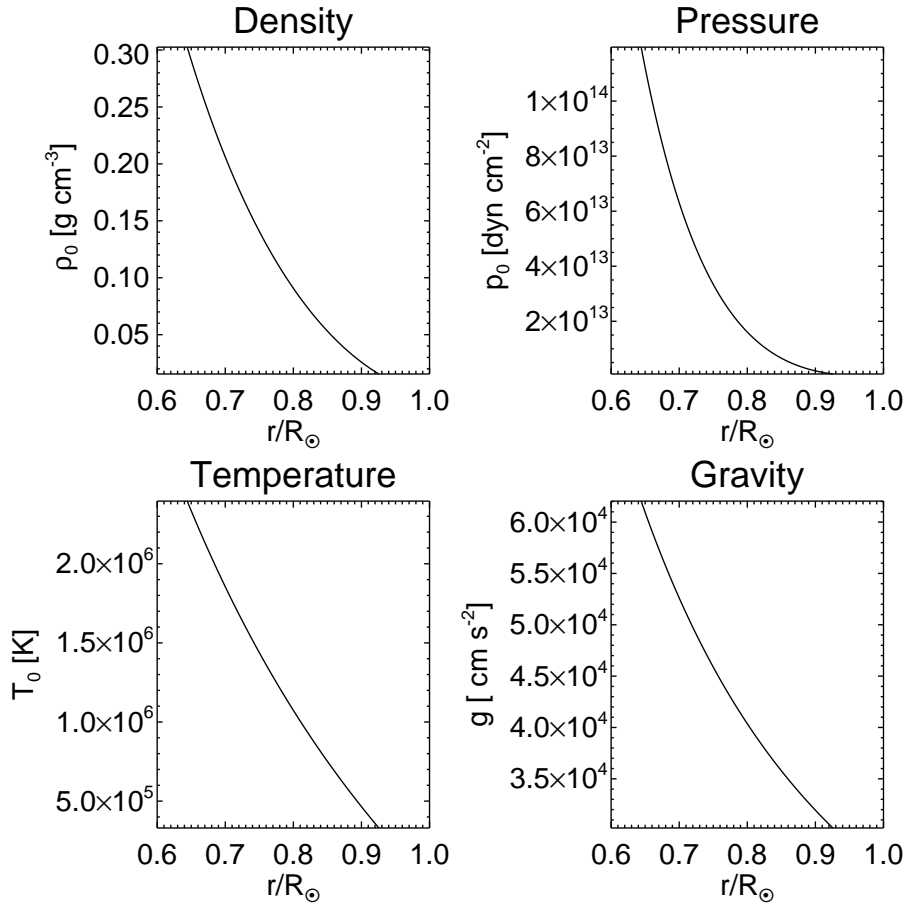


Figure 38: Profiles of density, pressure and temperature as a function of radial distance in the reference state. This stratification is adiabatic.

with

$$f_c(r) = \frac{1}{2} \left[ 1 + \tanh \left( \frac{r - r_{bc}}{d_{bc}} \right) \right], \quad (5.18.28)$$

$$\Delta = d_{\kappa\nu} \tanh^{-1}(2\alpha_{\kappa\nu} - 1), \quad (5.18.29)$$

where  $\nu_{0v}$ ,  $\nu_{0l}$  and  $\kappa_0$  are the values of the turbulent diffusivities within the convection zone, and  $\nu_{os}$  and  $\kappa_{os}$  are the values in the overshoot region. We specify  $\nu_{0l} = \kappa_{0l} = 3 \times 10^{12} \text{ cm}^2 \text{ s}^{-1}$ ,  $\nu_{os} = 6 \times 10^{10} \text{ cm}^2 \text{ s}^{-1}$  and  $\kappa_{os} = 6 \times 10^9 \text{ cm}^2 \text{ s}^{-1}$ , and we treat  $\nu_{0v}$  as a parameter.  $\alpha_{\kappa\nu}$  specifies the values of the turbulent diffusivities at  $r = r_{\text{tran}}$ , i.e.,  $\nu_{tv} = \nu_{os} + \alpha_{\kappa\nu}\nu_{0v}$ ,  $\nu_{tl} = \alpha_{\kappa\nu}\nu_{0l}$  and  $\kappa_t = \kappa_{os} + \alpha_{\kappa\nu}\kappa_0$  at  $r = r_{\text{tran}}$ .  $d_{bc}$  and  $d_{\kappa\nu}$  are the widths of transition. We specify  $\alpha_{\kappa\nu} = 0.1$ ,  $d_{bc} = 0.0125R_\odot$  and  $d_{\kappa\nu} = 0.025R_\odot$ . As already mentioned, the coefficients for turbulent viscosity and the  $\Lambda$  effect are different in our model from those of Rempel's (2005b). There are two reasons for this. One is that we intend to investigate the influence of both effects on stellar differential rotation separately (see §20.2). The other reason is that the formation of a tachocline in a reasonable amount of time requires a finite value (though small) for the coefficient of turbulent viscosity even in the radiative zone, in which there is likely to be weak turbulence (Rempel, 2005b). Fig. 39 shows the profiles of  $\nu_{tv}$ ,  $\nu_{tl}$  and  $\kappa_t$ .

## 18.4 The $\Lambda$ effect

In this study we adopt the non-diffusive part of the Reynolds stress, called the  $\Lambda$  effect. The  $\Lambda$  effect transports angular momentum and generates differential

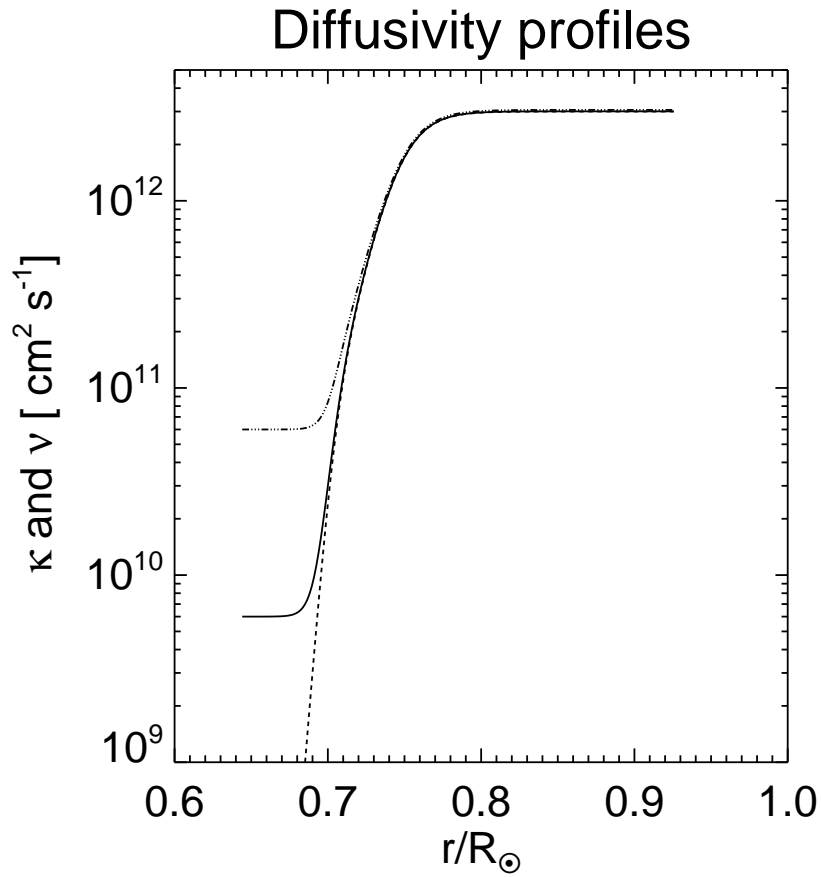


Figure 39: Profiles of diffusivity as a function of radial distance for cases 1-5 and 9-11. The solid line denotes the coefficient of turbulent conductivity  $\kappa_t$ . The dashed line denotes the coefficient of the  $\Lambda$  effect  $\nu_{\Lambda}$ . The dash and three dots line denotes the coefficient of turbulent viscosity  $\nu_{tv}$ .

rotation. The  $\Lambda$  effect tensors are expressed as

$$\Lambda_{r\phi} = \Lambda_{\phi r} = +L(r, \theta) \cos(\theta + \lambda), \quad (5.18.30)$$

$$\Lambda_{\theta\phi} = \Lambda_{\phi\theta} = -L(r, \theta) \sin(\theta + \lambda), \quad (5.18.31)$$

where  $L(r, \theta)$  is the amplitude of the  $\Lambda$  effect and  $\lambda$  denotes the inclination of the flux vector with respect to the rotational axis. We set  $\lambda = 15^\circ$  in all our calculations, so the angular momentum of this direction generates a solar-like surface poleward meridional flow (see §19).  $\Lambda_0$  is a free-parameter. We use for the amplitude of the  $\Lambda$  effect the expressions

$$f(r, \theta) = \sin^l \theta \cos \theta \tanh \left( \frac{r_{\max} - r}{d} \right), \quad (5.18.32)$$

$$L(r, \theta) = \Lambda_0 \Omega_0 \frac{f(r, \theta)}{\max|f(r, \theta)|}, \quad (5.18.33)$$

where  $r_{\max}$  denotes the location of the upper boundary, and  $d = 0.025R_\odot$ . The value of  $l$  needs to be equal to or larger than 2 to ensure regularity near the pole, so we set  $l = 2$ . The  $\Lambda$  effect does not depend on  $v_r$ ,  $v_\theta$  or  $\Omega_1$ , meaning it is a stationary effect. We emphasize that the  $\Lambda$  effect depends on stellar angular velocity  $\Omega_0$ , since the  $\Lambda$  effect is generated by turbulence and Coriolis force. The more rapidly the star rotates, the more angular momentum the  $\Lambda$  effect can transport. Note that we assume that the amplitude of the  $\Lambda$  effect ( $\Lambda_0$ ) and the inclination angle ( $\lambda$ ) do not depend on stellar angular velocity, although both of them are thought to vary with stellar angular velocity. We intend to analyze this variation in the  $\Lambda$ -effect in our future work.

## 18.5 Numerical Settings

Using the modified Lax-Wendroff scheme with TVD artificial viscosity (Davis, 1984), we solve Equations (5.18.1)-(5.18.5) numerically for the northern hemisphere of the meridional plane in  $0.65R_\odot < r < 0.93R_\odot$  and  $0 < \theta < \pi/2$ . We use a uniform resolution of 200 points in the radial direction and 400 points in the latitudinal direction in all of our simulations. Each simulation run is conducted until it reaches a stationary state. All the variables  $\rho_1$ ,  $v_r$ ,  $v_\theta$ ,  $\Omega_1$  and  $s_1$  are equal to zero in the initial condition. At the top boundary ( $r = 0.93R_\odot$ ) we adopt stress-free boundary conditions for  $v_r$ ,  $v_\theta$  and  $\Omega_1$  and set the derivative of  $s_1$  to zero:

$$\frac{\partial v_r}{\partial r} = 0, \quad (5.18.34)$$

$$\frac{\partial}{\partial r} \left( \frac{v_\theta}{r} \right) = 0, \quad (5.18.35)$$

$$\frac{\partial \Omega_1}{\partial r} = 0, \quad (5.18.36)$$

$$\frac{\partial s_1}{\partial r} = 0. \quad (5.18.37)$$

The boundary conditions for  $v_r$ ,  $v_\theta$  and  $s_1$  at the lower boundary ( $r = 0.65R_\odot$ ) are the same as those at the top boundary. Differential rotation connects with the rigidly rotating core at the lower boundary, so we adopt  $\Omega_1 = 0$  there. At both radial boundaries, we set  $\rho_1$  to make the right side of eq. (5.18.2) equal zero. At the

pole and the equator ( $\theta = 0$  and  $\pi/2$ ) we use the symmetric boundary condition:

$$\frac{\partial \rho_1}{\partial \theta} = 0, \quad (5.18.38)$$

$$\frac{\partial \Omega_1}{\partial \theta} = 0, \quad (5.18.39)$$

$$\frac{\partial v_r}{\partial \theta} = 0, \quad (5.18.40)$$

$$v_\theta = 0, \quad (5.18.41)$$

$$\frac{\partial s_1}{\partial \theta} = 0. \quad (5.18.42)$$

Due to the low Mach number of the expected flows, a direct compressible simulation is problematic, so adopting the same technique as Rempel (2005b), we reduce the speed of sound by multiplying the right side of eq. (5.18.1) by  $1/\zeta^2$ . The equation of continuity is therefore replaced with

$$\frac{\partial \rho_1}{\partial t} + \frac{1}{\zeta^2} \text{div}(\rho_0 \mathbf{v}) = 0. \quad (5.18.43)$$

The speed of sound then becomes  $\zeta$  times smaller than the original speed. We use  $\zeta = 200$  in all our calculations. This technique can be used safely in our present study since we only discuss stationary states, so the factor  $\zeta$  becomes unimportant. The validity of this technique is carefully discussed by Rempel (2005b). We test our code by reproducing the results presented by Rempel (2005b) and check the numerical convergence by runs with different grid spacings. After checking and cleaning up at every time step, conservation of total mass, total angular momentum and total energy are maintained through the simulation runs.

## 19 Stellar Differential Rotation and the Taylor-Proudman Theorem

In this section, based on the work of Rempel (2005b), we explain how the sub-adiabatically stratified region can generate solar-like differential rotation. The  $\phi$  component of the vorticity equation can be expressed as

$$\frac{\partial \omega_\phi}{\partial t} = [\dots] + r \sin \theta \frac{\partial \Omega^2}{\partial z} - \frac{g}{\gamma r} \frac{\partial s_1}{\partial \theta}, \quad (5.19.1)$$

where  $\Omega = \Omega_0 + \Omega_1$ , and the  $z$  axis represents the rotational axis. The inertial term and the diffusion term are neglected. If the last term of eq. (5.19.1) is zero, meaning there is no variation in entropy in the latitudinal direction, then  $\partial \Omega^2 / \partial z = 0$  in a stationary state, which is the Taylor-Proudman state. Solar-like differential rotation is generated in four stages.

1. In the northern hemisphere, the  $\Lambda$  effect transports angular momentum in the negative  $z$  direction and generates a negative  $\partial \Omega^2 / \partial z$ .
2. The negative  $\partial \Omega^2 / \partial z$  generates a negative  $\omega_\phi$  due to Coriolis force. This counter-clockwise meridional flow corresponds to a negative  $v_r$  (downflow) at high latitudes and a positive  $v_r$  (upflow) at low latitudes.
3. As we mentioned in Section 18.2, downflow (upflow) generates positive (negative) entropy perturbations in the subadiabatically stratified layer beneath the convection zone ( $\delta < 0$ ). Meridional flow can generate positive entropy perturbations at high latitudes and negative entropy perturbations at low latitudes. Therefore,  $\partial s_1 / \partial \theta$  becomes negative in the overshoot region.
4. The negative  $\partial s_1 / \partial \theta$  also keeps  $\partial \Omega^2 / \partial z$  negative in a stationary state.

Table 1: Significant parameters of the simplified model

Case	$\Omega_0$ [nHz]	$\nu_{0v}$ [cm <sup>2</sup> s <sup>-1</sup> ]	$\Lambda_0$
1	$1\Omega_\odot = 430$	$3 \times 10^{12}$	1
2	$2\Omega_\odot = 860$	$3 \times 10^{12}$	1
3	$4\Omega_\odot = 1720$	$3 \times 10^{12}$	1
4	$8\Omega_\odot = 3440$	$3 \times 10^{12}$	1
5	$16\Omega_\odot = 6880$	$3 \times 10^{12}$	1
6	$1\Omega_\odot = 430$	$12 \times 10^{12}$	1
7	$1\Omega_\odot = 430$	$6 \times 10^{12}$	1
8	$1\Omega_\odot = 430$	$1.5 \times 10^{12}$	1
9	$1\Omega_\odot = 430$	$3 \times 10^{12}$	2
10	$1\Omega_\odot = 430$	$3 \times 10^{12}$	0.5
11	$1\Omega_\odot = 430$	$3 \times 10^{12}$	0.25

The profile of angular velocity in the convection zone is determined by a balance of angular momentum transport from meridional flow and a reduction in meridional flow from buoyancy force at the subadiabatic layer.

## 20 Results and discussion

We run simulations for eleven cases, with Table 1 showing the parameters for each case.

### 20.1 Stellar Differential Rotation

In this section, we discuss the cases with angular velocities up to 16 times the solar value (represented by  $\Omega_\odot$ ), placing an emphasis on the morphology of stellar differential rotation. Fig. 40 shows the results of our calculations which correspond to cases 1-5 in Table 1. It is found that the larger stellar angular velocity is, the more likely it is for differential rotation to be in the Taylor-Proudman state, in which the contour lines of the angular velocity are parallel to the rotational axis. To evaluate

these results quantitatively, we define a parameter which denotes the morphology of differential rotation. We call it the Non-Taylor-Proudman parameter (hereafter the NTP parameter), which is expressed as

$$P_{\text{nTP}} = \frac{1}{R_{\odot}^2 \Omega_0^2} \int \frac{\partial \Omega_1^2}{\partial z} dV = \frac{1}{R_{\odot}^2 \Omega_0^2} \int \left( \cos \theta \frac{\partial}{\partial r} - \frac{\sin \theta}{r} \frac{\partial}{\partial \theta} \right) \Omega_1^2 dV, \quad (5.20.1)$$

where  $\Omega_0$  is the angular velocity of the radiative zone. When the NTP parameter is zero, differential rotation is in the Taylor-Proudman state. Conversely, differential rotation is far from the Taylor-Proudman state with a large absolute value of the NTP parameter. The value of the NTP parameter with various stellar angular velocities is shown in Fig. 41. The NTP monotonously decreases with increases in stellar angular velocity. These results indicate that with large stellar angular velocity values, differential rotation approaches the Taylor-Proudman state. These results are counter-intuitive, however, since we do not expect differential rotation to approach the Taylor-Proudman state with increasing stellar angular velocity values, since the  $\Lambda$  effect, which is a driver of the deviation from the Taylor-Proudman state, is proportional to stellar angular velocity  $\Omega_0$ . These are the most significant findings of this paper, so hereafter in this section we discuss these unexpected results.

We next discuss the temperature difference between the equator and the pole at the base of the convection zone ( $r = 0.71R_{\odot}$ ). Since temperature is given as a function of entropy by

$$T_1 = \frac{T_0}{\gamma} \left[ s_1 + (\gamma - 1) \frac{p_1}{p_0} \right], \quad (5.20.2)$$

and it is more objective than entropy, we use it here for discussing the thermal structure of the simulation results in the convection zone. Further, although it is mentioned in §19 that entropy gradient is crucial for breaking the Taylor-Proudman

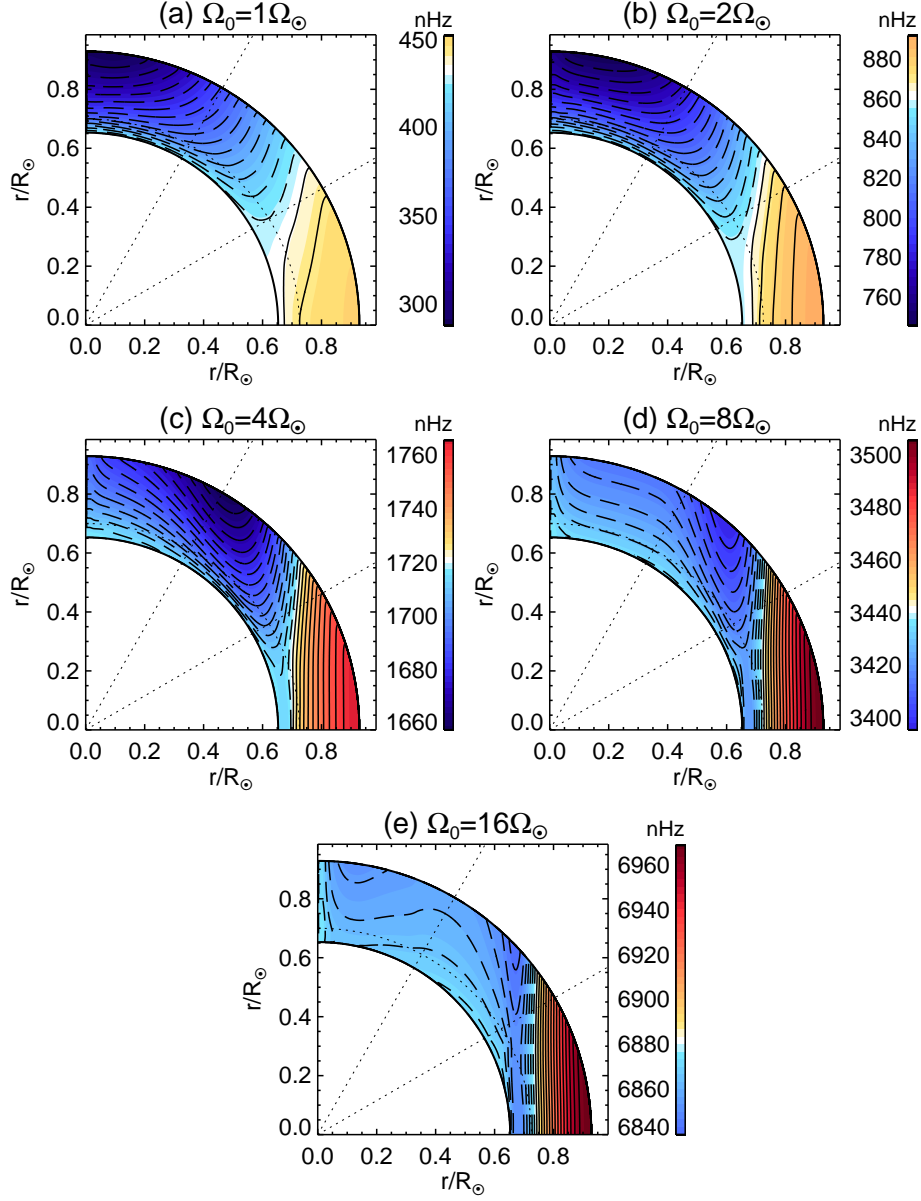


Figure 40: Rotation profiles of the simulation results. Panels (a)-(e) correspond to cases 1-5, respectively. The stellar rotation rate for each case is given at the top of each panel. The area of red and solid lines (blue and dashed lines) rotates faster (slower) than the rigidly rotating core at the bottom boundary. Color bars are given for angular velocity  $\Omega/2\pi = (\Omega_0 + \Omega_1)/2\pi$  in the unit of nHz. The dotted lines in each panel indicate the base of the convection zone ( $r = 0.71R_\odot$ ) and the colatitudes  $\theta = 30^\circ$  and  $\theta = 60^\circ$ .

constraint, the temperature difference can be used as its proxy. Fig. 42 shows the relationship between stellar angular velocity  $\Omega_0$  and temperature difference  $\Delta T$  at  $r = 0.71R_\odot$ , where  $\Delta T = \max(T_1(r_{bc}, \theta)) - \min(T_1(r_{bc}, \theta))$ . Although the temperature difference monotonously increases with larger stellar angular velocity values, it is not enough to make the rotational profile largely deviate from the Taylor-Proudman state. This can be explained by using the thermal wind equation, which is a steady state solution of eq. (5.19.1):

$$0 = r \sin \theta \frac{\partial \Omega^2}{\partial z} - \frac{g}{\gamma r} \frac{\partial s_1}{\partial \theta}. \quad (5.20.3)$$

This equation indicates that, for a given value of the NTP, we need an entropy gradient proportional to  $\Omega_0^2$ . However, our simulation results show that  $\Delta T \propto \Omega_0^{0.58}$ , which means that as  $\Omega_0$  increases, the thermal driving force becomes insufficient to push differential rotation away from the Taylor-Proudman state. In other words, the latitudinal entropy gradient in rapidly rotating stars is so small that differential rotation stays close to the Taylor-Proudman state. In our model, meridional flow generates latitudinal entropy gradient at the base of the convection zone. It is conjectured that the insufficient thermal drive is due to a slow meridional flow.

We next investigate the dependence of meridional flow on stellar angular velocity. Fig. 43 shows the radial profile of latitudinal velocity  $v_\theta$  at  $\theta = 45^\circ$ , using the results of cases 1, 2 and 9. In case 2, stellar angular velocity is twice that of case 1 (the solar value). In case 9, stellar angular velocity is equal to the solar value, and the amplitude of the  $\Lambda$  effect is two times the value in case 1. Fig. 43 shows that meridional flow does not depend on stellar angular velocity, while it correlates with the  $\Lambda$  effect. Considering eq. (5.18.33), the  $\Lambda$  effect increases with larger values of stellar angular velocity, since the amplitude of the  $\Lambda$  effect is proportional to  $\Omega_0$ .

The reason why differential rotation in rapidly rotation stars is close to the Taylor-Proudman state is that meridional flow does not become fast with large stellar angular velocity values.

We interpret the result that meridional flow does not depend on stellar angular velocity as follows. With large values of stellar angular velocity, more angular momentum is transported, so meridional flow obtains more energy from differential rotation. Coriolis force, however, is stronger with larger stellar angular velocity values, and this stronger Coriolis force bends the latitudinal meridional flow  $v_\theta$  quickly and generates radial meridional flow  $v_r$ . After this bending occurs, meridional flow loses its energy due to buoyancy. This mechanism is so efficient that most of the meridional flow energy (about 99 %) is transformed into internal energy due to buoyancy (Rempel, 2005a). Our results (Fig. 43) indicate that with higher stellar angular velocity (case 2), the above mechanism suppresses meridional flow. However, when only the  $\Lambda$  effect is large (case 9), this does not occur.

## 20.2 Angular Velocity Difference on the Surface

In this subsection we discuss angular velocity difference  $\Delta\Omega$  at the surface and the relationship between our results and previous observations. We conduct numerical simulations to investigate the physical process which determines  $\Delta\Omega$  (cases 1, 6-11). We define angular velocity difference as  $\Delta\Omega = \max(\Omega_1(r_{\max}, \theta)) - \min(\Omega_1(r_{\max}, \theta))$ .

$\Delta\Omega$  is determined by two opposing effects, a smoothing effect from turbulent viscosity and a steepening effect from the  $\Lambda$  effect. In a stationary state these two effects cancel each other out. Latitudinal flux for turbulent viscosity and the  $\Lambda$  effect can be written as  $\rho_0\nu_{0v}\Delta\Omega/\Delta\theta$  and  $\rho_0\nu_{0l}\Lambda_0\Omega_0$ , respectively. Because these two have

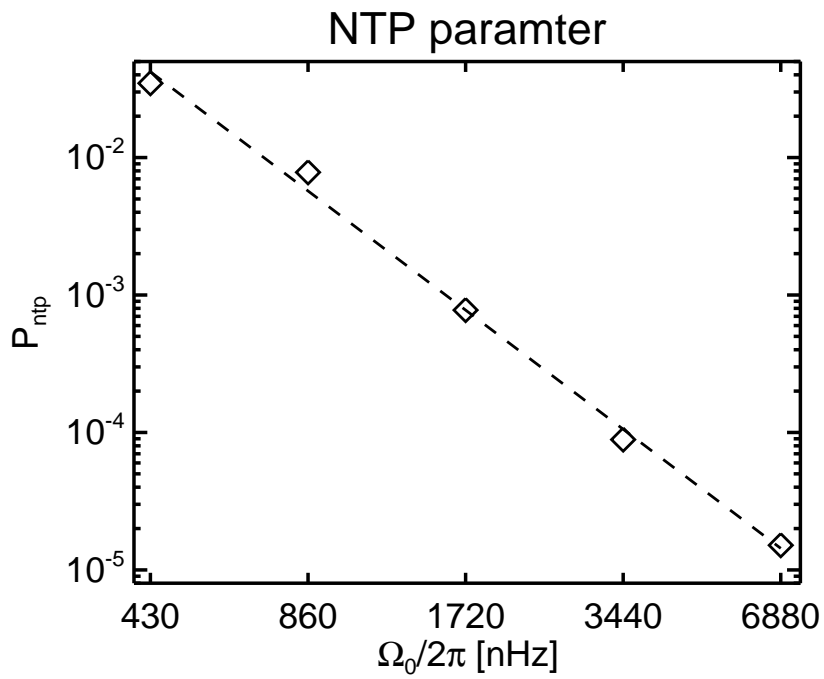


Figure 41: NTP parameter as a function of stellar angular velocity  $\Omega_0/2\pi$ . The dashed line is the fit to the results showing a power-law function with an index of  $-2.9$ .

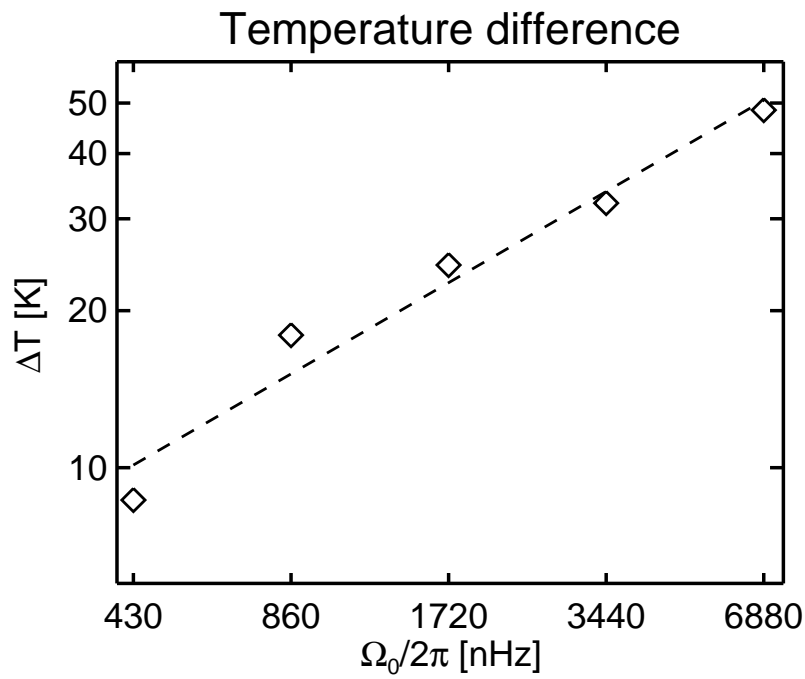


Figure 42: Temperature difference at the base of the convection zone ( $r = 0.71R_\odot$ ) as a function of stellar angular velocity ( $\Omega_0/2\pi$ ). The dashed line is the fit to the results showing a power-law function with an index of 0.58.

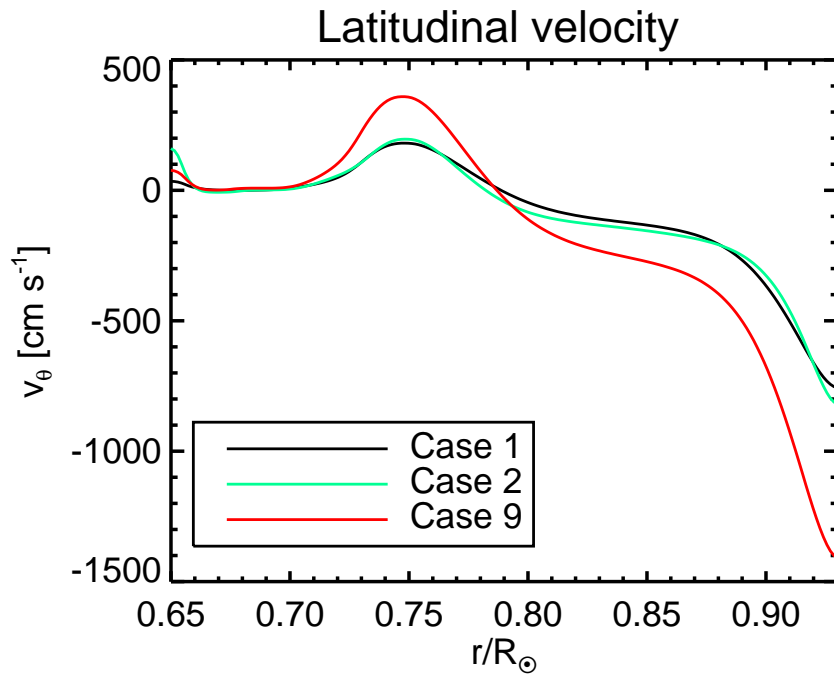


Figure 43: Profiles of latitudinal velocity ( $v_\theta$ ) at colatitude  $\theta = 45^\circ$  as a function of radial distance. In case 1, stellar angular velocity is the solar value, and the amplitude of angular momentum transport  $\Lambda_0 = 1$ . In case 2, stellar angular velocity  $\Omega_0 = 2\Omega_\odot$ . In case 9, amplitude of the turbulent angular momentum transport  $\Lambda_0 = 2$ .

approximately the same value,  $\Delta\Omega$  can be estimated as

$$\Delta\Omega \sim \frac{\nu_{0l}}{\nu_{0v}} \Lambda_0 \Omega_0 \Delta\theta, \quad (5.20.4)$$

where  $\Delta\theta$  denotes the differential rotation region.

In order to confirm eq. (5.20.4), we conduct two sets of simulations, firstly varying the value of turbulent viscosity ( $\nu_{0v}$ ), and secondly the amplitude of the  $\Lambda$  effect ( $\Lambda_0$ ). Note that the setting for turbulent viscosity does not reflect a real situation, since the coefficients of turbulent viscosity and the  $\Lambda$  effect should have a common value. Nonetheless, this is necessary for the purpose of our investigation. The simulation results are shown in Figures 44 and 45. We obtain  $\Delta\Omega \propto \nu_{0v}^{-0.88}$  and  $\Delta\Omega \propto \Lambda_0^{1.1}$ , which are consistent with eq. (5.20.4).

Fig. 46 shows the results of the dependence of  $\Delta\Omega$  on  $\Omega_0$  (Cases 1-5). Asterisks denote the difference at the surface between the equator and the pole, squares show the difference between the equator and the colatitude  $\theta = 45^\circ$ , and triangles are the difference between the equator and the colatitude  $\theta = 60^\circ$ . The difference at low latitudes (squares and triangles) monotonously increase with stellar angular velocity. However this is not the case for angular velocity difference between the equator and the pole (asterisk). As we discussed in §20.1, when stellar rotation velocity is high, the Taylor-Proudman state is achieved, meaning the gradient of angular velocity at the surface concentrates in lower latitudes. Due to this concentration,  $\Delta\theta$  becomes smaller in Eq. (5.20.4) with larger values of  $\Omega_0$ . Thus,  $\Delta\Omega_0$  does not show an explicit dependence on  $\Omega_0$ . At low latitudes,  $\Delta\theta$  is fixed and the angular velocity difference increases with stellar angular velocity. We obtain  $\Delta\Omega \propto \Omega_0^{0.43}$  (between the equator and the colatitude  $\theta = 45^\circ$ : squares) and  $\Delta\Omega \propto \Omega_0^{0.55}$  (between the equator and the colatitude  $\theta = 60^\circ$ : triangles). This indicates that  $\Delta\Omega/\Omega_0$  decreases with stellar

angular velocity. These results are consistent with previous stellar observations (Donahue et al., 1996; Reiners & Schmitt, 2003; Barnes et al., 2005).

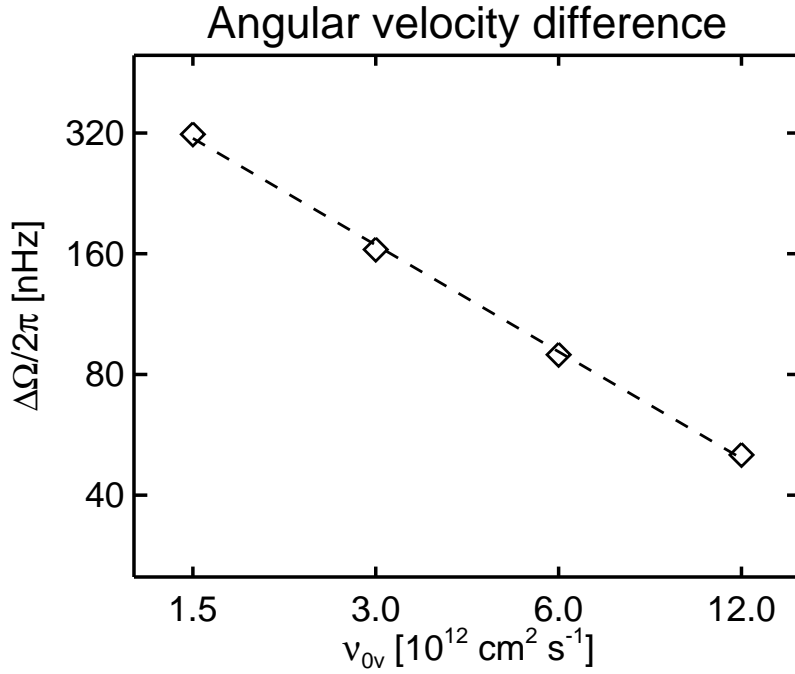


Figure 44: Angular velocity difference at the surface as a function of the coefficient of turbulent viscosity  $\nu_{0v}$ . The dashed line is the fit to the results showing a power-law function with an index of  $-0.88$ .

## 21 Summary

We have investigated differential rotation in rapidly rotating stars using a mean field model. This work is significant because it can be used as a base for further research on stellar activity cycles, which are most likely caused by the dynamo action of differential rotation in the stellar convection zone.

First, we investigated the morphology of differential rotation in rapidly rotating stars. Although more angular momentum is transported by convection with higher

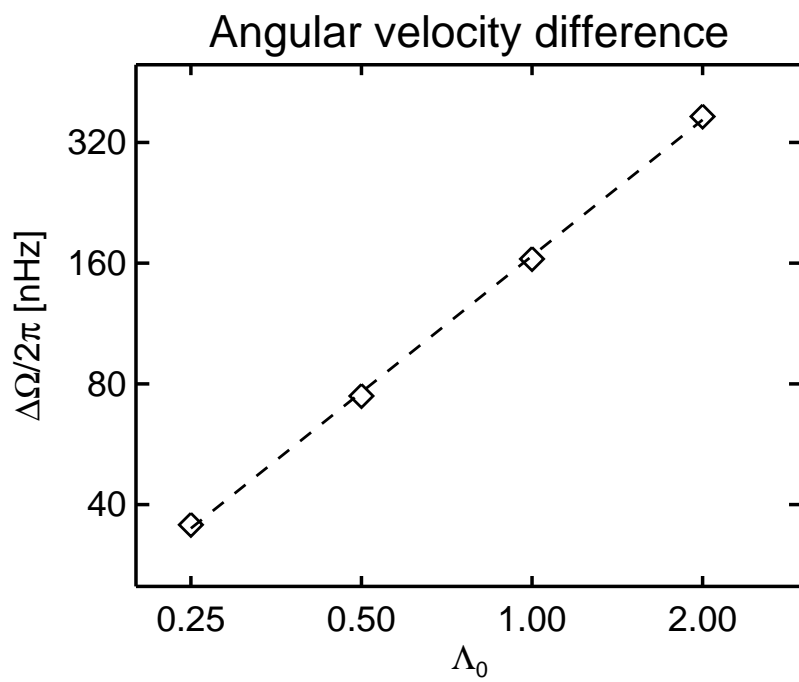


Figure 45: Angular velocity difference at the surface as a function of the amplitude of the angular momentum transport  $\Lambda_0$ . The dashed line is the fit to the results showing a power-law function with an index of 1.1.

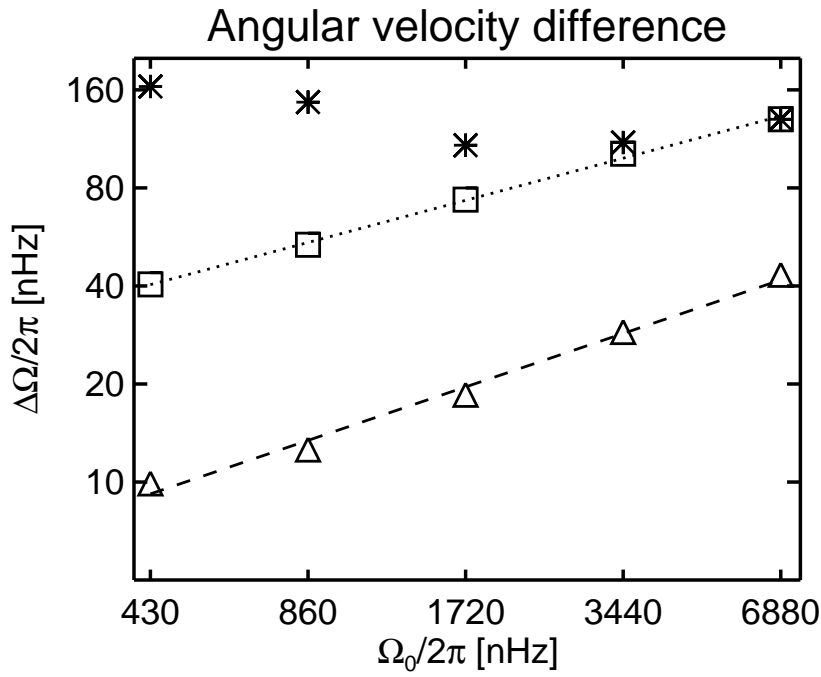


Figure 46: Angular velocity difference in three regions. Asterisks, squares and triangles represent the equator and the pole, the equator and the colatitude  $\theta = 45^\circ$  and the equator and the colatitude  $\theta = 30^\circ$ , respectively. The dashed and dotted lines are the fits to the results showing a power-law function with indices of 0.43 (squares) and 0.55 (triangles).

stellar angular velocity, the Coriolis force is stronger than in the solar case, so meridional flow slows from a loss of energy due to buoyancy. In our model, meridional flow generates latitudinal entropy gradient in the subadiabatically stratified overshoot region. Since the meridional flow is not fast, the entropy gradient is insufficient to move differential rotation far from the Taylor-Proudman state in rapidly rotating stars. As a result, the differential rotation of stars with high stellar angular velocity is close to the Taylor-Proudman state.

In comparison with three dimensional calculations (Brown et al., 2008), the advantage of our study is that entropy gradient can be calculated with a reasonable physical basis, which satisfies the solar case. There is also a possibility that our calculated entropy gradient at the base of the convection zone can be used as a boundary condition for a self-consistent three dimensional simulation of stellar convection (Miesch et al., 2006).

Next, we investigated angular velocity difference at the surface. The  $\Lambda$  effect causes spatial difference in the rotation profile, while turbulent viscosity reduces the difference. Angular velocity difference  $\Delta\Omega$  is determined in eq. (5.20.4), which is then used to investigate differential rotation in rapidly rotating stars. Since stellar rotation is close to the Taylor-Proudman state, and the radiative core is rotating rigidly, differential rotation is concentrated at low latitudes with high stellar angular velocity. This concentration leads to a small  $\Delta\theta$  in eq. (5.20.4). Therefore, only at low latitudes our model is consistent with stellar observations.

Our conclusions are as follows: (1) Differential rotation approaches the Taylor-Proudman state when stellar rotation is faster than solar rotation. (2) Meridional flow is insensitive to stellar angular velocity. (3) Turbulent viscosity and turbulent

angular momentum transport determine the spatial difference of angular velocity  $\Delta\Omega$ . (4) The results of our mean field model can explain observations of stellar differential rotation.

Our future work will focus on the stellar MHD dynamo. Several investigations have been conducted on the stellar dynamo using a kinematic dynamo framework (Dikpati et al., 2001; Charbonneau & Saar, 2001; Moss & Sokoloff, 2009; Jouve et al., 2010). Since, under such a framework, only the magnetic induction equation is solved using a given velocity field, solving a linear equation, such analysis does not give sufficient information on the strength of the dynamo-generated stellar magnetic field. To obtain the full amplitude of the stellar magnetic field, the feedback to the velocity field is required, i.e., an MHD framework. Adopting a similar approach to Rempel (2006), we can use the results of this paper to investigate the strength of the stellar magnetic field. Recent observations of the strength of the magnetic field generated by stellar differential rotation have been conducted using spectroscopy (e.g. Petit et al., 2008). A comparison of these observations and numerical calculations of the stellar dynamo could give new insight into the stellar magnetic field. Finally, our stellar MHD dynamo study would also contribute to the understanding of recent investigations into stellar magnetic cyclic activity periods (Noyes et al., 1984; Saar & Brandenburg, 1999).

## Part VI

# Future perspective

In this master thesis, we investigate the problems related to the solar and stellar magnetic cycles and the large scale structure of the velocity field in the mean field model. These studies give us significant information on these issues. By using the mean field approach, however, we cannot understand the solar and stellar dynamo self-consistently. As explained in §V, the convection has a crucial role on the angular momentum transport in the solar convection zone. The magnetic field generated by dynamo action is also affected by the convection.

To solve the convection in the solar interior is an important way to understand the physical processes of the solar and stellar magnetic cycles and their large scale flow. However, the calculation for the solar convection has some difficulties. One of the most important difficulties is caused by the low Mach number due to the low superadiabaticity. The Mach number at the base of the convection zone is thought to be 0.001 (Stix, 2004). It means that the speed of sound is much faster than the speed of convection. We must take a small time step ( $\Delta t$ ) due to this high speed of sound and under the CFL condition when adopting an explicitly time-advancing method.

The anelastic approximation is widely used to solve this difficulty (Glatzmaier, 1984; Miesch et al., 2000). In the anelastic approximation, the speed of sound is assumed to be infinite by using  $\nabla \cdot (\rho_0 \mathbf{v}) = 0$  as the equation of continuity, where  $\rho_0$  is the background density and  $\mathbf{v}$  is the fluid velocity. This approximation has been successful in reproducing the solar convection to some extent (e.g. Miesch et al.,

2000). It is, however, now approaching a resource limit for the usage of massively parallel computers which have more than 10,000 CPUs. This is because of the highly demanding amount of global communication among CPUs that is necessary for solving the elliptic equation in this approximation. It is estimated that the linear scaling of the computational speed is limited at most to 2000 CPUs (Miesch private communication).

Therefore we try using another method, i.e. the RSST (Reduced Speed of Sound Technique). In the RSST the speed of sound is reduced by varying the equation of continuity as,

$$\frac{\partial \rho}{\partial t} = -\nabla \cdot \left( \frac{\rho \mathbf{v}}{\xi^2} \right). \quad (6.21.1)$$

where  $\xi (> 1)$  is the reducing rate of the speed of sound. With this equation of continuity, the effective speed of sound is  $\xi$  times slower than the original one. The CFL condition is relaxed. The validity of this method is confirmed by my recent work (Hotta et al., 2011 in prep). By comparing the results of simulations of thermal convections, we found that the essential behavior does not change by this method until the “effective” Mach number reaches 0.4. In the real Sun, since the Mach number is expected below 0.003 at  $r = 0.95R_{\odot}$ , we may use the RSST up to  $\xi = 130$ .

There are two advantages of the RSST compared with the anelastic approximation. First is good scaling with a large number of CPUs. Using the RSST, the system includes only hyperbolic equations, so global communication is not required. The second advantage is the inhomogeneous grid. In most anelastic calculations, the Fourier transformation is frequently carried out. A uniform grid is necessary for the fast Fourier transformation. The convection and the magnetic field are not

homogeneous in the solar convection zone. Therefore an inhomogeneous grid, such as AMR (Adaptive Mesh Refinement), with the RSST is a powerful way to investigate the physics in the solar convection zone.

# Acknowledgments

I gratefully thank my supervisor, Dr. Takaaki Yokoyama. He leads me to the wonderful solar physics world. He kindly teaches me how to study physics and how interesting solar physics is. I appreciate my seminar members, Yusuke Iida, Naomasa Kitagawa, Shin Toriumi and Yuki Matsui. They give me great advices and suggestions. I am thankful to Dr. Matthias Rempel for his great assistance of my study. Dr. Hiroaki Isobe gives me advices for my first paper Hotta & Yokoyama (2010a). Numerical computations were carried out on the general-purpose PC farm at the Center for Computational Astrophysics (CfCA) of the National Astronomical Observatory of Japan, NEC SX-8 at Nobeyama Radio Observatory, NRO, of National Astronomical Observatory of Japan, and also on NEC SX-6 at Space Science Simulator, SSS of Japan Aerospace Exploration Agency, JAXA. I want to thank the Overseas Internship Program for Outstanding Young Earth and Planetary Researchers (OIYR Program). I have greatly benefited from the proofreading/editing assistance from the GCOE program. I am deeply grateful to my parents for their help.

## References

- Babcock, H. D. 1959, *ApJ*, 130, 364
- Babcock, H. W. 1961, *ApJ*, 133, 572
- Babcock, H. W., & Babcock, H. D. 1955, *ApJ*, 121, 349
- Baliunas, S. L., et al. 1995, *ApJ*, 438, 269
- Barnes, J. R., Cameron, A. C., Donati, J., James, D. J., Marsden, S. C., & Petit, P. 2005, *MNRAS*, 357, L1
- Bonanno, A., Elstner, D., Rüdiger, G., & Belvedere, G. 2002, *A&A*, 390, 673
- Brown, B. P., Browning, M. K., Brun, A. S., Miesch, M. S., & Toomre, J. 2008, *ApJ*, 689, 1354
- Carrington, R. C. 1858, *MNRAS*, 19, 1
- Cattaneo, F., & Hughes, D. W. 1996, *Phys. Rev. E*, 54, R4532
- Chapman, S. 1954, *ApJ*, 120, 151
- Charbonneau, P. 2005, *Living Reviews in Solar Physics*, 2, 2
- Charbonneau, P., & Saar, S. H. 2001, in *Astronomical Society of the Pacific Conference Series*, Vol. 248, *Magnetic Fields Across the Hertzsprung-Russell Diagram*, ed. G. Mathys, S. K. Solanki, & D. T. Wickramasinghe, 189
- Chatterjee, P., & Choudhuri, A. R. 2006, *Sol. Phys.*, 239, 29
- Chatterjee, P., Nandy, D., & Choudhuri, A. R. 2004, *A&A*, 427, 1019

- Choudhuri, A. R. 2003, *Sol. Phys.*, 215, 31
- Choudhuri, A. R., Chatterjee, P., & Jiang, J. 2007, *Physical Review Letters*, 98, 131103
- Choudhuri, A. R., & Karak, B. B. 2009, *Research in Astronomy and Astrophysics*, 9, 953
- Choudhuri, A. R., Schussler, M., & Dikpati, M. 1995, *A&A*, 303, L29
- Cowling, T. G. 1934, *MNRAS*, 94, 768
- . 1953, *Solar Electrodynamics*, ed. Kuiper, G. P., 532–+
- Davis, S. 1984, *Icase Report*, 84, 20
- Dikpati, M., & Charbonneau, P. 1999, *ApJ*, 518, 508
- Dikpati, M., & Choudhuri, A. R. 1994, *A&A*, 291, 975
- Dikpati, M., Corbard, T., Thompson, M. J., & Gilman, P. A. 2002, *ApJL*, 575, L41
- Dikpati, M., de Toma, G., Gilman, P. A., Arge, C. N., & White, O. R. 2004, *ApJ*, 601, 1136
- Dikpati, M., & Gilman, P. A. 2001, *ApJ*, 559, 428
- . 2006, *ApJ*, 649, 498
- . 2007, *Sol. Phys.*, 241, 1
- Dikpati, M., Gilman, P. A., & Rempel, M. 2003, *ApJ*, 596, 680

- Dikpati, M., Saar, S. H., Brummell, N., & Charbonneau, P. 2001, in *Astronomical Society of the Pacific Conference Series*, Vol. 248, *Magnetic Fields Across the Hertzsprung-Russell Diagram*, ed. G. Mathys, S. K. Solanki, & D. T. Wickramasinghe, 235
- Donahue, R. A., Saar, S. H., & Baliunas, S. L. 1996, *ApJ*, 466, 384
- D’Silva, S., & Choudhuri, A. R. 1993, *A&A*, 272, 621
- Fan, Y. 2009a, *Living Reviews in Solar Physics*, 6, 4
- Fan, Y. 2009b, in *Astronomical Society of the Pacific Conference Series*, Vol. 416, *Astronomical Society of the Pacific Conference Series*, ed. M. Dikpati, T. Arentoft, I. González Hernández, C. Lindsey, & F. Hill, 489–+
- Ferriz-Mas, A., Schmitt, D., & Schuessler, M. 1994, *A&A*, 289, 949
- Garaud, P., & Brummell, N. H. 2008, *ApJ*, 674, 498
- Giles, P. M., Duvall, T. L., Scherrer, P. H., & Bogart, R. S. 1997, *Nature*, 390, 52
- Gilman, P. A., & Miesch, M. S. 2004, *ApJ*, 611, 568
- Gilman, P. A., & Miller, J. 1981, *ApJS*, 46, 211
- Glatzmaier, G. A. 1984, *Journal of Computational Physics*, 55, 461
- Goel, A., & Choudhuri, A. R. 2009, *Research in Astronomy and Astrophysics*, 9, 115
- Guerrero, G., & de Gouveia Dal Pino, E. M. 2007, *A&A*, 464, 341

- Haber, D. A., Hindman, B. W., Toomre, J., Bogart, R. S., Larsen, R. M., & Hill, F. 2002, *ApJ*, 570, 855
- Hale, G. E. 1908, *ApJ*, 28, 315
- Hale, G. E., Ellerman, F., Nicholson, S. B., & Joy, A. H. 1919, *ApJ*, 49, 153
- Hale, G. E., & Nicholson, S. B. 1925, *ApJ*, 62, 270
- Harten, A. 1983, *Journal of Computational Physics*, 49, 357
- Hathaway, D. H. 2010, *Living Reviews in Solar Physics*, 7, 1
- Hathaway, D. H., et al. 1996, *Science*, 272, 1306
- Hotta, H., & Yokoyama, T. 2010a, *ApJ*, 709, 1009
- . 2010b, *ApJL*, 714, L308
- Howard, R., & Harvey, J. 1970, *Sol. Phys.*, 12, 23
- Howe, R., Christensen-Dalsgaard, J., Hill, F., Komm, R., Schou, J., & Thompson, M. J. 2009, *ApJL*, 701, L87
- Hoyt, D. V., & Schatten, K. H. 1997, *The role of the sun in climate change*
- Jiang, J., Chatterjee, P., & Choudhuri, A. R. 2007, *MNRAS*, 381, 1527
- Jouve, L., Brown, B. P., & Brun, A. S. 2010, *A&A*, 509, A32
- Kichatinov, L. L., & Rudiger, G. 1993, *A&A*, 276, 96
- Kitchatinov, L. L., & Rüdiger, G. 1995, *A&A*, 299, 446

- Krause, F., & Rädler, K. 1980, Mean-field magnetohydrodynamics and dynamo theory, ed. Goodman, L. J. & Love, R. N.
- Küker, M., Rüdiger, G., & Schultz, M. 2001, *A&A*, 374, 301
- Leighton, R. B. 1969, *ApJ*, 156, 1
- Miesch, M. S. 2005, *Living Reviews in Solar Physics*, 2, 1
- Miesch, M. S., Brun, A. S., & Toomre, J. 2006, *ApJ*, 641, 618
- Miesch, M. S., Elliott, J. R., Toomre, J., Clune, T. L., Glatzmaier, G. A., & Gilman, P. A. 2000, *ApJ*, 532, 593
- Miesch, M. S., & Toomre, J. 2009, *Annual Review of Fluid Mechanics*, 41, 317
- Moreno-Insertis, F. 1983, *A&A*, 122, 241
- Moss, D., & Sokoloff, D. 2009, *A&A*, 497, 829
- Muñoz-Jaramillo, A., Nandy, D., & Martens, P. C. H. 2009, *ApJ*, 698, 461
- Nandy, D., & Choudhuri, A. R. 2002, *Science*, 296, 1671
- Nishikawa, N., & Kusano, K. 2008, *Physics of Plasmas*, 15, 082903
- Noyes, R. W., Weiss, N. O., & Vaughan, A. H. 1984, *ApJ*, 287, 769
- Parker, E. N. 1955, *ApJ*, 122, 293
- . 1975, *ApJ*, 198, 205
- . 1979, *Cosmical magnetic fields: Their origin and their activity*, ed. Parker, E. N.

- Petit, P., et al. 2008, MNRAS, 388, 80
- Priest, E. R. 1987, Solar magneto-hydrodynamics., ed. Priest, E. R.
- Reiners, A., & Schmitt, J. H. M. M. 2003, A&A, 398, 647
- Rempel, M. 2005a, ApJ, 631, 1286
- . 2005b, ApJ, 622, 1320
- . 2006, ApJ, 647, 662
- Rubin, E. L., & Burstein, S. Z. 1967, Journal of Computational Physics, 2, 178
- Saar, S. H., & Brandenburg, A. 1999, ApJ, 524, 295
- Schwabe, M. 1843, Astronomische Nachrichten, 20, 283
- Spitzer, L. 1956, Physics of Fully Ionized Gases, ed. Spitzer, L.
- Spruit, H. C. 1974, Sol. Phys., 34, 277
- Stix, M. 2004, The sun : an introduction, ed. Stix, M.
- Thompson, M. J., Christensen-Dalsgaard, J., Miesch, M. S., & Toomre, J. 2003, ARAA, 41, 599
- Tsuneta, S., et al. 2008, ApJ, 688, 1374
- van Ballegoijen, A. A., & Choudhuri, A. R. 1988, ApJ, 333, 965
- Vorontsov, S. V., Christensen-Dalsgaard, J., Schou, J., Strakhov, V. N., & Thompson, M. J. 2002, Science, 296, 101

- Wang, Y., Nash, A. G., & Sheeley, Jr., N. R. 1989, *ApJ*, 347, 529
- Wang, Y., & Sheeley, Jr., N. R. 1991, *ApJ*, 375, 761
- Wilson, O. C. 1968, *ApJ*, 153, 221
- . 1978, *ApJ*, 226, 379
- Wittmann, A. D., & Xu, Z. T. 1987, *A&AS*, 70, 83
- Wolf, R. 1861, *MNRAS*, 21, 77
- Wolf, R. 1877, *Geschichte der Astronomie*
- Yeates, A. R., Nandy, D., & Mackay, D. H. 2008, *ApJ*, 673, 544
- Yoshimura, H. 1975, *ApJ*, 201, 740

# Appendix

## A List of Symbols

The symbol list for the General introduction (§I) is showed.

## B Vector Formula

### B.1 General Formula

This appendix shows the formulas which is required for this thesis.

$$\nabla \times (f\mathbf{U}) = f(\nabla \times \mathbf{U}) + (\nabla f) \times \mathbf{U} \quad (6.2.1)$$

$$\nabla \times (\mathbf{U} \times \mathbf{V}) = (\mathbf{V} \cdot \nabla)\mathbf{U} - \mathbf{V}(\nabla \cdot \mathbf{U}) - (\mathbf{U} \cdot \nabla)\mathbf{V} + \mathbf{U}(\nabla \cdot \mathbf{V}) \quad (6.2.2)$$

### B.2 Formular in Spherical Polar Coordinate

$$\nabla f = \left( \frac{\partial f}{\partial r}, \frac{1}{r} \frac{\partial f}{\partial \theta}, \frac{1}{r \sin \theta} \frac{\partial f}{\partial \phi} \right) \quad (6.2.3)$$

$$\nabla \cdot \mathbf{A} = \frac{1}{r^2} \frac{\partial}{\partial r} (r^2 A_r) + \frac{1}{r \sin \theta} \frac{\partial}{\partial \theta} (\sin \theta A_\theta) + \frac{1}{r \sin \theta} \frac{\partial A_\phi}{\partial \phi} \quad (6.2.4)$$

$$\Delta f = \frac{1}{r^2} \frac{\partial}{\partial r} \left( r^2 \frac{\partial f}{\partial r} \right) + \frac{1}{r^2 \sin \theta} \frac{\partial}{\partial \theta} \left( \sin \theta \frac{\partial f}{\partial \theta} \right) + \frac{1}{r^2 \sin^2 \theta} \frac{\partial^2 f}{\partial \phi^2} \quad (6.2.5)$$

$$(\nabla \times \mathbf{A})_r = \frac{1}{r \sin \theta} \left( \frac{\partial}{\partial \theta} (A_\phi \sin \theta) - \frac{\partial A_\theta}{\partial \phi} \right) \quad (6.2.6)$$

$$(\nabla \times \mathbf{A})_\theta = \frac{1}{r \sin \theta} \frac{\partial}{\partial \phi} A_r - \frac{1}{r} \frac{\partial}{\partial r} (r A_\phi) \quad (6.2.7)$$

$$(\nabla \times \mathbf{A})_\phi = \frac{1}{r} \left( \frac{\partial}{\partial r} (r A_\theta) - \frac{\partial}{\partial \theta} A_r \right) \quad (6.2.8)$$

Table 2: Symbols List

Symbol	Definition
$\mathbf{v}, v$	fluid velocity vector and magnitude
$\mathbf{v}_p$	velocity vector contained in meridional plane, meridional flow
$\mathbf{v}'$	turbulent velocity vector
$v_x, v_y, v_z$	component of fluid velocity in Cartesian coordinate
$\mathbf{B}, B$	magnetic field vector and magnitude
$\mathbf{B}'$	turbulent magnetic field vector
$\mathbf{B}_p$	poloidal magnetic field vector
$B_r, B_\theta, B_\phi$	radial, latitudinal and longitudinal component of magnetic field
$B_x, B_y, B_z$	component of magnetic field in Cartesian coordinate
$\mathbf{A}, A$	vector potential vector and magnitude
$A_r, A_\theta, A_\phi$	radial, latitudinal and longitudinal component of vector potential
$A_x, A_y, A_z$	component of vector potential in Cartesian coordinate
$t$	time coordinate
$\omega$	frequency
$\eta$	magnetic diffusivity by molecular diffusion
$\eta_t$	magnetic diffusivity by turbulent diffusion
$\nu$	molecular viscosity
$\rho$	density
$p$	gas pressure
$T$	temperature
$H_p$	pressure scale height
$\mathbf{\Pi}$	viscous stress tensor
$\tilde{\Omega}$	rotation rate of system
$\mathbf{\Omega}, \Omega$	angular velocity vector and magnitude
$\mathbf{g}, g$	gravitational acceleration vector and magnitude
$x, y, z$	coordinates in Cartesian coordinate
$k, k_x, k_y, k_z$	amplitude and component of the wave number in Cartesian coordinate
$r$	radial coordinate
$\theta$	latitudinal coordinate
$\phi$	longitudinal coordinate
$L$	characteristic length scale
$U$	characteristic speed
$Re$	Reynolds number
$Rm$	magnetic Reynolds number
$N_D$	dynamo number

$$\frac{\partial \mathbf{e}_r}{\partial \theta} = \mathbf{e}_\theta \quad (6.2.9)$$

$$\frac{\partial \mathbf{e}_r}{\partial \phi} = \sin \theta \mathbf{e}_\phi \quad (6.2.10)$$

$$\frac{\partial \mathbf{e}_\theta}{\partial \theta} = -\mathbf{e}_r \quad (6.2.11)$$

$$\frac{\partial \mathbf{e}_\theta}{\partial \phi} = \cos \theta \mathbf{e}_\phi \quad (6.2.12)$$

$$\frac{\partial \mathbf{e}_\phi}{\partial \phi} = -\sin \theta \mathbf{e}_r - \cos \theta \mathbf{e}_\theta \quad (6.2.13)$$

## C Derivation for Axisymmetric Induction Equation

In this section, the axisymmetric induction equations explained in §2.3 are derivated. The magnetic induction equation is expressed as,

$$\frac{\partial \mathbf{B}}{\partial t} = \nabla \times (\mathbf{v} \times \mathbf{B} - \eta \nabla \times \mathbf{B}). \quad (6.3.1)$$

The magnetic field and velocity are decomposed to the toroidal and poloidal components in axisymmetric system ( $\partial/\partial\phi$ ) as,

$$\mathbf{B} = \nabla \times (A_\phi \mathbf{e}_\phi) + B_\phi \mathbf{e}_\phi \quad (6.3.2)$$

$$\mathbf{v} = \mathbf{v}_p + r \sin \theta \Omega \mathbf{e}_\phi, \quad (6.3.3)$$

where the meridional flow can be expressed as  $\mathbf{v}_p = v_r \mathbf{e}_r + v_\theta \mathbf{e}_\theta$ . Then the magnetic induction equation is decomposed to the poloidal and the toroidal components.

$$\begin{aligned} \frac{\partial}{\partial t} (B_\phi \mathbf{e}_\phi + \nabla \times (A_\phi \mathbf{e}_\phi)) = & \nabla \times [(\mathbf{v}_p + r \sin \theta \Omega \mathbf{e}_\phi) \times (B_\phi \mathbf{e}_\phi + \nabla \times (A_\phi \mathbf{e}_\phi)) \\ & - \eta \nabla \times (B_\phi \mathbf{e}_\phi + \nabla \times (A_\phi \mathbf{e}_\phi))]. \end{aligned} \quad (6.3.4)$$

The toroidal component of eq. (6.3.4) is expressed as,

$$\frac{\partial}{\partial t} (B_\phi \mathbf{e}_\phi) = \nabla \times (\mathbf{v}_p \times B_\phi \mathbf{e}_\phi + r \sin \theta \Omega \mathbf{e}_\phi \times \mathbf{B}_p) - \nabla \times (\eta \nabla \times B_\phi \mathbf{e}_\phi). \quad (6.3.5)$$

The first term of the left side of eq. (6.3.5) can be transformed as,

$$\begin{aligned} \nabla \times (\mathbf{v}_p \times B_\phi \mathbf{e}_\phi + r \sin \theta \Omega \mathbf{e}_\phi \times \mathbf{B}_p) &= \left( -\frac{1}{r} \frac{\partial}{\partial r} (r v_r B_\phi) - \frac{1}{r} \frac{\partial}{\partial \theta} (v_\theta B_\phi) \right) \mathbf{e}_\phi \\ &+ r \sin \theta \mathbf{B}_p \cdot \nabla \Omega \mathbf{e}_\phi. \end{aligned} \quad (6.3.6)$$

The second term of the left side of eq. (6.3.5) can be transformed as,

$$\begin{aligned} -\nabla \times (\eta \nabla \times B_\phi \mathbf{e}_\phi) &= \nabla \eta \times (\nabla \times (B_\phi \mathbf{e}_\phi)) + \eta \nabla \times (\nabla \times (B_\phi \mathbf{e}_\phi)) \\ &= \left( \frac{1}{r} \frac{\partial \eta}{\partial r} (r B_\phi) + \frac{1}{r^2} \frac{\partial \eta}{\partial \theta} \frac{1}{\sin \theta} \frac{\partial}{\partial \theta} (\sin \theta B_\phi) \right) \mathbf{e}_\phi \\ &+ \eta \left( \Delta - \frac{1}{r^2 \sin^2 \theta} \right) B_\phi \mathbf{e}_\phi, \end{aligned} \quad (6.3.7)$$

where  $\Delta$  is the Laplacian. Therefore the equation of the toroidal magnetic field can be expressed as,

$$\begin{aligned} \frac{\partial B_\phi}{\partial t} &= -\frac{1}{r} \frac{\partial}{\partial r} (r v_r B_\phi) - \frac{1}{r} \frac{\partial}{\partial \theta} (v_\theta B_\phi) + r \sin \theta \mathbf{B}_p \cdot \nabla \Omega \\ &+ \frac{1}{r} \frac{\partial \eta}{\partial r} (r B_\phi) + \frac{1}{r^2} \frac{\partial \eta}{\partial \theta} \frac{1}{\sin \theta} \frac{\partial}{\partial \theta} (\sin \theta B_\phi) + \eta \left( \Delta - \frac{1}{r^2 \sin^2 \theta} \right) B_\phi. \end{aligned} \quad (6.3.8)$$

The poloidal component of eq. (6.3.4) can be expressed as,

$$\frac{\partial}{\partial t} (A_\phi \mathbf{e}_\phi) = \mathbf{v}_p \times (\nabla \times (A_\phi \mathbf{e}_\phi)) - \eta \nabla \times (\nabla \times (A_\phi \mathbf{e}_\phi)). \quad (6.3.9)$$

Similar to the equation for the toroidal magnetic field, the equation for poloidal magnetic field is expressed as,

$$\frac{\partial A_\phi}{\partial t} = -\frac{v_r}{r} \frac{\partial}{\partial t} (r A_\phi) - \frac{v_\theta}{r \sin \theta} \frac{\partial}{\partial \theta} (\sin \theta A_\phi) + \eta \left[ \Delta - \frac{1}{r^2 \sin^2 \theta} \right] A_\phi. \quad (6.3.10)$$

## D Derivation for Turbulent $\alpha$ effect and Diffusivity

The derivation for the turbulent  $\alpha$  effect and diffusivity is showed in this section (see also Krause & Rädler, 1980). Most of symbols in this section do not obey the

definition in Table 2. We decompose the magnetic field  $\mathbf{B}$  and the velocity field  $\mathbf{v}$  to the mean-field component  $\overline{\mathbf{B}}$ ,  $\overline{\mathbf{v}}$  and turbulent component  $\mathbf{B}'$ ,  $\mathbf{v}'$  as,

$$\mathbf{B} = \overline{\mathbf{B}} + \mathbf{B}' \quad (6.4.1)$$

$$\mathbf{v} = \overline{\mathbf{v}} + \mathbf{v}', \quad (6.4.2)$$

where the overline denotes the ensemble average. On averaging eq. (1.2.1) we obtain

$$\frac{\partial \overline{\mathbf{B}}}{\partial t} = \nabla \times (\overline{\mathbf{v}} \times \overline{\mathbf{B}}) + \nabla \times (\overline{\mathbf{v}' \times \mathbf{B}'}) - \nabla \times (\eta \nabla \times \overline{\mathbf{B}}), \quad (6.4.3)$$

We assume that there is no mean flow, i.e.  $\overline{\mathbf{v}} = 0$ . If we subtract eq. (6.4.3) from eq. (6.4.2) we find

$$\frac{\partial \mathbf{B}'}{\partial t} = \nabla \times (\mathbf{v}' \times \overline{\mathbf{B}} + \mathbf{v}' \times \mathbf{B}' - \overline{\mathbf{v}' \times \mathbf{B}'}) - \nabla \times (\eta \nabla \times \mathbf{B}') \quad (6.4.4)$$

We simplified that the second order fluctuation is small, so the term  $\mathbf{v}' \times \mathbf{B}' - \overline{\mathbf{v}' \times \mathbf{B}'}$  is small. Furthermore the value of the magnetic Reynolds number  $Rm$  is significantly larger than unity (see Appendix E in detail). This means that the term  $-\nabla \times (\eta \nabla \times \mathbf{B}')$  is small. Eq. (6.4.4) can be simplified as,

$$\frac{\partial \mathbf{B}'}{\partial t} \sim \nabla \times (\mathbf{v}' \times \overline{\mathbf{B}}). \quad (6.4.5)$$

In addition the life time of turbulent field  $\tau$  is introduced and eq. (6.4.5) is transformed as,

$$\mathbf{B}' \sim \tau \nabla \times (\mathbf{v}' \times \overline{\mathbf{B}}), \quad (6.4.6)$$

We must evaluate the term  $\overline{\mathbf{v}' \times \mathbf{B}'} = \overline{\mathbf{v}' \times \tau \nabla \times (\mathbf{v}' \times \overline{\mathbf{B}})}$  in eq. (6.4.4). For convenience, two variables are defined as,

$$\omega_{ijk} = \overline{v'_i \frac{\partial v'_k}{\partial x_j}}, \quad (6.4.7)$$

$$u_{ij} = \overline{v'_i v'_j}, \quad (6.4.8)$$

where  $v'_i$  denote the  $i$ th component of turbulent velocity in Cartesian coordinate  $(x_1, x_2, x_3)$ .  $i, j, k$  can take the values 1, 2, 3. We assume the homogeneous isotropy of the turbulence. It is easy to establish the relation of  $\omega_{ijk}, u_{ij}$  under this assumption. These values have to be unchanged with an arbitrary rotation. When, for example,

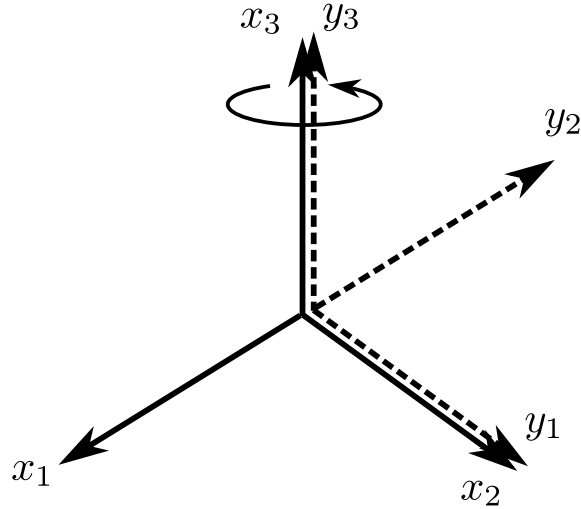


Figure 47: The solid line denotes the original Cartesian coordinate  $(x_1, x_2, x_3)$ . The dashed line denotes the  $90^\circ$ -rotated Cartesian coordinate  $(y_1, y_2, y_3)$

a  $90^\circ$ -rotation about the  $x_3$ -axis is carried out (see Fig. 47), the transformations are expressed as,

$$x_1 \rightarrow y_2, v'_1 \rightarrow v'_2 \quad (6.4.9)$$

$$x_2 \rightarrow -y_1, v'_2 \rightarrow -v'_1 \quad (6.4.10)$$

$$x_3 \rightarrow y_3, v'_3 \rightarrow v'_3 \quad (6.4.11)$$

Then we can obtain the relations of the value  $\omega_{ijk}$ ,  $u_{ij}$  as,

$$u_{23} = -u_{13} = -u_{23} = 0 \quad (6.4.12)$$

$$u_{11} = u_{22} = u_{33} = u \quad (6.4.13)$$

$$\omega_{111} = \omega_{222} = -\omega_{111} = 0 \quad (6.4.14)$$

$$\omega_{331} = \omega_{332} = -\omega_{331} = 0 \quad (6.4.15)$$

$$\omega_{313} = \omega_{323} = -\omega_{313} = 0 \quad (6.4.16)$$

$$\omega_{133} = \omega_{233} = -\omega_{133} = 0 \quad (6.4.17)$$

With 90°-rotation about the other axes  $x_1$  and  $x_2$ , we can figure out two relations.

One can be expressed as,

$$u_{ij} = u\delta_{ij} \quad (6.4.18)$$

Next can be expressed that when at least two of  $i, j, k$  are the same,

$$\omega_{ijk} = 0. \quad (6.4.19)$$

We can evaluate the term  $\mathbf{G} = \mathbf{v}' \times \nabla \times (\mathbf{v}' \times \bar{\mathbf{B}})$  with above relations. We decompose the vector  $\mathbf{G}$  to each component  $G_1$ ,  $G_2$  and  $G_3$ .

$$G_1 = v'_2[\partial_1(v'_3\bar{B}_1) - \partial_2(v'_1\bar{B}_3)] - v'_3[\partial_3(v'_2\bar{B}_3) - \partial_1(v'_3\bar{B}_2)] \quad (6.4.20)$$

$$G_2 = v'_3[\partial_2(v'_1\bar{B}_2) - \partial_3(v'_2\bar{B}_1)] + v'_1[\partial_1(v'_3\bar{B}_1) - \partial_2(v'_1\bar{B}_3)] \quad (6.4.21)$$

$$G_3 = v'_1[\partial_3(v'_2\bar{B}_3) - \partial_1(v'_3\bar{B}_2)] + v'_2[\partial_2(v'_1\bar{B}_2) - \partial_3(v'_2\bar{B}_1)] \quad (6.4.22)$$

$\overline{B}_i$  denotes the  $i$ th component of mean magnetic field.  $\partial_i$  denotes the  $i$ th component derivative ( $\partial/\partial x_i$ ). Averaged Eqs. (6.4.20)-(6.4.22) can be expressed as,

$$\begin{aligned}\overline{\mathbf{G}} &= \begin{pmatrix} \omega_{213}\overline{B}_1 + u_{33}\partial_3\overline{B}_2 - (\omega_{312}\overline{B}_1 + u_{22}\partial_2\overline{B}_3) \\ \omega_{321}\overline{B}_2 + u_{11}\partial_1\overline{B}_3 - (\omega_{123}\overline{B}_2 + u_{33}\partial_3\overline{B}_1) \\ \omega_{132}\overline{B}_3 + u_{22}\partial_2\overline{B}_1 - (\omega_{231}\overline{B}_3 + u_{11}\partial_1\overline{B}_2) \end{pmatrix} \\ &= - \begin{pmatrix} \omega_{312} - \omega_{213} \\ \omega_{123} - \omega_{321} \\ \omega_{231} - \omega_{132} \end{pmatrix} \cdot \overline{\mathbf{B}} - \frac{1}{3}\overline{\mathbf{v}'^2}(\nabla \times \overline{\mathbf{B}}).\end{aligned}\quad (6.4.23)$$

Then, there are relations as,

$$\omega_{312} - \omega_{213} = \omega_{123} - \omega_{321} = \omega_{231} - \omega_{132} = \frac{1}{3}\overline{\mathbf{v}' \cdot \nabla \times \mathbf{v}'}. \quad (6.4.24)$$

These equations can be verified with  $90^\circ$  about each axis. At last we can evaluate the term  $\overline{\mathbf{v}' \times \mathbf{B}'}$  as,

$$\overline{\mathbf{v}' \times \mathbf{B}'} = \alpha \overline{\mathbf{B}} - \eta_t \nabla \times \overline{\mathbf{B}} \quad (6.4.25)$$

$$\alpha = -\frac{\tau}{3}\overline{\mathbf{v}' \cdot \nabla \times \mathbf{v}'}. \quad (6.4.26)$$

$$\eta_t = \frac{\tau}{3}\overline{\mathbf{v}'^2} \quad (6.4.27)$$

This  $\eta_t$  is a basis for the value for the turbulent diffusivity used in Part III and IV.

## E Non-dimensional Number in Solar Convection Zone

Some non-dimensional numbers are evaluated in this section (see also Miesch, 2005). At first the Reynolds number  $Re$  is evaluated. The Reynolds number  $Re$  shows the ratio of time scale for viscous diffusion to advection. The molecular viscosity  $\nu$  of fully-ionized hydrogen in the solar interior is estimated by  $\nu \sim 1.2 \times 10^{-16} T^{5/2} / \rho \text{ cm}^2 \text{ s}^{-1}$  (Chapman, 1954; Parker, 1979). The value of the temperature

and the density are  $T \sim 2.2 \times 10^6$  K and  $\rho \sim 0.2$  g cm<sup>-3</sup> at the base of convection zone (Stix, 2004). This yields  $\nu \sim 3$  cm<sup>2</sup> s<sup>-1</sup>. The speed of the convection velocity is thought to be  $10^4$  cm s<sup>-1</sup> at the base of convection zone. The length scale can be taken the same as pressure scale height, so  $L \sim 7 \times 10^9$  cm. Therefore the Reynolds number at the base of convection zone can be estimated as,

$$Re = \frac{UL}{\nu} \sim 10^{12}. \quad (6.5.1)$$

Next, the magnetic Reynolds number  $Rm$  is estimated. The magnetic Reynolds number shows the ratio of time scale for advection and magnetic diffusion. The molecular magnetic diffusivity  $\eta$  is estimated by  $\eta = 10^{13}T^{-3/2}$  cm<sup>2</sup> s<sup>-1</sup> (Cowling, 1953; Spitzer, 1956). The same parameter as those for the Reynolds number are used. The molecular magnetic diffusivity  $\eta = 10^4$  cm<sup>2</sup> s<sup>-1</sup> at the base of convection zone. Therefore the magnetic Reynolds number at the base of convection zone is estimated as,

$$Rm = \frac{UL}{\eta} \sim 10^9. \quad (6.5.2)$$

## F Physical Meaning of $\Lambda$ effect

In this section the physical meaning of the  $\Lambda$  effect mentioned in Part V is explained. The  $\Lambda$  effect is a non-diffusive angular momentum transport caused by the coupling of the anisotropy of convection and the Coriolis force (Kichatinov & Rudiger, 1993). At first we explain the physical processes where each component of the convection transports angular momentum in the northern hemisphere of a rigidly rotating star. In a rotational system, the negative (positive) radial velocity ( $v'_r$ ) is bent by the Coriolis force, so that the positive (negative) longitudinal velocity

$\langle v'_\phi \rangle$  is generated (Fig. 48a). It means that the correlation between the radial and longitudinal velocity, i.e.,  $\langle v'_r v'_\phi \rangle$  is negative, so the angular momentum is transported inwardly by the Reynolds stress which is proportional to  $\langle v'_r v'_\phi \rangle$ . The same logic can be adopted for the latitudinal and longitudinal components of convection. It is easily understood that the latitudinal velocity transports angular momentum poleward (Fig. 48b) and the longitudinal velocity transports outwardly from the rotational axis (Fig. 48c).

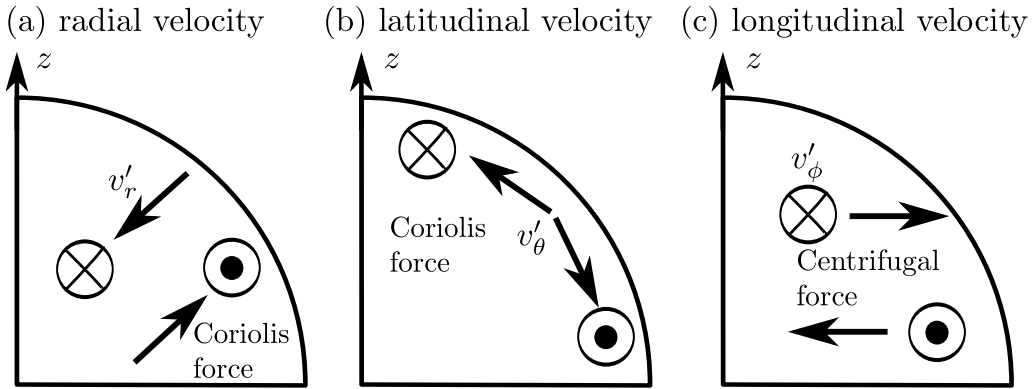


Figure 48: The schematic picture of the  $\Lambda$  effect. The  $z$ -axis is the rotational axis.

When the turbulence is isotropic, the angular momentum transports by the each component of the Reynolds stress are balanced and there is no non-diffusive transport. Anisotropy of turbulence is the essential factor of the  $\Lambda$  effect. There is anisotropy in a turbulence of a convection where radial velocity is higher than the others due to the stratification. This higher radial velocity generates the inward non-diffusive angular momentum transport. Furthermore, in the rapidly rotating stars, the effect of the rotation also generates the anisotropy of the turbulence, so the situation becomes complicated. If the longitudinal component of the convection is dominated, the  $\Lambda$  effect can transport angular momentum equatorward like our

sun.

## G Numerical Method

In this section, I explain the numerical schemes I use.

### G.1 modified Lax-Wendroff scheme

I explain the modified Lax-Wendroff scheme which is used in Part III, IV and V (Rubin & Burstein, 1967). The modified Lax-Wendroff scheme is the second-order scheme for time and space. This scheme can solve the equation which is the quasi-conservational form,

$$\frac{\partial Q}{\partial t} + \frac{\partial F(Q)}{\partial x} + \frac{\partial G(Q)}{\partial y} + S(Q) = 0, \quad (6.7.1)$$

In the modified Lax-Wendroff scheme, the time integrations at each time step are carried out in two-step calculations. In the following, the discretized variables for  $Q$ ,  $F_x$ ,  $F_y$  and  $S$  are defined as,

$$W_{i,j}^n = W(t_n, x_i, y_j), \quad (6.7.2)$$

$$F_{i,j}^n = F(W_{i,j}^n) = 0, \quad (6.7.3)$$

$$G_{i,j}^n = G(W_{i,j}^n) = 0, \quad (6.7.4)$$

$$S_{i,j}^n = S(W_{i,j}^n) = 0, \quad (6.7.5)$$

where  $t_n$  is the discretized time variable with  $n(= 0, 1, 2, \dots)$  and the discrete time stepmesh points are given by  $(x_i, y_j)$  with  $i, j(= 0, 1, 2, \dots)$ . In the first step of this

scheme, we calculate the physical values at mid-mesh point  $(x_{i+\frac{1}{2}}, y_{j+\frac{1}{2}})$  as,

$$\begin{aligned}
Q_{i+\frac{1}{2},j+\frac{1}{2}}^{n+1} &= \frac{1}{4} (Q_{i+1,j+1}^n + Q_{i+1,j}^n + Q_{i,j+1}^n + Q_{i,j}^n) \\
&- \frac{\Delta t}{2\Delta x_{i+\frac{1}{2}}} (F_{i+1,j+1}^n - F_{i+1,j}^n + F_{i+1,j}^n - F_{i,j}^n) \\
&- \frac{\Delta t}{2\Delta y_{j+\frac{1}{2}}} (G_{i+1,j+1}^n - G_{i,j+1}^n + G_{i,j+1}^n - G_{i,j}^n) \\
&- \frac{\Delta t}{4} (S_{i+1,j+1}^n + S_{i+1,j}^n + S_{i,j+1}^n + S_{i,j}^n), \tag{6.7.6}
\end{aligned}$$

where  $\Delta x_{i+\frac{1}{2}} \equiv x_{i+1} - x_i$  and  $\Delta y_{j+\frac{1}{2}} \equiv y_{j+1} - y_j$  are the mesh spacing in each direction and  $\Delta t \equiv t_{n+1} - t_n$  is the time spacing. The numerical fluxes and sources at the mid-mesh points are calculated as,

$$F_{i+\frac{1}{2},j+\frac{1}{2}}^{n+1} = F(Q_{i+\frac{1}{2},j+\frac{1}{2}}^{n+1}) \tag{6.7.7}$$

$$G_{i+\frac{1}{2},j+\frac{1}{2}}^{n+1} = G(Q_{i+\frac{1}{2},j+\frac{1}{2}}^{n+1}) \tag{6.7.8}$$

$$S_{i+\frac{1}{2},j+\frac{1}{2}}^{n+1} = S(Q_{i+\frac{1}{2},j+\frac{1}{2}}^{n+1}). \tag{6.7.9}$$

$$\tag{6.7.10}$$

The numerical fluxes and source at the interfaces of each mesh points are derived as,

$$\tilde{F}_{i+\frac{1}{2},j}^{n+1} = \frac{\Delta y_{j-\frac{1}{2}}}{2\Delta y_j} F_{i+\frac{1}{2},j+\frac{1}{2}}^{n+1} + \frac{\Delta y_{j+\frac{1}{2}}}{2\Delta y_j} F_{i+\frac{1}{2},j-\frac{1}{2}}^{n+1} \tag{6.7.11}$$

$$\tilde{G}_{i,j+\frac{1}{2}}^{n+1} = \frac{\Delta x_{i-\frac{1}{2}}}{2\Delta x_i} F_{i+\frac{1}{2},j+\frac{1}{2}}^{n+1} + \frac{\Delta x_{i+\frac{1}{2}}}{2\Delta x_i} F_{i-\frac{1}{2},j+\frac{1}{2}}^{n+1} \tag{6.7.12}$$

$$\begin{aligned}
\tilde{S}_{i,j}^{n+1} &= \frac{\Delta y_{j-\frac{1}{2}}}{2\Delta y_j} \left( \frac{\Delta x_{i-\frac{1}{2}}}{2\Delta x_i} S_{i+\frac{1}{2},j+\frac{1}{2}}^{n+1} + \frac{\Delta x_{i+\frac{1}{2}}}{2\Delta x_i} S_{i-\frac{1}{2},j+\frac{1}{2}}^{n+1} \right) \\
&+ \frac{\Delta y_{j+\frac{1}{2}}}{2\Delta y_j} \left( \frac{\Delta x_{i-\frac{1}{2}}}{2\Delta x_i} S_{i+\frac{1}{2},j-\frac{1}{2}}^{n+1} + \frac{\Delta x_{i+\frac{1}{2}}}{2\Delta x_i} S_{i-\frac{1}{2},j-\frac{1}{2}}^{n+1} \right), \tag{6.7.13}
\end{aligned}$$

where

$$\Delta x_i = \frac{1}{2} \left( \Delta x_{i+\frac{1}{2}} + \Delta x_{i-\frac{1}{2}} \right) \quad (6.7.14)$$

$$\Delta y_i = \frac{1}{2} \left( \Delta y_{j+\frac{1}{2}} + \Delta y_{j-\frac{1}{2}} \right) \quad (6.7.15)$$

The second step of the modified Lax-Wendroff is expressed as,

$$W_{i,j}^{n+1} = W_{i,j}^n \quad (6.7.16)$$

$$- \frac{\Delta t}{4\Delta x_i} \left( F_{i+1,j}^n - F_{i-1,j}^n + 2F_{i+\frac{1}{2},j}^n - 2F_{i-\frac{1}{2},j}^n \right) \quad (6.7.17)$$

$$- \frac{\Delta t}{4\Delta y_j} \left( G_{i,j+1}^n - G_{i,j-1}^n + 2G_{i,j+\frac{1}{2}}^n - 2G_{i,j-\frac{1}{2}}^n \right) \quad (6.7.18)$$

$$- \frac{\Delta t}{2} \left( S_{i,j}^n + \tilde{S}_{i,j}^{n+1} \right) \quad (6.7.19)$$

## G.2 artificial viscosity which satisfied TVD criterion

In this section, the TVD (Total Variation Diminishing) artificial viscosity suggested by Davis (1984) is explained. Using this artificial viscosity, a scheme can be TVD scheme. The most important advantage of a TVD scheme is that this scheme does not produce numerical oscillation, since a TVD scheme is monotonicity preserving (Harten, 1983). The viscous term is added after the second step of the modified Lax-Wendroff scheme as,

$$Q_{i,j}^{n+1(\text{new})} = Q_{i,j}^{n+1(\text{old})} + D_{i,j}^n, \quad (6.7.20)$$

where  $D_{i,j}^{n+1}$  is the viscous term.  $Q_{i,j}^{n+1(\text{old})}$  is the physical value for the new time step  $t_{n+1}$  obtained by the modified Lax-Wendroff scheme, and  $Q_{i,j}^{n+1(\text{new})}$  is the final result for this time step. At first a difference of the physical value is defined as,

$$\Delta Q_{i+\frac{1}{2},j}^n = Q_{i+1,j}^n - Q_{i,j}^n \quad (6.7.21)$$

$$\Delta Q_{i,j+\frac{1}{2}}^n = Q_{i,j+1}^n - Q_{i,j}^n. \quad (6.7.22)$$

Then, we define values as,

$$r_{x,i,j}^+ = \frac{\Delta Q_{i-\frac{1}{2},j}^n}{\Delta Q_{i+\frac{1}{2},j}^n}, \quad (6.7.23)$$

$$r_{x,i,j}^- = \frac{\Delta Q_{i+\frac{1}{2},j}^n}{\Delta Q_{i-\frac{1}{2},j}^n}, \quad (6.7.24)$$

$$r_{y,i,j}^+ = \frac{\Delta Q_{i,j-\frac{1}{2}}^n}{\Delta Q_{i,j+\frac{1}{2}}^n}, \quad (6.7.25)$$

$$r_{y,i,j}^- = \frac{\Delta Q_{i,j+\frac{1}{2}}^n}{\Delta Q_{i,j-\frac{1}{2}}^n}. \quad (6.7.26)$$

The coefficient for the artificial viscosity is defined as,

$$K_x(r_{x,i,j}) = \frac{1}{2}c(\nu_{x,i}) [1 - \phi(r_{x,i,j})], \quad (6.7.27)$$

$$K_y(r_{y,i,j}) = \frac{1}{2}c(\nu_{y,j}) [1 - \phi(r_{y,i,j})], \quad (6.7.28)$$

where  $c(\nu) = \nu(1 - \nu)$  with the Courant number,  $\nu_{x,i}^\pm = \Delta t / \Delta x_{i \pm \frac{1}{2}}$  and  $\nu_{y,j}^\pm = \Delta t / \Delta y_{j \pm \frac{1}{2}}$ . The function  $\phi$  is defined as,

$$\phi(r) = \text{minmod}(r, 1), \quad (6.7.29)$$

where  $\text{minmod}(a, b)$  is  $\min(a, b)$  (zero) with the same (different) signs of  $a$  and  $b$ .

Using these definitions, the viscous term  $D_{i,j}^n$  is expressed as,

$$\begin{aligned} D_{i,j}^n &= [K_x(r_{x,i,j}^+) + K_x(r_{x,i+1,j}^-)] (Q_{i+1,j}^n - Q_{i,j}^n) \\ &\quad - [K_x(r_{x,i-1,j}^+) + K_x(r_{x,i,j}^-)] (Q_{i,j}^n - Q_{i-1,j}^n) \\ &\quad + [K_y(r_{y,i,j}^+) + K_y(r_{y,i,j+1}^-)] (Q_{i,j+1}^n - Q_{i,j}^n) \\ &\quad - [K_y(r_{y,i,j-1}^+) + K_y(r_{y,i,j}^-)] (Q_{i,j}^n - Q_{i,j-1}^n). \end{aligned} \quad (6.7.30)$$